University of Alberta

Polymer Monoliths Photopatterned within Microfluidic Devices for Proteomics and Separation Science

by

Mei He

A thesis submitted to the Faculty of Graduate Studies and Research in partial fulfillment of the requirements for the degree of Doctor of Philosophy

Department of Chemistry

Edmonton, Alberta
Fall 2008

Library and Archives Canada

Published Heritage Branch

395 Wellington Street
Ottawa ON K1A 0N4
Canada

Bibliothèque et Archives Canada

Direction du Patrimoine de l'édition

395, rue Wellington
Ottawa ON K1A 0N4
Canada

Your file Votre référence
ISBN: 978-0-494-46330-7
Our file Notre référence
ISBN: 978-0-494-46330-7

NOTICE:
The author has granted a non-exclusive license allowing Library and Archives Canada to reproduce, publish, archive, preserve, conserve, communicate to the public by telecommunication or on the Internet, loan, distribute and sell theses worldwide, for commercial or non-commercial purposes, in microform, paper, electronic and/or any other formats.

The author retains copyright ownership and moral rights in this thesis. Neither the thesis nor substantial extracts from it may be printed or otherwise reproduced without the author's permission.

AVIS:
L'auteur a accordé une licence non exclusive permettant à la Bibliothèque et Archives Canada de reproduire, publier, archiver, sauvegarder, conserver, transmettre au public par télécommunication ou par l'Internet, prêter, distribuer et vendre des thèses partout dans le monde, à des fins commerciales ou autres, sur support microforme, papier, électronique et/ou autres formats.

L'auteur conserve la propriété du droit d'auteur et des droits moraux qui protège cette thèse. Ni la thèse ni des extraits substantiels de celle-ci ne doivent être imprimés ou autrement reproduits sans son autorisation.

In compliance with the Canadian Privacy Act some supporting forms may have been removed from this thesis.

While these forms may be included in the document page count, their removal does not represent any loss of content from the thesis.

Conformément à la loi canadienne sur la protection de la vie privée, quelques formulaires secondaires ont été enlevés de cette thèse.

Bien que ces formulaires aient inclus dans la pagination, il n'y aura aucun contenu manquant.

Canada

Abstract

This thesis reports the fundamental and systematic investigation of photopatterning of monolithic structures within microfluidic chips, as well as the exploration of their applications for separation science and proteomics. First, the effects of polymerization conditions on the porosity of photopatterned monolithic beds were evaluated by the measurement of their fluidic properties using a time of flight, photobleaching method. Out of a wide range of polymerization conditions in terms of monomer composition and porogenic solvent, a narrow composition window was obtained which gives good reproducibility and stability for HEMA based monolithic beds, and it was applied to immobilize trypsin for on-bed digestion. Second, it was observed that the physical confinement of microchannels induces significant spatial variation of monolithic structures, which leads to a new strategy to manipulate the morphology of polymer monoliths within micrometer-scale space. The extent of deformation from the bulk porous structure under confinement strongly depends on the ratio of the characteristic length of the confined space to the monolith pore size. At the extreme limit of deformation a smooth polymer layer is formed on the surface of capillary or microchannel. This confinement-induced structural deformation provides a rapid and effective strategy for robust wall coating. Finally, using this new coating strategy, we have realized several types of coating films within microchannels with tunable thicknesses ranging from ~100 nm to ~700 nm. Neutral and hydrophilic HEMA-based coatings have been demonstrated for reducing non-specific adsorption during protein separation. We also demonstrated photografting the monolithic coating with positively

charged META for EOF control, and with zwitterionic SBMA for open channel CEC separation of proteins. Our results demonstrate that this method provides a facile and robust surface modification strategy for applications such as surface chemistry control, surface biocompatibility, capillary electrophoresis and open tubular chromatography.

Acknowledgements

I would here like to express my thanks to the people who have been very helpful to me during the time it took me to write this thesis.

I have been very fortunate under the supervision of Dr. Jed D. Harrison, who provides support, encouragement, refreshing insight and guidance, and also critical questions. He always brought a thorough eye into the research projects. Such experience under his guidance is the most valuable asset to my future career growth. I would like to express my great thanks to him. I also thank him for financing my attendance at many academic conferences, which offered me excellent opportunities to expand my knowledge and research thoughts.

I would like to sincerely thank the strong support from my supervisory committee members, Professors Liang Li, Uttandaraman Sundararaj, Charles Lucy, David Bundle and Derrick L. J. Clive. I also thank Prof. Vincent Remcho for his willingness to serve as my external examiner. Especially, I feel grateful to Profs Liang Li and Uttandaraman Sundararaj for their valuable support of my postdoctoral application. Great thanks to Dr. Xuejun Sun in the Oncology Department for his valuable discussion on confocal microscope analysis. Without his help, I could not obtain the results and findings presented in Chapter 3 of my dissertation. Special thanks to Dr. Robert Campbell, who provided useful suggestions about microscopy for my research work in Chapter 4. Meanwhile, I would like to say thanks to the staff from the electronic, machine and glass shops, mass spectrometry lab, chemical storeroom, and NanoFab. Without their support, my research work would not have been completed.

I greatly thank all the members of the Harrison group, including Arlene Figley, Dr. Svetlana Sapelnikova, Jing Wen, Dr. Guifeng Jiang, Kowlasar Misir, Dr. Zhen Wang, Dr. Yong Zeng, Dr. Dolores Martinez, Dr. James Bao and Dr. Eric Flaim for their helpful assistance, and finally, my labmates, Josh Wasylycia, Qingye Lu, Yujuan Hua and Neda Nazemifard for their helpful discussion and friendship. You all have made my study and life in Edmonton enjoyable.

Foremost, I would like to express my wordless gratitude to my family, my father, my mother, my husband, my sister and brother. Without their understanding and support, I would not take the way to pursue my doctoral research. Great and special thanks to my mom. Thank you for accompanying me during my last year in Edmonton and thank you, mom, for all the things you did.

List of Contents

Chapter 1 Introduction

1.1 Background and Motivation 1

1.1.1 Lab-on-chip Devices for Bioanalysis 1

1.1.2 Functional Chemical Materials for Lab-on-chip Integration 7

1.1.3 Motivation and Scope of the Thesis 13

1.2 Photopolymerized Polymer Monolith 17

1.2.1 Photo-initiated Free Radical Polymerization 20

1.2.2 Photografting 22

1.3 Capillary Electrophoresis and Capillary Electrochromatography 23

1.3.1 Capillary Electrophoresis 23

1.3.2 Capillary Electrochromatography 26

1.3.3 Separation Efficiency and Resolution 27

1.3.4 Microchip Electrophoresis and Electrochromatography 28

1.4 References 31

Chapter 2 Characterization of Flow Properties of Porous Monoliths Photopatterned within Microfluidic Channels

2.1 Introduction 38

2.2 Materials and Methods 40

2.2.1 Reagents and Samples 40

2.2.2 Preparation of the Photo-polymerized Monoliths within Microchannels 40

2.2.3 Recovery of Glass Chip 41

2.2.4 Characterization of Monoliths in Microchannels 41

2.3 Results and Discussion 42

2.3.1 Photobleaching, Time of Flight Linear Flow Rate Measurement Method 42
2.3.2 Porogenic Solvents Selection for Monoliths Localized in Microchannels 46
2.3.3 The Effect of Exposure Time on Structure 50
2.3.4 Fluidic Stability and Reproducibility of Monoliths Photopatterned within Microchannels 52
2.4 Conclusions 61
2.5 References 61

Chapter 3 Confinement Effects on the Morphology of Photopatterned Porous Polymer Monoliths for Capillary and Microchip Wall Coatings

3.1 Introduction 64
3.2 Materials and Methods 66
3.2.1 Microfluidic Device Fabrication 66
3.2.2 Preparation of Photo-polymerized Monoliths 67
3.2.3 Characterization of Monoliths 69
3.3 Results and Discussion. 70
3.3.1 Monolith Structure as a Funcation of Confinement 70
3.3.2 Parameters Affecting Deformation of Monolith Materials 77
3.3.3 Thermal-initiated Polymerization Under Confinement 84
3.3.4 Functionalization of Thick Wall Coatings Formed by Confinement Effect 88
3.4 Conclusions 90
3.5 References 90

Chapter 4 Photopatternable Multifunctional Coatings Based on Confinement Effect for Fast Microchip Electrophoresis of Proteins and Peptides

4.1 Introduction 93

4.2 Materials and Methods 95

4.2.1 Microfluidic Device Fabrication 95

4.2.2 Samples and Reagents 96

4.2.3 Preparation of Photo-polymerized Coatings 96

4.2.4 Microchip Electrophoresis Conditions 97

4.3 Results and Discussion 98

4.3.1 Photopattern Properties of Coatings in Confined Channels 98

4.3.2 Tunable Thickness of the Photopolymerized Coating 101

4.3.3 EOF Monitoring for Evaluating the Surface Modification 105

4.3.3.1 The Dependence of EOF on Buffer pH Value 107

4.3.3.2 Long-term Stability of EOF 107

4.3.4 Injection Geometry Optimization for Separation 110

4.3.5 Protein Separation Performance 115

4.3.6 Separation of Enzymatic Digest Mixtures 123

4.4 Conclusions 127

4.5 References 127

Chapter 5 Polymer Monolith Photopatterned within Microfluidic Devices as Enzymatic Microreactor

5.1 Introduction 130

5.2 Materials and Methods 132

5.2.1 Reagents and Samples 132

5.2.2 Trypsin Immobilization Procedure 132

5.2.3 Mass Spectrometry Conditions 133

5.3 Results and Discussion. 134
5.3.1 Photoinitiator 134
5.3.2 Photopatterning Resolution 136
5.3.3 Sovent Selection 139
5.3.4 Pore Structure 139
5.3.5 Enzymatic Microreactor 142
5.4 Conclusions 147
5.5 References 147

Chapter 6 Conclusions and Future Work

6.1 Summary of the Thesis 149
6.2 Future Work 151
6.3 References 153

APPENDIX Summary of Pore Size of Monoliths Corresponding to Different Recipes Reported in the Literature

..... 154

List of Tables

Table 2.1 Pore sizes of bulk poly (HEMA-co-EDMA) measured by Hg intrusion porosimetry. 44

Table 2.2 Influence of the amounts of monomer HEMA, crosslinker EDMA and porogenic solvent octanol on the monolith structure. 49

Table 3.1 The recipes and the resultant pore sizes for different photo-polymerized monoliths. 68

Table 4.1 Buffer prepared with varied pH value for EOF measurement. 98

Table 4.2 The film thickness measured from 20 batches of coatings in different space dimensions. ...102

Table 4.3 EOF measurements for one-step coating method by adding META into starting mixture. ...105

Table 4.4 Separation efficiency, migration time, and relative standard deviation for protein separation with 20 consecutive runs and day-to-day runs. The data was calculated from Figure 4.11 and Figure 4.12 within one device. ...121

Table 4.5 Separation efficiency, migration time, half peak width and relative standard deviation for protein separation with 20 consecutive runs. The data was calculated from Figure 4.13 within one device. ...121

Table 5.1 The recipe for the photopolymerization of microreactor. ...133

Table 5.2 Experimentally identified peptides from Figure 5.9. ...145

Table 5.3 The Experimentally identified peptides from Figure 5.10. ...146

List of Figures

Chapter 1

Figure 1.1 Miniaturized microfluidic and nanofluidic devices. **A**: Layout of a PDMS microchip for single-cell analysis, showing the cell-manipulation section on the left and the molecule-counting section on the right [25][1]. Pneumatic valves were integrated to sequentially control single cell injection and capture. **B**: A nanofluidic filtering structure for separating both DNA and protein molecules (left) based on two distinct mechanisms: entropic trapping for long, flexible DNA chains (right top) and Ogston sieving for short, rigid DNA fragments and SDS-denatured proteins (right bottom), adapted from [26]. **C**: A complex microfluidic network used to generate a concentration gradient profile across the channel based on the diffusion in laminar flow [28][2]. 3

Figure 1.2 Microfluidic systems for high-throughput screening of protein crystallization conditions. **A**: A large-scale integrated device containing 480 active valves and 144 parallel reaction chambers [31][3]. The inset shows the real size of the device. **B**: A microdroplet generator coupled with a capillary for on-line X-ray detection [32][4]. Left: the schematic illustration of reagent mixing and droplet formation; right: A photograph of the real composite PDMS device (top) as well as the protein crystals formed in the individual droplets and a representative x-ray data (bottom). 5

Figure 1.3 Micromachined separation matrix structures. **A**: A 10-μm thick monolithic column microfabricated by reactive ion etching on quartz for microchip-based liquid phase chromatography [40][2]. **B**: An array of micropillars made by replication from a PDMS mould, adapted from [41]. 7

Figure 1.4 Integrated SDS-PAGE microchip with sample preconcentrator based on photopatterned cross-linked polyacrylamide gel [45][2]. **A**: Chip layout. The inset shows a bright-field image of a photopolymerized size exclusion membrane (visible due to light scattering) positioned in the offset-T junction. **B–D**: Schematic and fluorescent images of sequential process of protein analysis by switching electric fields applied to the reagent reservoirs, including preconcentration, elution, and separation. 8

Figure 1.5 Packing beads in microfluidic chips. **A**: Schematic and video images showing electrokinetic packing process using dual weir structures [47][2]. **B**: Schematic and photograph of microchannel packing silica gel beads within a microchannel with a dam structure, adapted from [48]. 9

Figure 1.6 Multifunctional integration of photopolymerized monolith within microfluidic chips. **A**: Sequential enzyme immobilization [50][2]. **B**: Monolithic mixer [51][4]. **C**: Monolithic solid phase for microchip-based electro-chromatography separation [52][2]. **D**: Two-stage, dual-phase microdevice with photopatterned monolithic column for DNA extraction [53][2]. **E**: Monolithic beds array for protein preconcentration, adapted from [54]. **F**: Mobile polymer monolith for valve control in microchip HPLC separation [55][2]. 12

Figure 1.7 Microfluidics Platform for multiplexed protein analysis. Top: side-view of one of the 20 microchannels in platform. Bottom: The design of the protein processing platform coupled with ESI-MS. Adapted from Taylor *et al.* [58]. 14

Figure 1.8 SEM image showing the structure of a porous polymer monolith in dry state. 18

Figure 1.9 The monomers and crosslinkers used for polymerization of porous monoliths. **1**: Styrene; **2**: Butyl methacrylate; **3**: [2-(methacryloyloxy) ethyl]- trimethylammonium chloride; **4**: glycidyl methacrylate; **5**: vinyl azlactone; **6**: 2-acrylamido-2-methyl-1-propanesulfonic acid; **7**: Acrylamide; **8**: 2-hydroxyethyl methacrylate; **9**: divinylbenzene; **10**: ethylene dimethacrylate 19

Figure 1.10 Mechanism of free radical polymerization, adapted from [77]. R is the radical formed by the decomposition of photoinitiator. 21

Figure 1.11 Schematic representation of the growing polymer chains during photografting with increasing irradiation time from A to C, adapted from [88]. 23

Figure 1.12 Schematic illustration for the mechanism of the electroosmotic flow within glass channel. 24

Figure 1.13 Schematic illustration of the mechanism of the capillary electrophoresis separation. 26

Figure 1.14 The difference between the profiles of flow driven by pressure and EOF in a packed column. Adapted from ref [101]. 27

Figure 1.15 The schematic setup for microchip electrophoresis coupled with laser induced fluorescence detection (LIF). 29

Chapter 2

Figure 2.1 The flow resistance of monoliths poly (HEMA-co-EDMA) produced by using different total weight percentages of 1-octanol solvent in a 600-μm wide and 20-μm deep glass channel. ♦ 70% 1-octanol; □ 65% 1-octanol; ▲ 55% 1-octanol. See Table 2.1 for the corresponding pore size measured by Hg intrusion porosimetry. 44

Figure 2.2 Pore size distribution measured by mercury intrusion porosimetry. **A**: 1.05 μm pore size measured twice for the same sample. The recipe was the same as indicated in Figure 2.1, 70% 1-octanol. **B**: 1.04 μm pore size measured from two batches of polymer monoliths. The recipe was the same as indicated in Figure 2.1, 55% 1-octanol. 45

Figure 2.3 **A**: Diffuse edge of polymer monolith within microchannel produced by volatile porogenic solvents: 30% methanol and 30% 1-propanol. **B**: Sharp edge of monolith produced using 1-octanol. **C**: The flow resistance of monoliths poly (HEMA-co-EDMA) formed using different porogenic solvents. 1: 60% toluene, 2: 65% 1-octanol, 3: 60% 1-heptanol, 4: 60% 1-hexanol, 5: 15% toluene+45%1-dodecanol, 6: 42%1-dodecanol + 18% cyclohexanol, 7: 30%1-decanol+30%1,4-butanediol. 48

Figure 2.4 The stability of the monolith prepared using the recipe in ref [20]: HEMA 24%, EDMA 16%, 42%1-dodecanol, 18% cyclohexanol. The variation for day-to-day reproducibility is 23.2%. 49

Figure 2.5 The effect of exposure time on the flow resistance (**A**) and porous monolithic structures (**B** 6 min, **C** 11 min). The HEMA based polymer monoliths were prepared from 60 wt% 1-octanol and 40 wt% monomer mixture (EDMA/[HEMA+EDMA]=60 wt%). The solid curve is drawn as a guide to eye. 51

Figure 2.6 Flow properties of different beds formed by using different amounts of porogenic solvent 1-octanol (EDMA/(HEMA+EDMA) fixed at 70 wt% ratio) (**A**) and different ratio of crosslinker EDMA/(HEMA+EDMA) (solvent fixed at 70 wt% 1-octanol)(**B**). 55

Figure 2.7 The flow stability of the monolithic beds over 7 days for different composition ratios. The graphs of A-D represent the stable and reproducible flow resistance for monoliths with the same amount of 70 wt% EDMA/ (HEMA+EDMA) and different amounts of 1-octanol: **A** 70%, **B** 65%, **C** 60%, **D** 55%. 56

Figure 2.8 The flow stability of the monolithic beds over 7 days for different composition ratios. The graphs of A-D represent the unstable flow resistance for monolith with the same amount of 30 wt% EDMA/ (HEMA+EDMA) and different amounts of 1-octanol: **A** 70%, **B** 65%, **C** 60%, **D** 55%. 57

Figure 2.9 The effect of crosslinker and solvent ratio on the flow stability of photopatterned monoliths over 7 days. The RSD was calculated for the slope of the plot of flow rate versus pressure. The pooled RSD shown here is the pooled value measured from two batches of monolithic columns ($n_1+n_2=7$). 58

Figure 2.10 Flow measurements for different batches of monolithic beds with the same polymerization conditions on one microfluidic device. The monoliths were prepared with a component ratio within the stable composition range. 59

Figure 2.11 Flow properties measured on monolithic beds within different wafers with the same polymerization conditions. The recipe is the same as indicated in Figure 2.10. 60

Chapter 3

Figure 3.1 Experimental setup for (left) photoinitiated polymerization and (right) laser scanning confocal microscopy, with a double T separation chip illustrated. 68

Figure 3.2 The morphology of Monolith 1 photopatterned in fused-silica capillary with different internal diameters. Recipe is listed in Table 3.1. 71

Figure 3.3 Evolution of the morphology of photo-polymerized monoliths with decreasing capillary diameter (**A**), and the corresponding pore size of the bulk polymer by Hg intrusion porosimetry (**B**). Numbers refer to the monolith number. No surface treatment was used on the capillaries. See Table 3.1 for composition of each monolith (M1 refers to Monolith 1, etc.). 74

Figure 3.4 The reconstructed LSCM images and depth profiles of volume fractions for hydrophilic Monolith 1 photo-polymerized within microchannels that were not surface treated. LSCM was conducted in negative mode, thus the pore is dark and the solid monolith is bright. 75

Figure 3.5 The reconstructed LSCM images and depth profiles of volume fractions for hydrophobic Monolith 3 photo-polymerized within microchannels that were not surface treated. LSCM was conducted in negative mode, thus the pore is dark and the solid monolith is bright. 76

Figure 3.6 The reconstructed laser scanning confocal micrographs of the morphology of Monolith 1 photo-polymerized in microchannels with the indicated depths, and with different surface chemistries: (a) a hydrophilic surface and (b) a hydrophobic surface. 80

Figure 3.7 The depth profiles of volume fraction for hydrophilic Monolith 1(**A**) and Monolith 2 (**B**), as well as hydrophobic Monolith 3 (**C**) within microchannels with either hydrophilic or hydrophobic surface chemistry. 81

Figure 3.8 The depth profiles of volume fraction for hydrophilic Monolith 1 (**A**) and hydrophobic Monolith 3 (**B**) within microchannels with either hydrophilic or hydrophobic surface chemistry. 82

Figure 3.9 The cross-sectional SEM images of the 5-μm i.d. capillary. Monolith 1 was photo-polymerized under confinement with partial UV light exposure. **A**: non-exposure zone; **B**: exposure zone. 83

Figure 3.10 The morphology of polymer monolith evolved with the reaction time under confinement (20-μm i.d. capillary) by using thermal-initiated polymerization. Reaction time **A**: 10 min; **B**: 16 min; **C**: 22 min; **D**: 30 min; **E**: 180 min; **F**: 240 min. Polymerization conditions: HEMA 12 wt%, EDMA 8 wt%, toluene 80 wt%, AIBN 0.2 wt%, T= 85 ℃. This recipe only forms the film layer in 20-μm i.d. capillary by using photo-initiated polymerization. 86

Figure 3.11 The morphology of polymer monolith evolved with the reaction time under confinement (10-μm i.d. cpillary) by using thermal-initiated polymerization. Reaction time **A**: 20 min; **B**: 30 min; **C**: 60 min; **D**: 120 min. Polymerization conditions are the same as indicated in Figure 3.10. 87

Figure 3.12 The confinement effect was employed to achieve uniform, thick wall coatings in microchannels (**A**) and a capillary (**B**)-(**C**). Microchannel depth is 10 μm and width is 50 μm. The internal diameter of capillary is 10 μm. Polymerization conditions: HEMA 4 wt%, EDMA 6 wt%, toluene 90 wt%, benzoin 0.06 wt%, UV 312 nm for 10 min. Photografting: META 20wt%, tertbutyl alcohol 60 wt%, water 20 wt%, 4-(dimethylamino) benzonphenone 0.2 wt%, UV 312 nm for 120 s. 89

Chapter 4

Figure 4.1 Digital photo of one μCE device coated with polymer film based on confinement effect. Polymerization conditions: HEMA 4 wt%, EDMA 6 wt%, toluene 90 wt%, benzoin 0.06 wt%, UV 312 nm for 10 min. The film is invisible due to its thickness ~200 nm. 97

Figure 4.2 **A:** The fluorescent digital photo of a glass microchannel with half coated film. **B**: Intensity of fluorescence signal as a function of distance across the microchannel. Polymerization conditions: HEMA 4 wt%, EDMA 6 wt%, toluene 90 wt%, benzoin 0.06 wt%, UV 312 nm for 10 min. 100

Figure 4.3 **A**: Microfluidic scheme for μCE separation. 1: sample reservoir, 2: sample waste reservoir, 3: buffer reservoir, 4: buffer waste reservoir. **B**: Schematic illustration of photopatternable polymeric coatings based on the confinement effect and it was employed to achieve uniform, cationic thick wall coatings in microchannel shown in SEM image **C** by photografting. Conditions: HEMA 4 wt%, EDMA 6 wt%, toluene 90 wt%, benzoin 0.06 wt%, UV 312 nm for 10 min. Photografting: META 20wt%, tertbutyl alcohol 60 wt%, water 20 wt%, 4-(dimethylamino) benzonphenone 0.2 wt%, UV 312 nm for 120 s. **D**: SEM images showing the dependence of film thickness on monomer concentration. The polymerization was conducted in 10-μm internal diameter silica -fused capillaries and the recipe for each film thickness is indicated in Figure 4.4 A. ...103

Figure 4.4 **A**: The relationship between the film thickness and the monomer concentration. Monomer percentage = (HEMA+EDMA)/ (HEMA +EDMA+toluene), which varied from 0 wt% to 60 wt%. The ratio of HEMA: EDMA is fixed at 4:6. Each deviation is calculated from 10 batches of polymerization. **B**: SEM image showing the polymer morphology with component ratio lies in the gel-like structure range in Table 2.2. The polymerization was conducted in 10-μm internal diameter silica -fused capillaries. UV 312 nm exposed for 16 min. ...104

Figure 4.5 The reversed EOF magnitude affected by photografting time and the reproducibility of two-step photografting method. The deviation is from four batches of coatings. Polymerization conditions: HEMA 4 wt%, EDMA 6 wt%, toluene 90 wt%, benzoin 0.1 wt%, UV 312 nm for 10 min. Photografting: META 20wt%, tertbutyl alcohol 60 wt%, water 20 wt%, benzonphenone 0.2 wt%, UV 254 nm. The polymerization was conducted in 10-μm internal diameter silica-fused capillaries. The measurements were performed at room temperature with 20 mM phosphate buffer (pH7.0). ...106

Figure 4.6 **A**: EOF measured within glass microchannel responsed to the different buffer pH illustrating the surface coverage effect of the total coating process. Curves: (a) Activated glass microchannel, (b) Neutral HEMA-coated glass microchannel, (c) Cationic META photografted glass microchannel. The polymerization conditions were indicated in figure 4.3 C. **B**: The reproducibility of EOF produced by cationic META coating. The measurements were performed at room temperature with 20 mM phosphate buffer (pH7.0). Glass microchannel is ~24-μm wide and ~7-μm deep. ...109

Figure 4.7 Fluorescent images for pinched protein injection in HEMA polymer coated microchips. Protein concentration is 50 μM in 20 mM phosphate buffer (pH 9.0). **A:** Trypsin inhibitor injected in a 10-μm off double-T injector with 1000 V injection voltage. Other three reservoirs are grounded. **B**: BSA injected in a cross injector with 1000 V injection voltage. Other three reservoirs are grounded. ...111

Figure 4.8 Electropherograms of proteins with different injection times. **A**: BSA; **B**: IgG; **C**: Trypsin inhibitor. Proteins in 20 mM phosphate buffer (pH 9.0) were injected in a cross injector coated with HEMA polymer layer and the injection voltage is 1000 V. ...113

Figure 4.9 Plot of peak area/t_{migr} versus length of sample loading time for proteins in 20 mM phosphate buffer, pH 9.0. Electrophoretic conditions are the same as Figure 4.8. ...114

Figure 4.10 Electropherograms for protein separation under the influence of the separation length. The first peak is trypsin inhibitor and the second peak is BSA. The HEMA polymerization condition is the same as given for Figure 4.3, without photografting of META. Proteins were mixed in 20 mM Phosphate buffer (pH 9.0). Injection time is 10 s. ...116

Figure 4.11 Electropherograms of 20 repetitive runs for model protein separation. Microchannel was coated with neutral hydrophilic HEMA polymer film. The first peak is trypsin inhibitor and the second peak is BSA. Polymerization condition is the same as given for Figure 4.3, without photografting of META. Proteins were mixed in 20 mM Phosphate buffer (pH 9.0). Injection time is 10 s and the separation voltage is 300 V/cm. The separation length is 0.5 cm. ...117

Figure 4.12 Day-to-day reproducibility of migration time of proteins in neutral HEMA-coated microchannel. Conditions are the same as given in Figure 4.11. Peak 1: trypsin inhibitor. Peak 2: BSA. ...119

Figure 4.13 Electropherograms of 20 repetitive runs for protein separation based on neutral hydrophilic surface coating (HEMA) used for prevention of non-specific adsorption; the first peak is carbonic anhydrase and the second peak is trypsin inhibitor. Two runs are shown, offset on the y-axis for clarity. The HEMA polymerization condition is the same as given for Figure 4.3, without photografting of META. Proteins were mixed in 20 mM phosphate buffer (pH 3.0). Injection time is 8 s and the separation voltage is 150 V/cm. The separation length is 0.5 cm. ...122

Figure 4.14 Electropherogram for three model proteins separated within a HEMA polymer coated glass microchannel; the first peak is trypsin inhibitor, the second is ovalbumin and third is BSA. Proteins were mixed in 20 mM Phosphate buffer (pH 9.0). Injection time is 10 s and the separation voltage is 400 V/cm. The separation length is 1 cm. ...123

Figure 4.15 Electropherograms for separation of FITC-conjugated BSA digests whthin glass channel coated with (**A**) HEMA polymer layer and (**B**) HEMA polymer layer with SBMA photografting. Conditions: 20 mM Phosphate buffer (pH 9.5). Injection time is 10 s and the separation voltage is 700 V/cm. The separation length is 1 cm. The HEMA layer polymerization condition is the same as given for Figure 4.3. Photografting: SBMA 5 wt%, water 35 wt%, 1,4-butanediol 60 wt%, 4-(dimethylamino) benzonphenone 0.2 wt%, UV 312 nm for 150 s. ...126

Chapter 5

Figure 5.1 The scheme of immobilization procedure for covalent attachment of enzyme *via* epoxy group. ...133

Figure 5.2 The UV absorption profiles for photoinitiators. **A**: benzoin; **B**: 4-(dimethylamino) benzophenone. The graphy was adapted from website. ...135

Figure 5.3 Digital photo of polymer monoliths photopatterned within microfluidic devices. ...136

Figure 5.4 The top-view of the edge of polymer monolith cast in microchannel. The left dark part is monolith and right clear part is microchannel without monolith. **A**: the result from experiment. HEMA 16 wt%, EDMA 24 wt%, 1-octanol 60 wt%, Benzoin0.004 wt%, 312nm UV for 9 min. **B**: A result from literature [27]. 30%1,3-butanediol diacrylate, 0.5% AMPS, 0.3% trimethoxysilylpropyl acrylate, 6.92% lauryl acrylate, 62.28% butyl acrylate, and 0.5 wt % of the initiator AIBN. ...138

Figure 5.5 The top-view of the edges of polymer monoliths cast in microchannels for different bathes. The bottom dark part is monolith and top clear part is glass microchannel without monolith. The polymerization conditions are the same as indicated in Figure 5.4 A. ...138

Figure 5.6 The morphology and pore size distributions of monoliths with different surface chemistries. **A and C:** SEM image and pore size distribution of hydrophobic monolith, BMA 16 wt%, EDMA 24 wt%, 1-octanol 60 wt%, Benzoin 0.004 wt%, 312nm UV for 9 min. **B and D**: SEM image and pore size distribution of hydrophilic monolith, HEMA 16 wt%, EDMA 24 wt%, 1-octanol 60 wt%, Benzoin 0.004 wt%, 312nm UV for 9 min. 141

Figure 5.7 **A**: The morphology of the microreactor shown by SEM image; **B**: The pore size distribution of the microreactor measured by mercury intrusion porosimetry. The porosity is 78%. The recipe for the polymerization was list in Table 5.1. ...142

Figure 5.8 The stability of the flow resistance for microreactor measured over one week. The recipe was shown in Table 5.1. ...143

Figure 5.9 The m/z spectra of digested Cytochrome C by using trypsin immobilized monolithic microreactor. The length of the monolithic bed is 7 mm. The residence time is 180 s. The residues position is labeled on the top of the assigned peak. The sequence coverage is calculated as 78%. No auto-digested trypsin fragment peaks were found. ...145

Figure 5.10 The m/z spectra of digested Cytochrome C by using trypsin immobilized monolithic microreactor. The residence time is 60 s. The residues position is labeled on the top of the assigned peak. The sequence coverage is calculated as 45.2%. No auto-digested trypsin fragment peaks were found. ...146

List of Abbreviations

AIBN	2,2′-Azobis(2-methylpropionitrile)
BMA	Butyl Methacrylate
CE	Capillary Electrophoresis
CEC	Capillary Electrochromatography
2D	Two-dimensional
3D	Three-dimensional
EOF	Electroosmotic Flow
ESI	Electrospray Ionization
EDMA	Ethylene Dimethacrylate
GMA	Glycidyl Methyacrylate
HPLC	High Performance Liquid Chromatography
HCCA	α-Cyano-4-hydroxycinnamic Acid
HEMA	2-Hydroxyethyl Methacrylate
LIF	Laser-induced Fluorescence
LSCM	Laser Scanning Confocal Microscope
μCE	Microchip-based Electrophoresis
META	[2-(Methacryloyloxy) ethyl]- trimethylammonium Chloride
MALDI	Matrix-assisted Laser Desorption and Ionization
MS	Mass Spectrometry
PMT	Photomultiplier Tube
PDMS	Polydimethylsiloxane
RSD	Relative Standard Deviation
SPE	Solid Phase Extraction
SEM	Scanning Electron Microscope
SBMA	Sulfobetaine Methacrylate
SDS-PAGE	Sodium Dodecyl Sulfate Polyacrylamide Gel Electrophoresis

List of Structural Formulas

2-hydroxyethyl methacrylate

(HEMA)

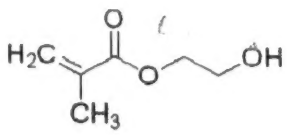

butyl methacrylate

(BMA)

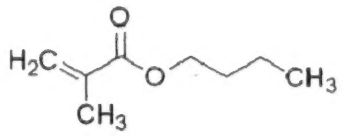

glycidyl methacrylate

(GMA)

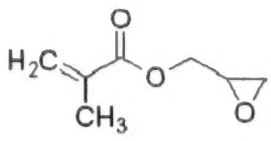

[2-(methacryloyloxy) ethyl]-trimethylammonium chloride

(META)

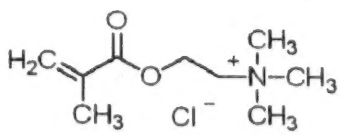

ethylene dimethacrylate

(EDMA)

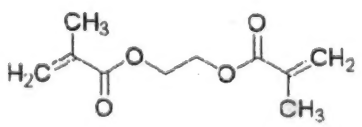

sulfobetaine methacrylate

(SBMA)

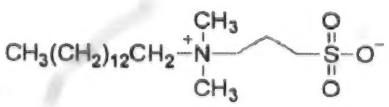

2,2′-azobis(2-methylpropionitrile)

(AIBN)

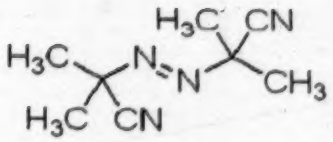

4-(dimethylamino)benzophenone

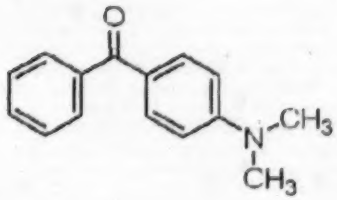

benzoin

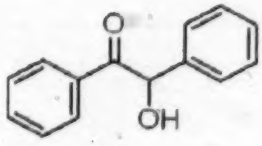

3-(trimethoxysilyl)propyl methacrylate

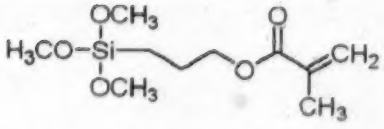

triethoxy(octyl)silane

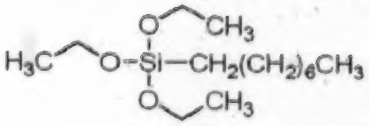

1-[3-(trimethoxysilyl)propyl] urea

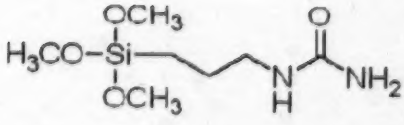

Chapter 1

Introduction

1.1 BACKGOUND AND MOTIVATION

1.1.1 Lab-on-chip Devices for Bioanalysis

Microfluidics, the science and technology of manipulating and processing small amount of fluids (10^{-9} to 10^{-18} litres) in channels with dimensions of several to hundreds of micrometers, has emerged as an exciting new field [1-5]. It offers a number of advantages: the ability to use very small quantities of samples and reagents, and to carry out separation and detection with high resolution and sensitivity [6], low cost [7-9], short time for analysis [10-12], and reduced dimensions compared with other analytical devices. Such devices may provide higher efficiency for new fundamental research [13]. Rapid development of new fabrication methods and functional components has been witnessed over the last few years, with development of valves [14-17], micromixers [18-21] and pumps [22, 23]. These elements are essential to achieve fully integrated microchemical 'laboratories' on a chip. The development of soft lithography makes it possible to fabricate prototype microfluidic systems for quick testing of ideas in a short period of time (typically less than one day), and to allow for massive replication of microdevices in several hours [24]. Microfluidics offers an enabling platform, which has given rise to marked scientific and technological advances in numerous research areas spanning from chemical synthesis and biological analysis to optics and information technology.

A particularly beneficial characteristic of lab-on-chip devices is to provide a miniaturized platform for probing biological systems. The volumes of samples and reagents that are needed are quantitatively small, and consequently, the waste is also minimized, which is particularly important when working with biologically hazardous material. Most importantly, microfluidic and nanofluidic tools possess dimensions compatible with biological samples, which allow efficient and sensitive interrogation of fundamental biological processes at a single cell and even single molecule level [2, 3]. For instance, the Zare group reported a microfluidic device which allows sophisticated cell manipulation and provides extremely high sensitivity detection of proteins (present at fewer than 1000 molecules per cell) [25]. This single-cell analysis chip for mammalian and insect cells, shown in Figure 1.1 A, is made of polydimethylsiloxane (PDMS) and has three sections: cell manipulation, electrophoretic separation, and single-molecule fluorescence counting of protein contents of a single cell. Han *et al.* invented a microfabricated DNA separation device composed of an array of nano-gaps to interact with biological macromolecules, as sketched in Figure 1.1 B [26]. The deep trenches serve as entropic traps to retain DNA coils based on their hydrodynamic sizes. Such nanofluidic filter arrays can also be used to achieve rapid separation of short DNA and SDS-denatured proteins. Reducing physical dimensions down to micrometer and nanometer scales fundamentally alters the fluidic dynamics, mass transfer, and other physical properties within micro-/nano-devices, resulting in numerous novel applications [27]. Figure 1.1 C presents a microfluidic network that consists of a series of microchannels to create concentration gradients with appropriated step size [28]. This device is based on laminar flow at low Reynolds number, in which fluidic mixing only

occurred by diffusion of molecules across the interface. As the physical dimensions of channels decreased, their surface-to-volume ratio increased, and the rate of heat and mass transfer was dramatically increased [29, 30]. Those distinctive phenomena are motivating various chip-based methods in which analyses can be carried out more rapidly and at lower cost via small-scale systems than with current laboratory bench-scale methods.

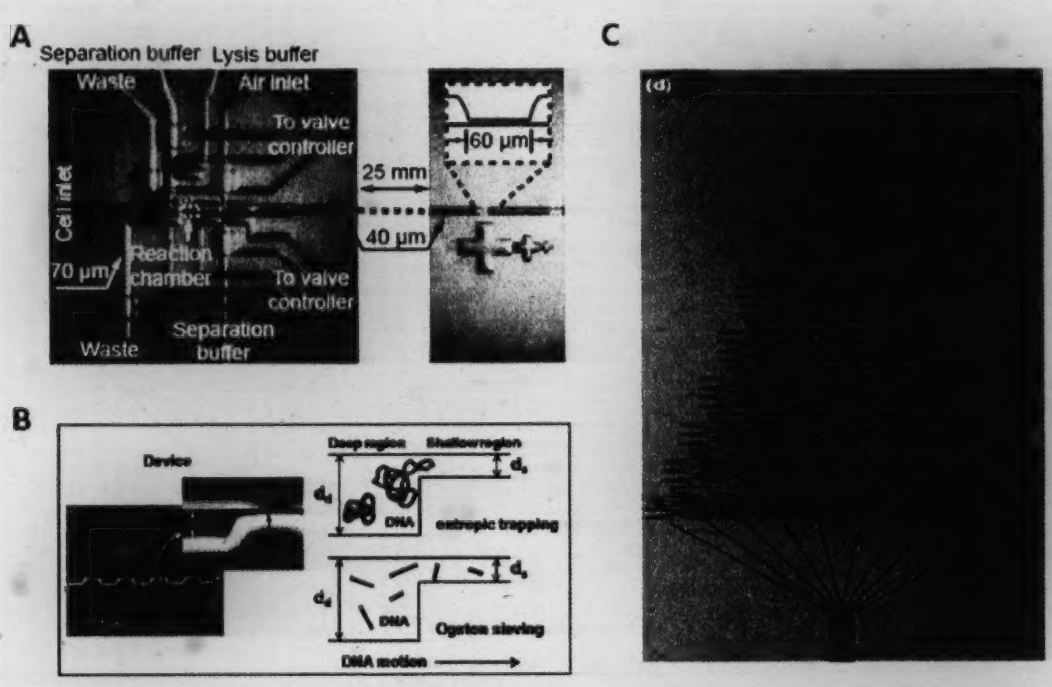

Figure 1.1 Miniaturized microfluidic and nanofluidic devices. **A**: Layout of a PDMS microchip for single-cell analysis, showing the cell-manipulation section on the left and the molecule-counting section on the right [25][1]. Pneumatic valves were integrated to sequentially control single cell injection and capture. **B**: A nanofluidic filtering structure for separating both DNA and protein molecules (left) based on two distinct mechanisms: entropic trapping for long, flexible DNA chains (right top) and Ogston sieving for short, rigid DNA fragments and SDS-denatured proteins (right bottom), adapted from [26]. **C**: A complex microfluidic network used to generate a concentration gradient profile across the channel based on the diffusion in laminar flow [28][2].

1. Copyright © 2008 by American Association for the Advancement of Science
2. Copyright © 2008 American Chemical Society.

Another driving force in lab-on-chip technology is the integration of parallel elements and/or various functional components, which has equipped lab-on-chip devices with unprecedented capability in terms of analysis throughput, sophistication of operation, and automation. In turn, device integration leads to further miniaturization of laboratory instruments. For example, the Quake group developed a scheme for metering and mixing fluids on the picoliter scale, as shown in Figure 1.2 A, which is scalable to highly integrated parallel architectures [31]. The chip has 480 active valves and performs 144 parallel reactions, each of which consumes only 10 nl of protein sample. This device was employed for rapid on-chip screening of protein crystallization conditions, trapping droplets containing proteins in microchambers, to give faster crystal growth, and thus a higher hit rate than conventional techniques. The dimension of the complete device is only about the size of a penny, as seen in Figure 1.2 A inset. The Ismagilov group invented a microsystem containing a PDMS microfluidic droplet generator composited with a glass capillary (Figure 1.2 B) [32]. This composite device employs continuously produced droplets as individual microreactors for protein crystallization, and enables continuous and direct X-ray diffraction analysis of protein crystals formed in the droplets flowing through the capillary. Microfabrication also allows easy and economical scaling from single units to complex networks and arrays to perform many experiments in parallel, as well as for mass production [33].

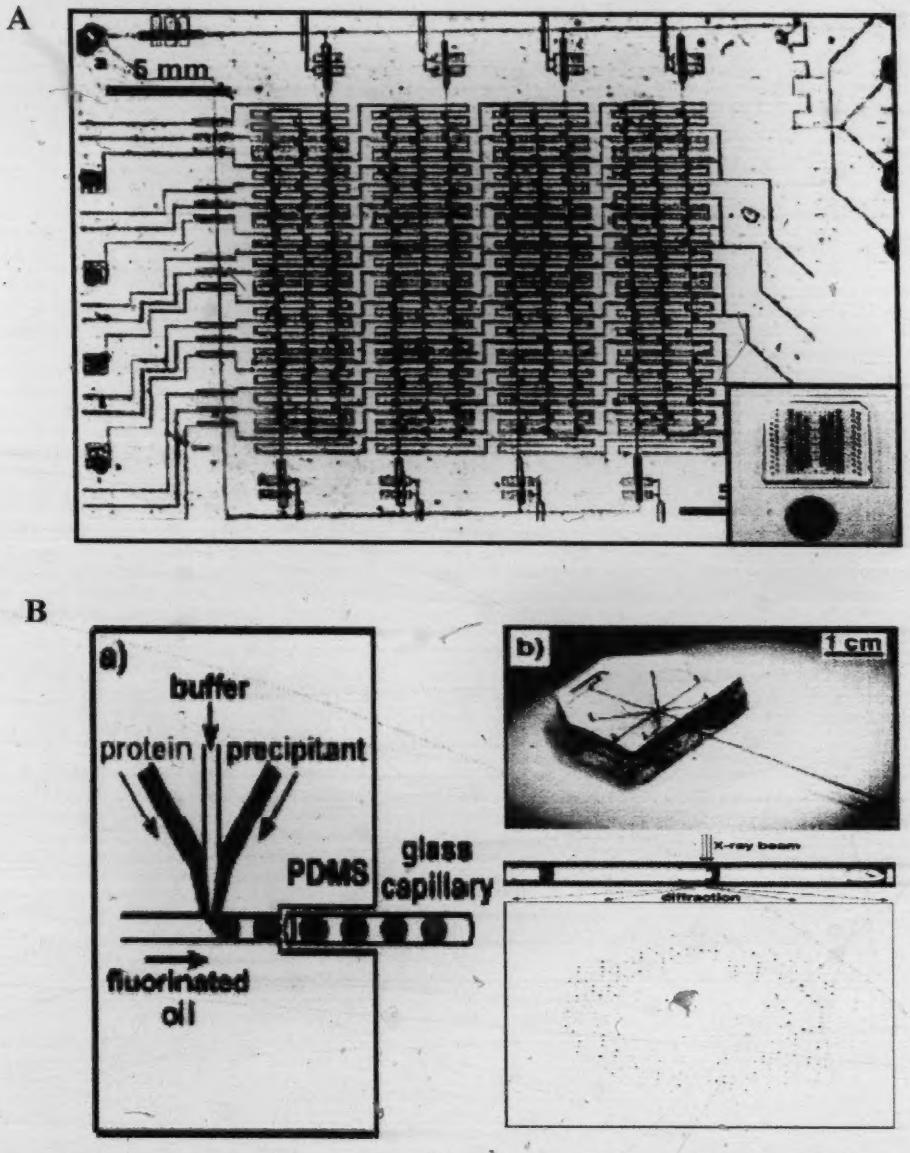

Figure 1.2 Microfluidic systems for high-throughput screening of protein crystallization conditions. **A**: A large-scale integrated device containing 480 active valves and 144 parallel reaction chambers [31][3]. The inset shows the real size of the device. **B**: A microdroplet generator coupled with a capillary for on-line X-ray detection [32][4]. Left: the schematic illustration of reagent mixing and droplet formation; right: A photograph of the real composite PDMS device (top) as well as the protein crystals formed in the individual droplets and a representative x-ray data (bottom).

---

3. Copyright © 2008 by the National Academy of Sciences of the United States of America.
4. Copyright © 2008 WILEY-VCH Verlag GmbH & Co. KGaA, Weinheim

The miniaturization and integration of lab-on-chip devices rely on the development of the functional components for sample introduction, pumping, sorting, mixing and metering fluids, etc. The invention of a simple PDMS-based valve [34] has markedly driven the automation of microfluidic operation and enabled numerous applications in biological science and engineering [25, 31, 35, 36]. Herr *et al.* implemented a microfluidic device for multiple sample pretreatment and analysis steps, including filtering, concentration, mixing, as well as electrophoretic protein separation, using multistep-photopatterned polyacrylamide hydrogel [37]. This point-of-care diagnostic microsystem has been demonstrated to conduct hands-free immunoassay analysis of human saliva samples.

The separation matrix is one of the most important functional elements in microfluidic applications. Compared to conventional chemical media used to fill the microchannels, the micro/nanomachined structures possess advantages such as regular and precisely engineered geometry, mechanical robustness, and ease of integration [38, 39]. Figure 1.3 presents two typical micrometer-sized structures of different geometries, which were produced by plasma etching [40] or imprinting in a PDMS substrate [41]. However, practical applications of such micro/nanomachined structures are still largely impeded by current technical limitations of nanolithography, such as very high cost, tedious fabrication steps, and challenges in fabrication at 10-nm length scales [42, 43]. Therefore, conventional chemical materials still hold the dominant position in the application of microfluidic devices.

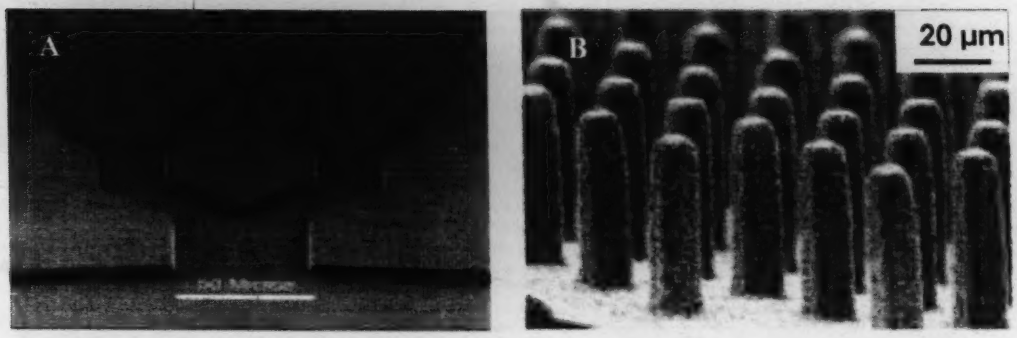

Figure 1.3 Micromachined separation matrix structures. **A**: A 10-µm thick monolithic column microfabricated by reactive ion etching on quartz for microchip-based liquid phase chromatography [40][2]. **B**: An array of micropillars made by replication from a PDMS mould, adapted from [41].

1.1.2 Functional Chemical Materials for Lab-on-chip Integration

Functional chemical materials used in microfluidic systems are organic gels, beads and polymer monoliths, which are typically inexpensive chemicals and have flexible functional chemistries. Soft gels are used for separating and immobilizing species in microchannels. They can be used to provide hydrodynamic resistance, to eliminate cross flow, and to balance pressure between channels [44]. Herr *et al.* designed a microfluidic chip with photopattened hydrogels for SDS-PAGE analysis of protein, as shown in Figure 1.4 [45]. Two polymeric gel elements, a thin (~50 µm) size exclusion membrane for preconcentration and a long gel column for protein sizing, were fabricated *in-situ* using photopolymerization. The size exclusion membrane was polymerized in the injection channel using a shaped laser beam, and the separation gel was cast by photolithography using a mask and UV lamp. Contiguous placement of the two polymeric elements in the channels of a microchip enabled simple and zero dead volume integration. The protein preconcentration and separation were performed sequentially, as demonstrated in Figure 1.4 B–D.

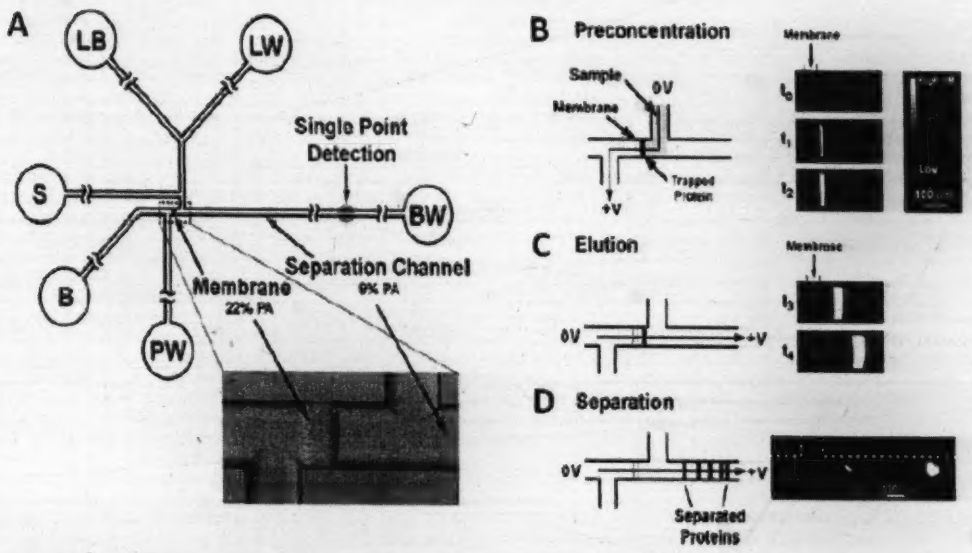

Figure 1.4 Integrated SDS-PAGE microchip with sample preconcentrator based on photopatterned cross-linked polyacrylamide gel [45][2]. **A**: Chip layout. The inset shows a bright-field image of a photopolymerized size exclusion membrane (visible due to light scattering) positioned in the offset-T junction. **B–D**: Schematic and fluorescent images of sequential process of protein analysis by switching electric fields applied to the reagent reservoirs, including preconcentration, elution, and separation.

Conventional polymer gels, however, suffer from some common disadvantages, such as low mechanical strength, high swelling ratio and low tolerance for strong organic solvents and extreme pH. These drawbacks impede their application to fluidic systems requiring pressure and harsh buffer conditions. Commercially available chromatographic beads have much stronger rigidity and defined geometry. The wide range of sizes and flexible chemistry properties has made beads ubiquitous in immunoassays, reactor beds, and chromatography. Currently, most packing techniques need frit or weir structures to trap beads into the specific area. For example, in Figure 1.5 A, our group designed two weirs within a sample channel to form a cavity to retain the silica beads pumped by electroosmotic pumping [46]. This technique allows the beads in the cavity to be

repeatedly exchanged. Electrochromatography and solid phase extraction have been realized by integrating bead-packed beds into microfluidic chips [47]. A similar packing technique was developed by Masaki *et al.*, as shown in Figure 1.5 B, by filling silica gel beads into a microchannel that had a dam structure [48]. This device was used to perform cleanup for polycyclic aromatic hydrocarbons from diesel exhaust particles.

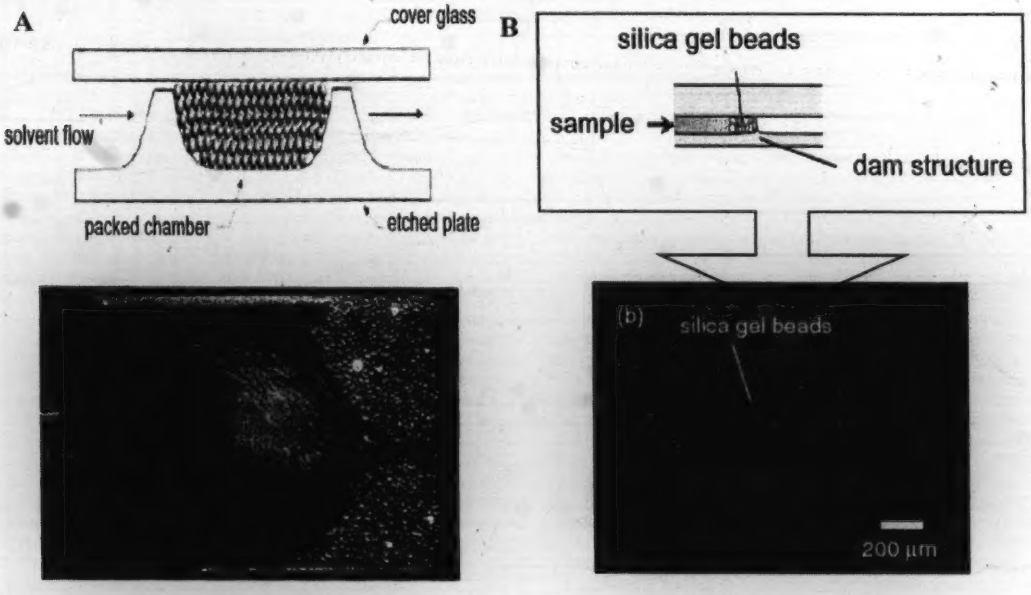

Figure 1.5 Packing beads in microfluidic chips. **A**: Schematic and video images showing electrokinetic packing process using dual weir structures [47][2]. **B**: Schematic and photograph of microchannel packing silica gel beads within a microchannel with a dam structure, adapted from [48].

Polymer monoliths share many of the benefits of packed chromatographic beads, including high surface area and easily controlled surface chemistry. In addition, they present distinct advantages for microfluidic applications. Monolithic beds can be easily and rapidly prepared via free radical polymerization within the channels of the microdevice without need for frits or other retaining structures. The porosity, surface area, and pore size of the monolith are controlled by adjusting the composition of the

initial monomer solution and the polymerization conditions. A wide range of functional groups can be photografted onto the surface of the monolith. Most interestingly, polymer monoliths can be lithographically defined in one step in the desired location of the microchannel. The highly porous structure of monoliths leads to lower back pressure compared to bead packing. Indeed, high pressure drops may cause the failure of the bonding between the top and the bottom chip wafers and cannot be provided by on-chip pumping system [49].

Polymer monoliths have received tremendous interest in microfluidic applications, some of which will be exemplified below. A sequential photografting technique was developed to fabricate an alternating array of two kinds of enzymatic microreactors, which is shown in Figure 1.6 A [50]. Multiple enzymes were photopatterned on one porous polymer monolith within a microfluidic device to perform spatially separated multi-enzymatic reactions. Thomas Rohr *et al.* designed a simple and efficient micro-mixer using a highly porous monolithic bed prepared by direct photo-polymerization in the channels of a microfluidic chip, as seen in Figure 1.6 B [51]. Best mixing results were achieved with a monolithic mixer containing very large irregular pores. Polymer monoliths have also been popularly employed as the solid phase for chip-based electrochromatography. Figure 1.6 C demonstrated one such device fabricated by the Singh group for rapid separation of peptides [52]. The Landers group implemented a two-stage, dual-phase microdevice for highly efficient DNA purification from submicroliter volumes of whole blood [53]. This method uses a C_{18} reverse phase to remove protein contents in the blood sample first, followed by DNA extraction using a photopolymerized monolithic column. This purification process shows good device-to-device

reproducibility, demonstrated by the DNA extraction profile as well as the electrophoretic sizing in Figure 1.6 D. Photopatterning allows ready scale-up to fabricate large-scale arrays of parallel polymer monolithic beds for high-throughput processing of biological samples. For example, Jane Wang *et al.* designed a microfluidic device patterned with 36 polymer beds for sequential protein preconcentration, which was shown in Figure 1.6 E [54]. In addition to their chemical functionalities, polymer monolith structures can be used as mechanical parts in microfluidic operations. The Kirby group developed a mobile polymer monolith by creating a non-stick moving polymer part inside a microfluidic channel to perform a piston-based function [55, 56]. This valving technology allowed the construction of an integrated HPLC system on a microchip, illustrated in Figure 1.6 F, which is capable of working under high pressure (>30 M Pa) for the rapid separation of peptides and proteins with high reproducibility (retention time RSD = 0.03%) [55]. This technique also makes it possible to build various valves and fluidic controlling elements for microfluidic integration.

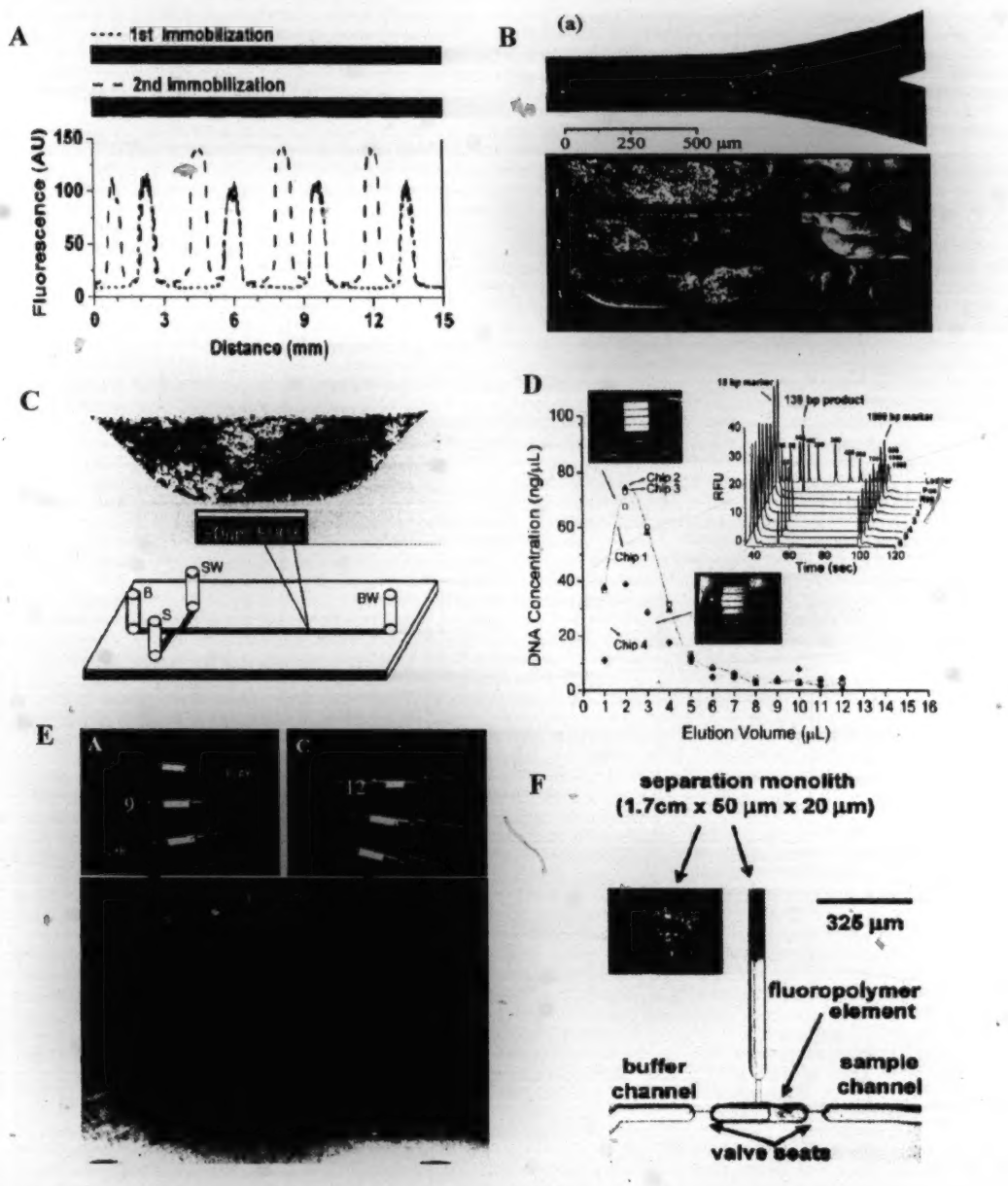

Figure 1.6 Multifunctional integration of photopolymerized monolith within microfluidic chips. **A**: Sequential enzyme immobilization [50][2]. **B**: Monolithic mixer [51][4]. **C**: Monolithic solid phase for microchip-based electro-chromatography separation [52][2]. **D**: Two-stage, dual-phase microdevice with photopatterned monolithic column for DNA extraction [53][2]. **E**: Monolithic beds array for protein preconcentration, adapted from [54]. **F**: Mobile polymer monolith for valve control in microchip HPLC separation [55][2].

1.1.3 Motivation and Scope of the Thesis

Because conventional beads are widely available, well characterized, and easily functionalized, they have become a popular choice as the packing materials in microfluidic systems. Uniform and reproducible packing of beads in the channels of a microchip, however, represents a significant technical challenge. In addition, packing a complex microfluidic manifold is difficult and higher back pressure is needed for packing longer bed. Those technical difficulties have hindered the utilization of beads within microfluidic devices, especially for multiplexed microsystems. Our group devised a multiplexed microfluidic platform of 20 channels in parallel for high-throughput and automated proteomic applications, which is shown in Figure 1.7 [57, 58]. A series of protein processing stages are incorporated into this microsystem, as outlined below. A protein mixture is introduced into the capillary and then separated by isoelectric focusing. By sequentially grounding the electrodes connected to each channel, each protein fraction is driven into the individual microchannel which contains a trypsin bed for enzymatic digestion and a solid phase extraction bed for preconcentration of digests. Concentrated digests are then sequentially eluted out and subjected to ESI-MS analysis. Both digestion and solid phase extraction beds were packed using beads. It proved to be extremely challenging to pack all 40 beds uniformly enough that the flow rate in the channels is predictable for sequential delivery of samples. An alternative method is highly desired for fabricating well controlled bed packing, which is the initial motivation for this thesis. Specifically, we seek to employ photopolymerized polymer monoliths, as an inexpensive and effective alternative to classic silica beads, in order to obtain stable and reproducible

flow resistance. Reproducibility is an essential requirement for the sequential operation of our multiplexed protein processor designs.

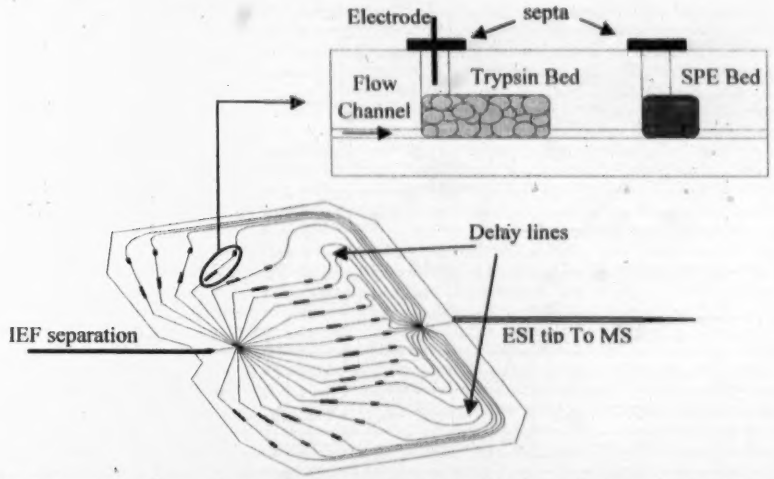

Figure 1.7 Microfluidics Platform for multiplexed protein analysis. Top: side-view of one of the 20 microchannels in platform. Bottom: The design of the protein processing platform coupled with ESI-MS. Adapted from Taylor *et al.* [58].

This thesis concentrates on systematic investigation of photopolymerization conditions and the related fluidic properties of various polymer monoliths patterned within microfluidic chips, and explores their applications for separation science and proteomics. During our studies, we found that the physical confinement of microchannels induces significant spatial variation of monolithic structures, which leads to a new strategy to manipulate the morphology of polymer monolith within micrometer-scale confinement. We have demonstrated that this new approach can be employed to achieve robust, thick-film coatings of microchannel walls as well as its application in separation of biomolecules, including both peptides and proteins.

The thesis is organized as described below:

Chapter 2 characterizes the properties of monolithic beds photopatterned within microfluidic channels in terms of the fluidic stability and reproducibility. Polymeric

monoliths were selectively patterned within microchannels with a wide range of reagents and reaction conditions and their flow resistance was evaluated using a photobleaching, time of flight, linear flow rate measurement method. The polymerization conditions, including porogenic solvent, monomer composition, and photo-exposure time, have been optimized to obtain monolithic beds with good flow stability and reproducibility. The RSD of the flow stability was less than 4% over 7 days for monoliths prepared with 60-80 wt% crosslinker/ (monomer + crosslinker). The results obtained in this study provide highly useful guidance for patterning uniform polymeric monolithic beds, which are critical for their applications in multiplexed microfluidic systems, such as parallel functional arrays.

In Chapter 3, we show that the morphology of porous polymer monoliths photopatterned within capillaries and microchannels is substantially influenced by the dimensions of confinement. Porous polymer monoliths were prepared by UV-initiated free-radical polymerization using either hydrophilic or hydrophobic monomers, crosslinker and different porogenic solvents. These mixtures produce bulk pore diameters between 3.2 and 0.4 μm. The extent of deformation from the bulk-polymerized porous structure under confinement strongly depends on the ratio of characteristic length of the confined space to the monolith pore size. Bulk-like porosity is observed for a confinement dimension to pore size ratio > 10, and significant deviation is observed for a ratio < 5. At the extreme limit of deformation a smooth polymer layer is formed on the surface of the capillary or microchannel. Surface tension or wetting also plays a role, with greater wetting enhancing deformation of the bulk structure. The films created by

extreme deformation provide a rapid and effective strategy for robust wall coating, with the ability to photograft various surface chemistries onto the coating.

In Chapter 4, we discuss using the observed confinement effect for preparing relatively thick (~ 300 nm) and uniform surface coatings for microfluidic devices. The preliminary polymer coating can be further modified with various chemical functional groups. Here we first coated the glass microchannel with a neutral polymer layer of 2-hydroxyethyl methacrylate (HEMA), and then photografted functional groups with or without charges to manipulate electroosmotic flow (EOF). This thick-film coating was then assessed for the electrophoretic separation of proteins in terms of efficiency and reproducibility. This coating method minimizes protein absorption onto the glass wall, giving very high separation efficiency. Long-term measurements showing the reproducibility of protein separations proved the durability of this thick coating. Overall, our coating method is robust and easy to perform, requiring a total preparation time less than 10 min. It can be subsequently modified with various surface functional groups to achieve complex photolithographically defined patterns.

Chapter 5 systematically investigates the experimental conditions for patterning of photopolymerized monoliths within microscale channels, which include the photopattern resolution, surface chemistry selection, pore structure control and porogenic solvent selection. The conditions were optimized to establish a fast and easy protocol for patterning porous monoliths for enzymatic microreactor applications. The conditions for trypsin immobilization on the surface of the porous monolith and the digestion efficiency in patterned microreactors with stable flow resistance were evaluated.

Chapter 6 concludes the present progress of this work and discusses the future perspectives.

To facilitate our discussion, it is helpful to briefly review some important aspects of photopolymerized monoliths and microchip electrophoresis separation, which is the main purpose of Sections 1.2 and 1.3.

1.2 Photopolymerized Polymer Monolith

Porous polymer monoliths have received tremendous interest in many applications since they were first used in chromatographic tubes in the late 1980s [59-61]. UV initiated polymerization for monolith preparations was shown in the late 1990s [62, 63]. Polymer monoliths have a distinct bicontinuous structure, which is formed during polymerization of a mixture of monomer, crosslinker, porogenic solvent and initiator. This molded rigid porous structure persists permanently even in the dry state [64]. The internal structure consists of numerous interconnected cavities (pores) of different sizes, and structural rigidity is secured through extensive crosslinking. Figure 1.8 shows a typical example of the structure of a monolith prepared by photo-initiated polymerization. The structure consists of numerous microglobules which aggregate and crosslink to form larger aggregates. The flow-through macropores between the large aggregates and the intermediate pores between microglobules together contribute to the characteristic pore size of the polymer monolith [65-67].

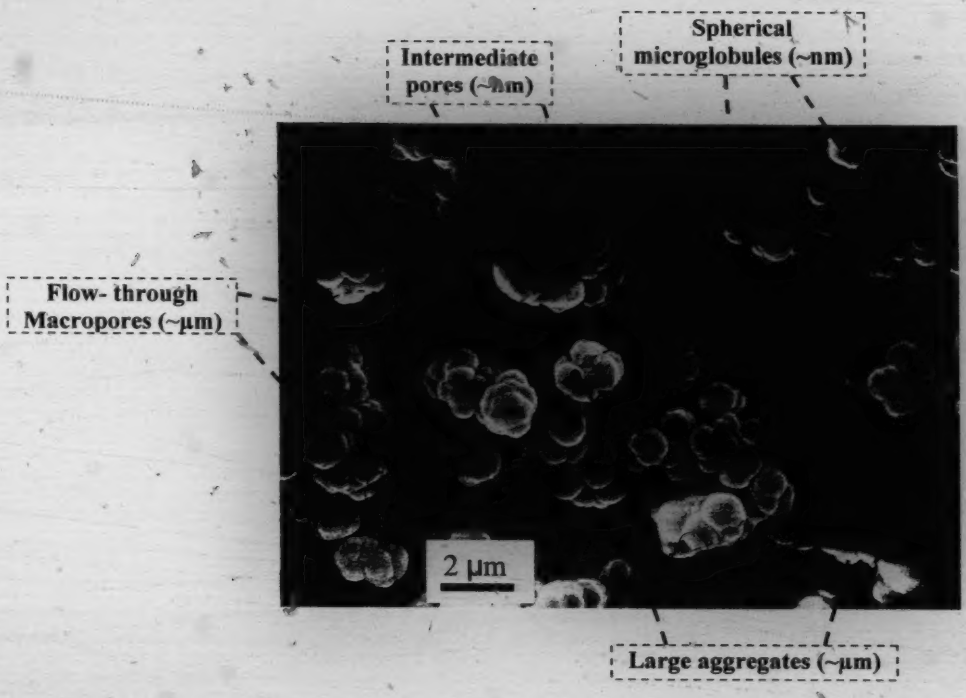

Figure 1.8 SEM image showing the structure of a porous polymer monolith in dry state.

Most polymer monoliths are based on styrene-divinylbenzene and/or methacrylate copolymerization. Most monomers and crosslinkers used for monolith polymerization are listed in Figure 1.9. Each monomer contains a functional group for control of the surface chemistry of the monolith columns. An example is HEMA, which contains the hydrophilic hydroxyl functional group. This copolymerization system for the production of porous monolith includes a monovinyl monomer, a divinyl monomer (crosslinker), an initiator, and the inert diluent. The decomposition of the initiator by UV light exposure or heating produces free-radicals, which initiate polymerization between monomers (see Session 1.2.1 and Figure 1.10). After a certain reaction time, a three-dimensional network

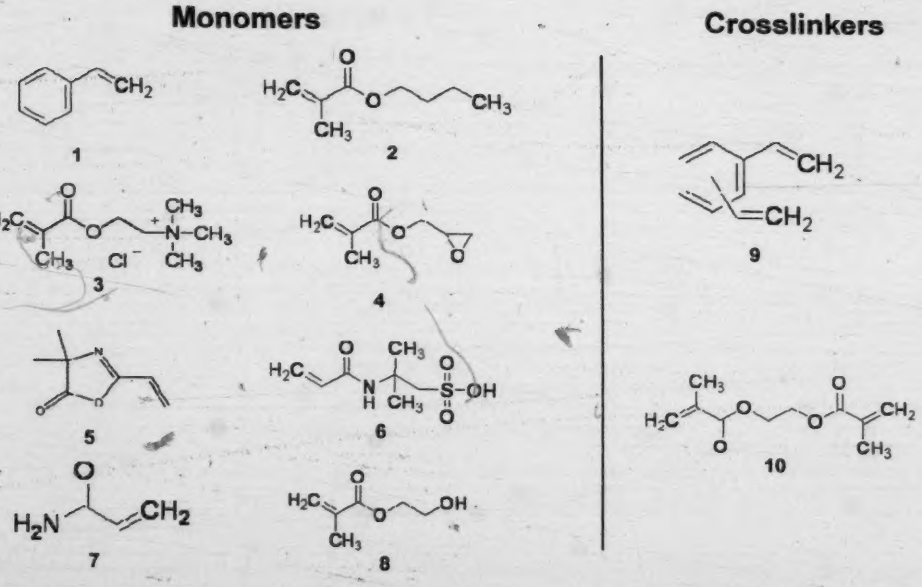

Figure 1.9 The monomers and crosslinkers used for polymerization of porous monoliths. **1**: Styrene; **2**: Butyl methacrylate; **3**: [2-(methacryloyloxy) ethyl]-trimethylammonium chloride; **4**: glycidyl methacrylate; **5**: vinyl azlactone; **6**: 2-acrylamido-2-methyl-1-propanesulfonic acid; **7**: Acrylamide; **8**: 2-hydroxyethyl methacrylate; **9**: divinylbenzene; **10**: ethylene dimethacrylate

of very large size may start to form, which creates a structure having dimensions approaching that of the containing vessel. At this point, the system (monomer–diluent mixture) changes from a liquid to a solid-like state, due to the low solubility of the polymer. Continuing polymerization and crosslinking reactions decrease the amount of soluble component, by increasing the crosslinking density of the network. After complete conversion of monomer to polymer, only the network and the diluent remain in the reaction system. The classical mechanism of pore formation that occurs during the polymerization process depends on the type of porogen used for the reaction. In this process, the monomers are better solvating agents for the polymer than the porogen. Therefore, the initiated nuclei are precipitated and enlarged by their continuing

polymerization and by capturing other branched or even crosslinked polymer formed in the solution. Eventually, nuclei are associated into clusters held together by polymer chains that crosslink the neighbouring nuclei. The clusters remain dispersed within the inert solvent, therefore forming a scaffold-like interconnected matrix within the polymerizing system. The interconnected matrix becomes reinforced by crosslinking, which leads to the final porous polymer body. The inert solvent remains trapped in the voids of the crosslinked polymer [68-72].

This mechanism of pore formation during polymerization in the presence of porogens does not yet allow a prediction of the sizes of the pores that should result. The current knowledge of factors that control pore size in porous polymers is mostly empirical [73]. The polymer phase separates from the inert solvent during the polymerization because of its limited solubility in the mixture. It occurs at an earlier stage by addition of a poorer solvent in the polymerizing system, which results in better coalescence of many nuclei and further increase in their size. Overall, the globules that are formed in such a system are larger and, consequently, the voids (pores) between them become larger as well [74].

1.2.1 Photo-initiated Free Radical Polymerization

In free radical polymerization, photoinitiators absorb incident light and undergo the homolytic decomposition in the excited state to produce free radicals [75]. For example, benzoin decomposition under UV exposure can be described as follows [76]:

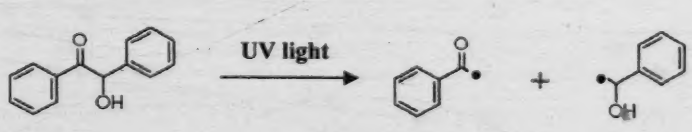

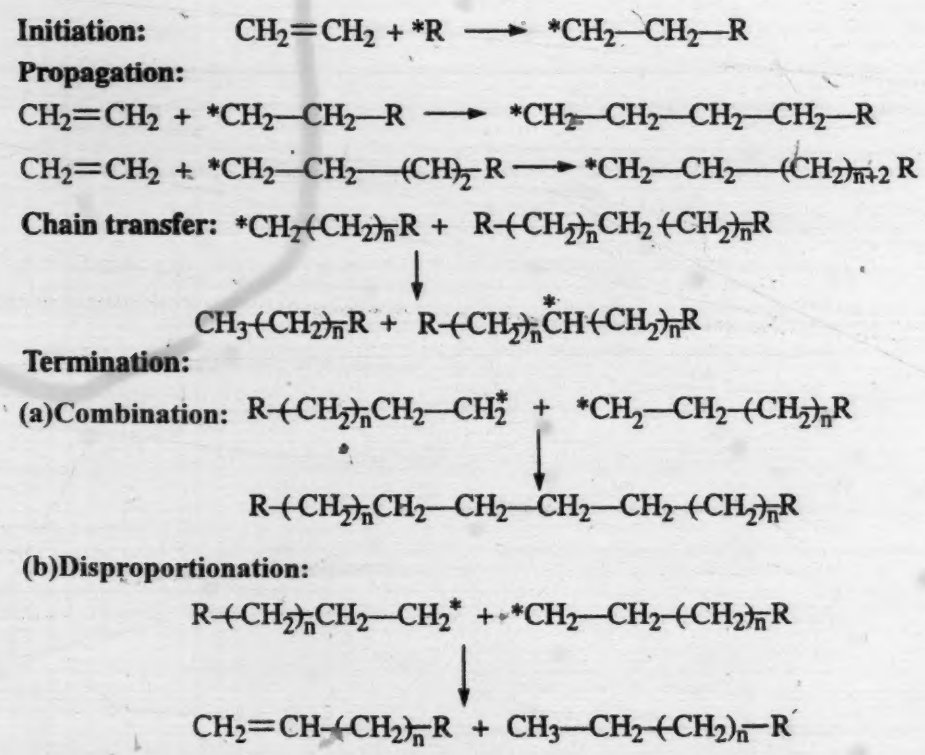

Figure 1.10 Mechanism of free radical polymerization, adapted from [77]. R is the radical formed by the decomposition of photoinitiator.

The monomers usually contain at least one double bond that participates in the reaction by accepting or adding the free radical. For example, the mechanism of polymerization of polyethylene is illustrated in Figure 1.10, and consists of three steps, named initiation, propagation and termination. The free radical produced from the initiator is accepted and added to the double bond of the monomer. The activated monomers keep attacking other monomers or crosslinkers. The polymer chain keeps extending by continuously adding monomers. Chain transfer starts a new chain growing out of the middle of the long polymer chain and results in a branched chain. Monomers are often combined with a crosslinker, which usually contains at least two double bonds, to form cross-linked polymer networks. Chain growth can be terminated by a combination of two growing

polymer chain, by disproportionation of chains [77, 78], or by reaction with impurities that quench the radicals.

1.2.2 Photografting

The grafting of solid surfaces with layers of polymer has become a very important technique used in numerous areas, such as microelectronic packaging and functional membranes [79]. In these applications, surface grafting enables the introduction of specific groups, while also preserving the bulk and structural properties of the underlying material, by a post-polymerization step such as UV initiation. This post-polymerization makes monomer units with the desired functionalities reacted with the underlying surface. This step is extremely versatile, as it allows independent control of the porous structure obtained in the initial polymerization step. The attachment of chains of reactive polymer to the surface site provides multiple functionalities. This grafting process also enables the control of both location and to some extent, quantity of functional groups, since the exposure to light can be controlled both spatially and temporally [80, 81]. An appealing approach involves the packing of channels with porous materials, as this significantly increases the available surface area and enables the introduction of specific chemistries into the device. In particular, the grafting of polymer surfaces could considerably increase their functional capabilities [82]. Fréchet and other research groups used this technique to create axial gradients of functionalities for multi-enzymatic reactions and pH gradient separation [83-85].

Usually, benzophenone has been used as photoinitiator for photografting, combined with the functional monomer and solvent. Benzophenone absorbs the UV light, forms

free radicals and abstracts a hydrogen from the substrate surface. The radical formed on the surface adds to a monomer in solution, leading to grafted chains [86, 87]. This grafting reaction is fast and gives a very thin layer of grafted polymer (< 10 nm) in a few seconds, with no, or very small effects on the bulk substrate. Figure 1.11 illustrates the proposed grafting process used by Rhor *et al.* [88]. Initially, only a limited number of polymer chains grow from the surface (see Figure 1.11 A). As the polymerization continues, the degree of branching increases since grafting also occurs via H-abstraction from the already grafted chains. As the density of chains increases, crosslinking becomes increasingly prevalent, and finally, a dense crosslinked polymer network is formed.

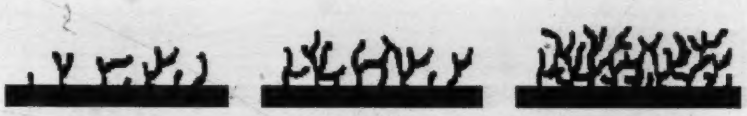

A: chain growth B: branching C: cross-linking

Figure 1.11 Schematic representation of the growing polymer chains during photografting with increasing irradiation time from A to C, adapted from [88].

1.3 Capillary Electrophoresis and Capillary Electrochromatography

1.3.1 Capillary Electrophoresis

Electrophoresis has become one of the most important tools for separation since its discovery. A number of techniques based on electrophoresis have been established, among which capillary electrophoresis (CE) features high speed, low sample consumption, high separation efficiency, and sensitive detection. In traditional capillary electrophoresis, analytes move in a conductive liquid medium in a silica-fused capillary under the influence of an electric field. Separation is based on the differential movement

of analytes in an electric field [89]. The mobility for an ion is constant in a given medium, which is defined by

$$\mu = z/(6\pi\eta r) \qquad (1.1)$$

where z is the net charge of the analyte, r is the radius of the analyte and η is the viscosity of the buffer solution. The velocity of migration of an analyte in capillary electrophoresis will also depend upon the rate of electroosmotic flow (EOF).

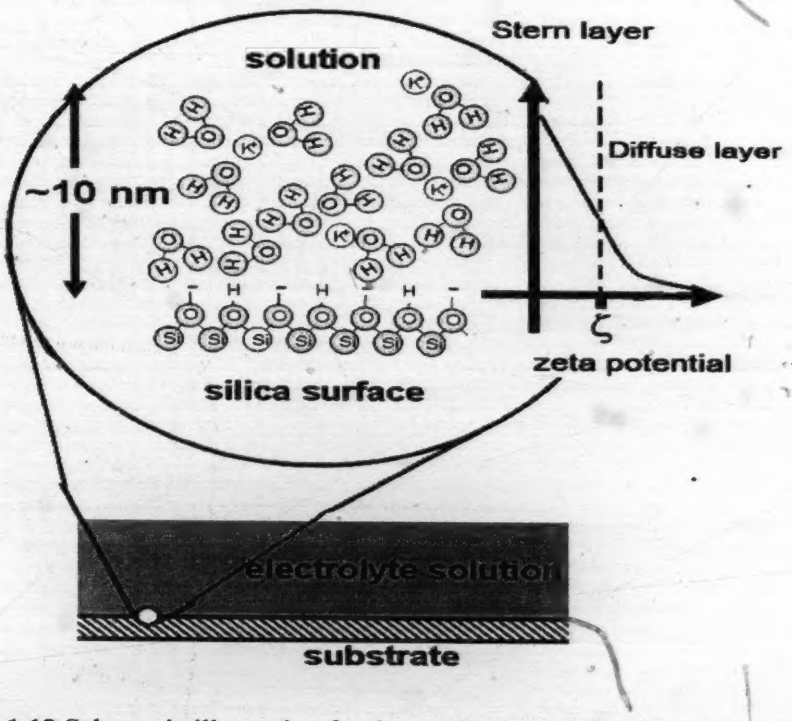

Figure 1.12 Schematic illustration for the mechanism of the electroosmotic flow within silica surface channel.

EOF is an essential phenomenon in capillary electrophoresis, which refers to the movement of liquid relative to a stationary charged surface under an applied electric field [90]. A silica or glass surface has ionizable silanol groups (Si-O$^-$) in contact with the buffer solution at pH greater than 3, as shown in Figure 1.12. Thus, the inner surface of

the channel is negatively charged, leading to the build-up of surface electric charge and a diffuse field of counter ions in an electrical double layer [91]. The first fixed layer of ions is the Stern layer, and the outer mobile layer is the Diffuse layer. There is a plane of slip that separates the mobile fluid from fluid that remains attached to the surface, and the electric potential at this plane is called the zeta potential. The plane of slip position depends on the charge density at the surface and the thickness of the double layer, and is conventionally taken to lie at the inner edge of the Diffuse layer. In the Diffuse layer, the potential falls essentially exponentially to zero [92], as indicated in Figure 1.12. When an electric field is applied, the mobile cation layer is pulled in the direction of cathode. Since these cations are solvated, the solvent migrates with the mobile layer and induces electroosmotic flow (EOF) of the buffer solution. The mobility of EOF is defined as Equation 1.2 [93]

$$\mu_e = \varepsilon \varepsilon_0 \zeta / \eta \qquad \textbf{(1.2)}$$

where ε is the dielectric constant of the dispersion medium, ε_0 is the permittivity of free space, η is the dynamic viscosity of the dispersion medium, and ζ is the zeta potential.

Typically, EOF pumps the buffer flow through the capillary towards the cathode, because most surfaces are anionic under many conditions. Negatively charged analytes are attracted to the anode, counter to the EOF, while positively charged analytes are attracted to the cathode, along with the EOF. Since the EOF is generally greater than the mobility of the analytes, all analytes are carried along with the buffer solution toward the cathode, as illustrated by Figure 1.13. Negatively charged analytes migrate slower in the capillary due to their conflicting electrophoretic and electroosmotic mobilities. Neutral components migrate with the same velocity as the EOF.

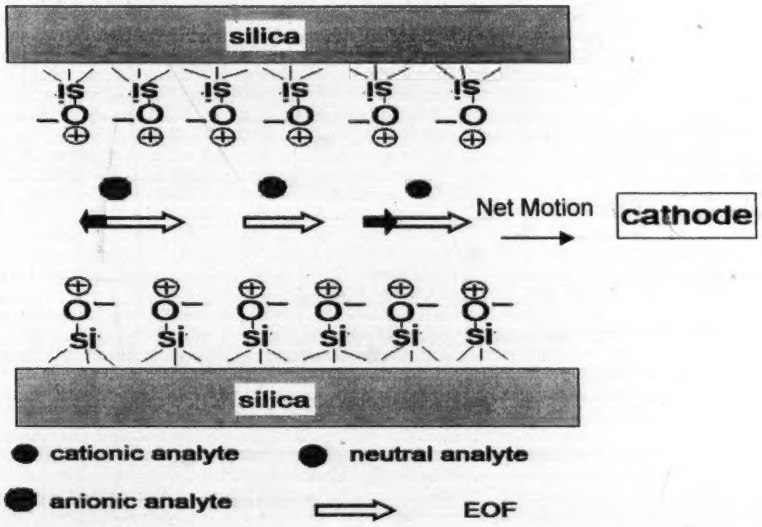

Figure 1.13 Schematic illustration of the mechanism of the capillary electrophoresis separation.

1.3.2 Capillary Electrochromatography

In order to improve the selectivity and efficiency of protein separation, capillary electrophoresis systems can be adapted for capillary electrochromatography by combining electrokinetic pumping with liquid chromatography based separation mechanisms. Therefore, CEC separation is based on the differences of partition coefficients of solutes between two phases combined with the differences of solutes mobilities [94]. CEC may provide better selectivity in some cases, for example, in protein separations [95]. Much of the research in CEC has involved the use of capillaries packed with particles, typically silica-based chromatographic beads inherited from HPLC. The Remcho group did early work on investigating the EOF behavior during the particle packed CEC separation to elucidate separation mechanism [96-98]. Figure 1.14 shows the different flow profile properties of pressure driven and EOF driven flow in a packed column. For EOF driven flow, the flow rate is independent of particle diameter and

column length. Therefore, smaller particles and longer columns can be used for separation, which will provide higher efficiency, compared to the pressure driven flow. EOF reduces dispersion of the solute band as it passes through the column due to the plug -like character of electroosmotic flow, which improves the efficiency and peak capacity [99, 100].

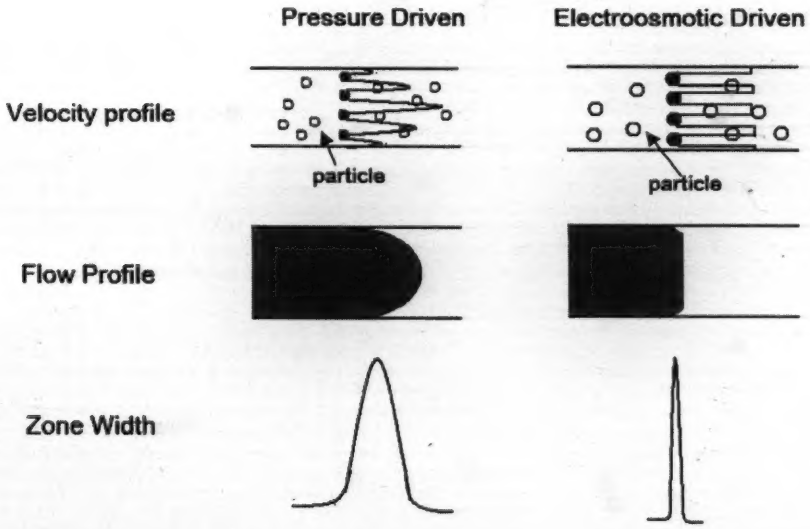

Figure 1.14 The difference between the profiles of flow driven by pressure and EOF in a packed column. Adapted from ref [101].

1.3.3 Separation Efficiency and Resolution

The separation efficiency of capillary zone electrophoresis can be characterized using the number of theoretical plates, which in the idealized case is given by:

$$N = \mu V / D_m \qquad (1.3)$$

where N is the number of theoretical plates, μ is the apparent mobility in the separation medium and D_m is the diffusion coefficient of the analyte. According to this equation, the

separation efficiency is largely affected by diffusion and is proportional to the strength of the electric field. EOF does not significantly contribute to band broadening as in pressure-driven chromatography, due to its plug-like character. Assuming the signal peaks fit a Gaussian distribution, the theoretical plate number can be determined from the electropherogram by using the following equation:

$$N = 5.54 (t_R / W_h)^2 \quad (1.4)$$

where t_R is migration time, $W_{1/2}$ is peak width at half height. In practice, the measured efficiency also includes peak broadening effects arising from injection, detection, electric dispersion, Joule heating and adsorption of samples to the wall [102]. Resolution, R_s, measures how well species have been separated. The resolution of two adjacent peaks can be defined as the ratio of the peak separation Δt to the average baseline width of two adjacent peaks: $R_s = 2\Delta t / (W_1 + W_2)$. Baseline resolution is achieved when $R_s = 1.5$.

1.3.4 Microchip Electrophoresis and Electrochromatography

Since the early 1990s, when Manz and Harrison micromachined a miniaturized capillary electrophoresis-based system on chip [103-106], microchips for analytical separation purposes have attracted great attention [107-110]. The prevalence of electrokinetic separation in microdevices is due to the ease of implementation, the potential for automation, and the ability to generate EOF inside microchip channels to provide pumping actions.

Figure 1.15 shows the typical microchip electrophoresis setup, in which the microchip consists of two perpendicular channels connecting four reservoirs. Typical channel dimensions are around 50-200 μm wide and 5-150 μm deep. The shorter channel

is generally used for sample injection, and the longer one is used as the separation channel. The volumes of the reservoirs are typically around 10-50 μL, and they allow the loading of buffer and samples, and collecting of the waste. Injection is generally achieved by an electrokinetic mode, after complete filling of the channel with the buffer.

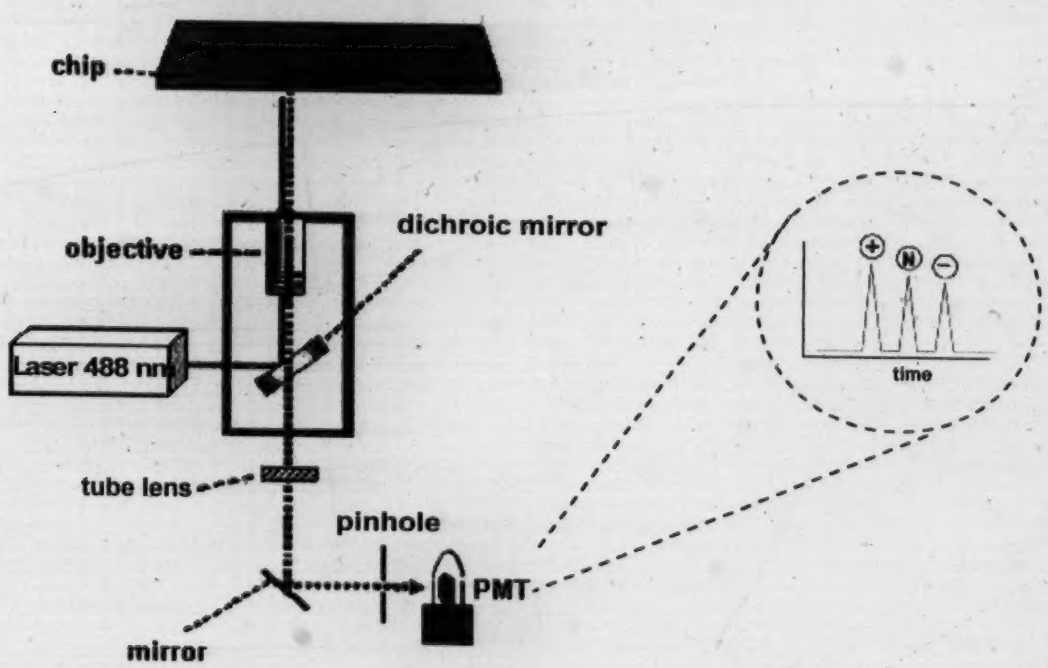

Figure 1.15 The schematic setup for microchip electrophoresis coupled with laser induced fluorescence detection (LIF).

The sample is first placed into the sample reservoir. Then, a suitable voltage is applied between the sample load reservoir and sample waste reservoir. The electrophoretic mobility of the analyte, often combined with EOF, leads to displacement of the sample across the intersection of the two channels. Surface treatment may reduce the EOF, so that electrokinetic sampling performed in these cases does not depend on

EOF. The electric potential is then switched from the sample channel to the separation channel, in order to inject and to separate the analytes electrokinetically. For detection, laser induced fluorescence detection (LIF) is easily adapted to the dimensions of microchips. A variety of excitation sources are now commercially available, and a 488 - nm Ar laser is a common choice. Fluorescent emission from the analytes was collected by an inverted microscope equipped with a dichroic mirror and filter. Eventually, the signal is collected by a PMT detector.

Microchip-based electrochromatography is a hybrid method of microchip zone electrophoresis and chip-based liquid chromatography and it combines the best characteristics of both methods [111]. Combining those two methods creates a powerful analytical tool capable to separate both ionic and neutral compounds with high efficiency and selectivity. Additionally, flow generated by electroosmosis obviates the need for high pressure pumps, which are difficult to fabricate in the microchip manifold. Many packing materials have been incorporated into the microchannel for CEC separation, including sol-gel and polymer-based monoliths and beads [112-114].

In open-channel electrochromatography the walls of a microchannel are coated with a retentive phase. Different distribution equilibria between the running buffer and a coated stationary phase are responsible for resolution of the solutes. The octadecyl and octyl reverse-phase (C_{18} and C_8) coatings are popular in microchip-based open–channel electrochromatography [115-117]. The first instance was described by the Ramsey group [118, 119]. A glass microchip with serpentine column geometry and chemically bonded octadecyl group on the microchannel walls was prepared. Three neutral coumarin dyes were baseline separated in 170 s with 5-μm plate height. Pumera *et al.* described a gold

nanoparticle coated open-channel electrochromatography [120]. 10-nm citrate-stabilized gold nanoparticles were used and the resolution and plate numbers were doubled in the presence of gold nanoparticles compared to untreated channel.

In the following chapters, we will focus on the effects of important parameters suggested in the theories introduced above, including the selection of porogenic solvents and monomers for polymer porous structure formation, photopatterning resolution, EOF, glass channel coating and protein separation, etc. The knowledge gained through these efforts will help us to optimize polymer monolith integration within the microfluidic devices and explore their applications.

1.4 REFERENCES

1 Whitesides, G. M. *Nature* **2006**, *442*, 368-373.

2 Ali, J. E.; Sorger, P. K.; Jensen, K. F. *Nature* **2006**, *442*, 403-411.

3 Craighead, H. *Nature* **2006**, *442*, 387-393.

4 Janasek, D.; Franzke, J.; Manz, A. *Nature* **2006**, *442*, 374-380.

5 DeMello, A. J. *Nature* **2006**, *442*, 394-402.

6 Jung, B.; Bharadwaj, R.; Santiago, J. G. *Electrophoresis* **2003**, *24*, 3476-3483.

7 Obreja, P.; Cristea, D.; Kusko, M.; DinescuJ, A. *Opt. A: Pure Appl. Opt.* **2008**, *10*, 1-6.

8 Liu, Y.; Cady, N. C.; Batt, C. A. *Biomed. Microdevices* **2007**, *9*, 769–776.

9 Fogarty, B. A.; Heppert, K. E.; Cory, T. J.; Hulbutta, K.R.; Martind, R. S.; Lunte, S. M. *Analyst* **2005**, *130*, 924–930.

10 Qi, L. Y.; Yin, X. F.; Zhang, L.; Wang, M. *Lab Chip* **2008**, *8*, 1137–1144.

11 Kumar, K. S.; Kang, S. H. *Electrophoresis* **2007**, *28*, 4247–4254.

12 Duffy, C. F.; MacCraith, B.; Diamond, D.; O'Kennedy, R.; Arriaga, E. A. *Lab Chip* **2006**, *6*, 1007–1011.

13 Hosokawa, K.; Omata, M.; Maeda, M. *Anal. Chem.* **2007**, *79*, 6000-6004.

14 Chen, P. J.; Rodger, D. C.; Meng, E. M.; Humayun, M. S.; Tai, Y.C. *J. Microelectromech. Syst.* **2007**, *16*, 223-231.

15 Oh, K. W.; Park, C.; Namkoong, K.; Kim, J.; Ock, K. S.; Kim, S.; Kim, Y. A.; Cho, Y. K.; Ko, C. *Lab Chip* **2005**, *5*, 845–850.

16 Wang, J.; Chen, Z.; Mauk, M.; Hong, K. S.; Li, M.; Yang, S.; Bau, H. H. *Biomed. Microdevices* **2005**, *7*, 313-322.

17 Suzuki, H.; Yoneyama, R. *Sens. Actuators, B* **2003**, *96*, 38–45.

18 Niu, X.; Liu, L.; Wen, W.; Sheng, P. *Appl. Phys. Lett.* **2006**, *88*, 153508-153510.

19 Burke, B. J.; Regnier, F. E. *Anal. Chem.* **2003**, *75*, 1786-1791.

20 Harnett, C. K.; Templeton, J.; Dunphy-Guzman, K. A.; Senousy, Y. M.; Kanouff, M. P. *Lab Chip* **2008**, *8*, 565–572.

21 Liu, M. C.; Ho, D.; Tai, Y. C. *Sens. Actuators, B* **2008**, *129*, 826–833.

22 Yairi, M.; Richter, C. *Sens. Actuators, A* **2007**, *137*, 350-356.

23 Eddings, M. A.; Gale, B. K. *J. Micromech. Microeng.* **2006**, *16*, 2396–2402.

24 Yu, H.; Balogun, O.; Li, B.; Murray, T. W.; Zhang, X. *Sens. Actuators, A* **2006**, *127*, 228–234.

25 Huang B.; Wu H.; Bhaya D.; Grossman A.; Granier S.; Kobilka B. K.; Zare R. N. *Science* **2007**, 315, 81-84.

26 Fu, J. P.; Yoo, J.; Han, J. Y. *Phys. Rev. Lett.* **2006**, *97*, 018103-1-4.

27 Squires, T. M.; Quake, S. R. *Rev. Mod. Phys.* **2005**, *77*, 977-1026.

28 Dertinger, S. K. W.; Chiu, D. T.; Jeon, N. L.; Whitesides, G. M. *Anal. Chem.* **2001**, *73*, 1240-1246.

29 Kamholz, A. E.; Yager, P. *Biophys. J.* **2001**, *80*, 155–160.

30 Shchukin, D. G.; Kommireddy, D. S.; Zhao, Y.; Cui, T.; Sukhorukov, G. B.; Lvóv, Y. M. *Adv. Mater.* **2004**, *16*, 389-393.

31 Hansen, C. L.; Skordalakes, E.; Berger, J. M.; Quake, S. R. *Proc. Natl. Acad. Sci. U.S.A.* **2002**, *99*, 16531–16536.

32 Zheng, B.; Tice, J. D.; Roach, L. S.; Ismagilov. R. F. *Angew. Chem. Int. Ed.* **2004**, *43*, 2508 –2511.

33 Nisisako, T.; Torii, T. *Lab Chip* **2008**, 8, 287-293.

34 Thorsen, T.; Maerkl, S. J.; Quake, S. R. *Science* **2002**, *298*, 580-584.

35 Melin, J.; Quake, S. R. *Annu. Rev. Biophys. Biomol. Struct.* **2007**, *36*, 213–231.

36 Wikswo, J. P.; Prokop, A.; Baudenbacher, F.; Cliffel. D.; Csukas, B.; Velkovsky, M. *IEF Proc.-Nanobiotechnol.* **2006**, *153*, 81-101.

37 Herr, A. E.; Hatch, A. V.; Throckmorton, D. J.; Tran, H. M.; Brennan, J. S.; Giannobile, W. V.; Singh, A. K. *Proc. Natl. Acad. Sci. U.S.A.* **2007**, *104*, 5268-5273.

38 Bagolini, A.; Pakula, L.; MScholtes, T. L.; Pham, H. T. M.; French, P. J.; Sarro, P. M. *J. Micromech. Microeng.* **2002**, *12*, 385–389.

39 Harfenist, S. A.; Cambron, S. D.; Nelson, E. W.; Berry, S. M.; Isham, A. W.; Crain, M. M.; Walsh, K. M.; Keynton, R. S.; Cohn, R. W. *Nano Lett.* **2004**, *4*, 1931-1937.

40 He, B.; Tait, N.; Regnier, F. *Anal. Chem.* **1998**, *70*, 3790-3797.

41 Rosqvist, T.; Johansson, S. *Sens. Actuators, A* **2002**, 97-98, 512-519.

42 Wirth, M. J. *Anal. Chem.* **2007**, *79*, 801-808.

43 Zeng, Y.; He, M.; Harrison, D. J. *Angew. Chem. Int. Ed.* **2008**, *47*, 6388-6391.

44 Ng, J. M. K.; Gitlin, I.; Stroock, A. D.; Whitesides, G. M. *Electrophoresis* **2002**, *23*, 3461-3473.

45 Hatch, A. V.; Herr, A. E.; Throckmorton, D. J.; Brennan, J. S.; Singh, A. K. *Anal. Chem.* **2006**, *78*, 4976-4984.

46 Jemere, A. B.; Oleschuk, R. D.; Ouchen, F.; Fajuyigbe, F.; Harrison, D. J. *Electrophoresis* **2002**, *23*, 3537–3544.

47 Oleschuk, R. D.; Shultz-Lockyear, L. L.; Ning, Y.; Harrison, D.J. *Anal. Chem.* **2000**, *72*, 585-590.

48 Masaki, H.; Hoshi, J.; Amano, S.; Sasaki, Y.; Korenaga, T. *Anal. Sci.* **2006**, *22*, 345-348.

49 Gac, S. L.; Carlier, J.; Camart, J. C.; Olivé, C. C.; Rolando, C. *J. Chromatogr. B* **2004**, *808*, 3-14.

50 Logan, T. C.; Clark, D. S.; Stachowiak, T. B.; Svec, F.; Fréchet, J. M. J. *Anal. Chem.* **2007**, *79*, 6592-6598.

51 Rohr, T.; Yu, C.; Davey, M. H.; Svec, F.; Fréchet, J. M. J. *Electrophoresis* **2001**, *22*, 3959-3967.

52 Throckmorton, D. J.; Shepodd, T. J.; Singh, A. K. *Anal. Chem.* **2002**, *74*, 784-789.

53 Wen, J.; Guillo, C.; Ferrance, J. P.; Landers, J. P. *Anal. Chem.* **2007**, *79*, 6135-6142.

54 Wang, Z. *University of Alberta Thesis*, Edmonton, **2007**.

55 Reichmuth, D. S.; Shepodd, T. J.; Kirby, B. J. *Anal. Chem.* **2005**, *77*, 2997-3000.

56 Hasselbrink, E. F.; Jr.; Shepodd, T. J.; Rehm, J. E. *Anal. Chem.* **2002**, *74*, 4913-4918.

57 Taylor, J.; Wang, C.; Harrison, D. J. *Proc. μTAS 2002*, Netherlands, **2002**, 344-346.

58 Taylor, J. *University of Alberta Thesis*, Edmonton, **2004**.

59 Remcho, V. T.; McNair, H. M. *J. High. Resolut. Chromatogr.* **1991**, *14*, 471-474.

60 Remcho, V. T.; McNair, H. M.; Rasmussen, H. T. *J. Chem. Educ.* **1992**, *69*, A117-A119.

61 Svec, F. *Electrophoresis* **2006**, *27*, 947-961.

62 Svec, F. *J. Chromatogr. B* **2006**, *841*, 52-64.

63 Miyabe, K.; Guiochon, G. *J. Sep. Sci.* **2004**, *27*, 853–873.

64 Viklund, C.; Svec, F.; Fréchet, J. M. J. *Chem. Mater.* **1996**, *8*, 744-750.

65 Okay, O. *Prog. Polym. Sci.* **2000**, *25*, 711–779.

66 Sing, K. S. W. *Colloids Surf., A* **2004**, *241*, 3-7.

67 Urban, J.; Eeltink, S.; Jandera, P.; Schoenmakers, P. J. *J. Chromatogr. A* **2008**, 1182, 161-168.

68 Xie, S.; Allington, R. W.; Fréchet, J. M. J.; Svec, F. *Adv. Biochem. Eng./Biotechnol.* **2002**, *76*, 88-125.

69 Yu, C.; Xu, M.; Svec, F.; Fréchet, J. M. J. *J. Polym. Sci., Part A: Polym. Chem.* **2002**, *40*, 755–769.

70 Peters, E. C.; Svec, F.; Fréchet, J. M. J. *Adv. Mater.* **1999**, *11*, 1169-1181.

71 Svec, F.; Fréchet, J. M. J. *Chem. Mater.* **1995**, *7*, 707-715.

72 Buchmeiser, M. R. *Polym.* **2007**, *48*, 2187-2198.

73 Svec, F.; Fréchet, J. M. J. *Ind. Eng. Chem. Res.* **1999**, *38*, 34-48.

74 Viklund, C.; Svec, F.; Fréchet, J. M. J. *Chem. Mater.* **1996**, *8*, 744-750.

75 Shultz, A. R.; Joshi, M. G. *J. Polym. Sci., Part B: Polym. Phys.* **1984**, *22*, 1753-1771.

76 Kelly, J. M.; Mcardle, C. B.; Maunder, M. J. F. *Photochemistry and polymeric systems*, Royal Society of Chemistry, Cambridge, **1998**.

77 Bahadur, P.; Sastry, N. V. *Principles of polymer science*, Narosa Publishing House, New Delhi, **2002**.

78 Ahluwaliu, V. K.; Mishra, A. *Polymer science: A text book*, CRC Press, Florida, **2008**.

79 Dyer, D. J. *Adv. Polym. Sci.* **2006**, *197*, 47–65.

80 Stachowiak, T. B.; Svec, F.; Fréchet, J. M. J. *Chem. Mater.* **2006**, *18*, 5950-5957.

81 Pucci, V.; Raggi, M. A.; Svec, F.; Fréchet, J. M. J. *J. Sep. Sci.* **2004**, *27*, 779-788.

82 Eeltink, S.; Hilder, E. F.; Geiser, L.; Svec, F.; Fréchet, J. M. J.; Rozing, G. P.; Schoenmakers, P. J.; Kok, W. T. *J. Sep. Sci.* **2007**, *30*, 407-413.

83 Zhu, G.; Yuan, H.; Zhao, P.; Zhang, L.; Liang, Z.; Zhang, W.; Zhang, Y. *Electrophoresis* **2006**, *27*, 3578-3585.

84 Sommer, G. J.; Singh, A. K.; Hatch, A. V. *Anal. Chem.* **2008**, *80*, A-G.

85 Stachowiak, T. B.; Mair, D. A.; Holden, T. G.; Lee, L. J.; Svec, F.; Fréchet, J. M. J. *J. Sep. Sci.* **2007**, *30*, 1088-1093.

86 Ranby, B.; Yang, W. T.; Tretinnikov, O. *Nucl. Instrum. Methods Phys. Res., Sect. B* **1999**, *151*, 301-305.

87 Gao, S. L.; Häβler, R. H.; Mäder, E.; Bahners, T.; Opwis, K.; Schollmeyer, E. *Appl. Phys. B* **2005**, *81*, 681–690.

88 Rohr, T.; Hilder, E. F.; Donovan, J. J.; Svec, F.; Fréchet, J. M. J. *Macromol.* **2003**, *36*, 1677-1684.

89 Deyl, Z. *Electrophoresis part A: techniques*, Elsevier, Netherlands, **1979**.

90 Wang, W.; Zhou, F.; Zhao, L.; Zhang, J. R.; Zhu, J. J. *J. Chromatogr. A* **2007**, *1170*, 1–8.

91 Attard, P. *Curr. Opin. Colloid Interface Sci.* **2001**, *6*, 366-371.

92 Schmickler, W. *Chem. Rev.* **1996**, *96*, 3177-3200.

93 Kirby, B. J.; Hasselbrink, E. F.; Jr. *Electrophoresis* **2004**, *25*, 187–202.

94 Clark, S. L.; Remcho, V. T. *Anal. Chem.* **2003**, *75*, 5692-5696.

95 Cooper, J. W.; Wang, Y.; Lee, C. S. *Electrophoresis* **2004**, *25*, 3913-3926.

96 Vallano, P. T.; Remcho, V. T. *Anal. Chem.* **2000**, *72*, 4255-4265.

97 Li, D.; Remcho, V. T. *J. Microcol. Separations* **1997**, *9*, 389-397.

98 Vallano, P. T.; Remcho, V. T. *J. AOAC Int.* **1999**, *82*, 1604-1612.

99 Nischang, I.; Tallarek, U. *Electrophoresis* **2007**, *28*, 611–626.

100 Rathore, A. S. *Electrophoresis* **2002**, *23*, 3827–3846.

101 Dittmann, M. M.; Rozing, G. P. *J. Chromatogr. A* **1996**, *744*, 63-74.

102 Righetti, P. G.; Vanoss, C. J.; Wanderhoff, J. W. *Electrokinetic separation methods*, Elsevier, Netherlands, **1979**.

103 Manz, A; Fettinger, J. C.; Verpoorte, E. M. J.; Ludi, H.; Widmer, H. M.; Harrison, D. J. *Trends Anal. Chem.* **1991**, *10*, 144-149.

104 Manz, A.; Harrison, D. J.; Verpoorte, E. M.J.; Fettinger, H. C.; Ludi, H.; Widmer, H. M. *J. Chromatog.* **1991**, *593*, 253-258.

105 Harrison, D. J.; Manz, A.; Fan, Z.; Ludi, H.; Widmer, H. M. *Anal. Chem.* **1992**, *64*, 1926- 1932.

106 Harrison, D.J.; Fluri, K.; Seiler, K.; Fan, Z.; Effenhauser, C. S.; Manz, A. *Science* **1993**, *261*, 895-897.

107 Peng, Y.; Pallandre, A.; Tran, N. T.; Taverna, M. *Electrophoresis* **2008**, *29*, 157-178.

108 Pumera, M.; Wang, J.; Grushka, E.; Polsky, R. *Anal. Chem.* **2001**, *73*, 5625-5628.

109 Revermann, T.; Götz, S.; Kűnnemeyer, J.; Karst, U. *Analyst* **2008**, *133*, 167-174.

110 Sinville, R.; Soper, S. A. *J. Sep. Sci.* **2007**, *30*, 1714-1728.

111 Pumera, M. *Talanta* **2005**, *66*, 1048-1062.

112 Quigley, C. L.; Marlin, N. D.; Melin, V.; Manz, A.; Smith, N. W. *Electrophoresis* **2003**, *24*, 917-944.

113 Hoegger, D.; Freitag, R. *Electrophoresis* **2003**, *24*, 2058-2972.

114 Lazar, L. M.; Li, L.; Yang, Y.; Karger, B. L. *Electrophoresis* **2003**, *24*, 3655-3662.

115 Constantin, S.; Freitag, R.; Solignac, D.; Sayah, A.; Gijs, M. A. M. *Sens. Actuators B* **2001**, *78*, 267-272.

116 Kutter, J. P.; Jacobson, S. C.; Matsubara, N.; Ramsey, J. M. *Anal. Chem.* **1998**, *70*, 3291-3297.

117 Gottschlich, N.; Jacobson, S. C.; Culbertson, C. T.; Ramsey, J. M. *Anal. Chem.* **2001**, *73*, 2669-2674.

118 Jacobson, S. C.; Hergenriider, R.; Koutny, L. B.; Ramsey, J. M. *Anal. Chem.* **1994**, *66*, 2369-2373.

119 Broyles, B. S.; Jacobson, S. C.; Ramsey, J. M. *Anal. Chem.* **2003**, *75*, 2761-2767.

120 Pumera, M.; Wang, J.; Grushka, E.; Polsky, R. *Anal. Chem.* **2001**, *73*, 5625-5628.

Chapter 2

Characterization of Flow Properties of Porous Monoliths Photopatterned within Microfluidic Channels*

2.1 INTRODUCTION

Automated, high-throughput genomic and proteomic analysis calls for multiplexed, parallel and multichannel microfluidic systems. Reaction and separation beds for protein digestion, solid phase extraction (SPE) and liquid chromatography (LC) will be important components of such systems [1-4]. Such beds can be prepared by packing conventional beads [5, 6], coating channel walls [7], or creating monolithic columns [8-10]. We fabricated 40 packed beds for protein digestion and SPE in 20 parallel channels, meant to feed into a mass spectrometer [11]. However, it is still technically challenging to pack all 40 beds with conventional beads and manage to obtain the same flow properties.

Polymer monolithic columns provide a useful alternative for bed preparation in a highly multiplexed device [12-14]. Their physical and chemical properties can be readily tuned by adjusting the polymerization mixture composition. Additionally, their bicontinuous porous structures cause lower pressure drop along the bed even with smaller pore size compared to silica bead packing. The most important feature of polymer

---

* A portion of this chapter was presented as He, M.; Harrison, D. J. *Proceedings of Micro-Total Analysis Systems.* **2006**, Volume 1, 170-172.

A version of this chapter has been prepared for submission. He, M.; Harrison, D. J. *Electrophoresis.* **2008**.

monoliths for integrated multifunctional microsystems is the relatively simple preparation afforded by *in situ* photopatterning. These features made monolithic columns integrated in microchip devices attractive for chemical and biological analysis [15-17]. Multiplexed, parallel column-based devices require a very high level of reproducibility over time, between the same columns on chip and between chips [18]. To date detailed studies on stability and reproducibility of the fluidic properties of multiplexed monolithic columns within microchannels have not been performed with the level of precision. Here we report in detail on the effects of preparation conditions and extent of column use on the flow properties of monolithic beds, and report bed to bed reproducibility, which is critical to the use of these materials in parallel arrays.

A photobleaching, time of flight linear flow rate measurement method we developed previously [19] was used to study the fluidic properties of porous polymer monoliths in microfluidic channels. Compared to mercury intrusion porosimetry, which measures the pore size of the bulk-prepared monolith in the dry state [20], this method measurement provides a much more accurate evaluation of the flow resistance of monolithic beds fabricated within microchannels. As we have recently shown, the pore size of a monolith is a functional of the size of capillary in which it is formed, revealing measurements on bulk-prepared monolith suspect [21, 22]. Meanwhile, our tests reveal that many monolith recipes did not necessarily yield a monolith in the microchannel with stable flow resistance over time [23]. Bed to bed variation of non-optimized monoliths was also found in the range of 20-200 % on the same wafer. We systematically investigated a wide range of polymerization conditions in order to establish those that give well-defined photopatterned monolithic beds with stable fluidic properties. The results obtained in this

study provide guidance for patterning robust and uniform polymeric monolithic beds. This information is critical for the application of polymer monolith to multiplexed microfluidic systems, such as parallel microreactor or microseparation arrays.

2.2 MATERIALS AND METHODS

2.2.1 Reagents and Samples

Benzoin, toluene, 1-octanol, 1-heptanol, 1-hexanol, 1-dodecanol, 1-decanol, cyclohexanol, 1,4-butanediol, 2-hydroxyethyl methacrylate (HEMA), ethylene dimethacrylate (EDMA) and 3-(trimethoxysilyl)propyl methacrylate were purchased from Aldrich (Milwaukee, WI, USA). EDMA and HEMA were purified by filtering through basic alumina columns (mesh 650, activity I). Fluorescein disodium salt (Sigma, St. Louis, MO) was used as received. Distilled water was polished with a Milli-Q UV Plus Ultra-Pure Millipore system (Mississauga, Ontario, Canada). All solutions were passed through a 0.22 μm pore size filter (Millipore, Bedford, MA) before using.

2.2.2 Preparation of the Photo-polymerized Monoliths within Microchannels

Microchannels were fabricated in Corning 0211 glass (Corning Glass Works, Parkridge, IL) at the University of Alberta NanoFab Facility, using published procedures [24]. 3-cm long channels were etched 20 μm deep and 600 μm wide. For activation, the microchannels were rinsed sequentially with water, 0.2 M sodium hydroxide, water, 0.2 M HCl, and acetone. Then a solution of 20% (v/v) 3-(trimethoxysilyl)propyl methacrylate in ethanol with 5% acetic acid was pumped through each channel for 1h (0.1 μL/min)

using a syringe pump (PHD2000, Harvard apparatus, USA), followed by rinsing with acetone and drying overnight at 75°C.

Functional monomers, crosslinkers, porogenic solvents, and photoinitiator (benzoin, 1 wt% of monomers) were mixed and purged with nitrogen for 5 min to remove dissolved oxygen prior to introduction into microchannels. Filled microchannels were sealed with tape. A custom printed photomask was used to selectively expose 4-mm long channels to a UV transilluminator, equipped with six 312-nm tubes (15W, model TS-312R, Spectroline, Westbury, NY). Monoliths were then flushed with methanol and water (1:1 v/v) (0.05μL/min) for 5 min to remove unreacted reagents. When not in use, the monolithic beds were stored in water.

2.2.3 Recovery of Glass Chip

A thermal decomposition protocol can be used for complete removal of the polymer material from channels yielding a clean glass chip that can be readily reused [16]. The glass chip was flushed by deionized water and heated in an oven at a rate of 10 °C /min to 550°C, then holding for 2 h. After that, the oven cools down to 20 °C at a rate of 10 °C /min. Then the glass channel was incubated in 0.2 M NaOH overnight to refresh the glass surface.

2.2.4 Characterization of Monoliths in Microchannels

A photobleaching, time of flight linear flow rate measurement method we developed previously [19] was used to study the fluidic properties of porous polymer monoliths in microfluidic channels. Briefly, 200 nM fluorescein aqueous solution was used to measure

the linear velocity of a moving dye front at a given pressure. The dye front was created by photobleaching with an intense, chopped Ar-ion laser beam. Flow rates were measured 1 cm downstream of the beds after they were saturated with fluorescein.

Glass chips were cut by a Dicing Saw (Diamond Touch, Colorado, USA) to expose cross-sections of polymer beds in the microchannels, followed by examination using a Leo 1430 scanning electron microscope (SEM) (Leo, Oberkochen, Germany). Pore size measurement with a Hg intrusion porosimetry (Autopore IV 9500, Micromeritics) was performed on bulk monolith materials polymerized in purged glass vials. Prior to measurement, the bulk polymer materials were extracted in a Soxhlet apparatus with methanol for 12 h, and dried in a vacuum for 12 h.

2.3 RESULTS AND DISCUSSION

2.3.1 Photobleaching, Time of Flight Linear Flow Rate Measurement Method

Column integrations in microfluidic devices, such as separation media for chromatography, flow-through reactors, or supports for solid-phase chemistry, rely on their hydrodynamic properties, which essentially allow liquid to flow through the material at a reasonably low back pressure. This property depends primarily on the porosity of the material. The porosity of polymer monolithic columns is a key element of their performance, and is related to pore size via Darcy's law. Mercury intrusion porosimetry is a popular technique for characterizing the pore size distribution of porous solids. However, this technique is restricted to measurement of the dry state of a bulk-scale prepared monolith [25]. The porous structure of a monolith formed within micro-scale channels or capillaries is not necessarily the same as that formed in an unconfined,

bulk volume [21]. This makes it difficult to get accurate, precise information on the affects of monomer composition and porogenic solvent on porosity in a capillary or channel. Notably, while Viklund et al have shown a reasonable correlation of log pore size to flow resistance in agreement with an extension of the Hagen-Poiseuille law, close inspection of their results shows there is significant scatter in the relationship [26].

We have used a time of flight, photobleaching method to evaluate the linear velocity through a monolithic column. Figure 2.1 plots the linear velocity as a function of the pressure applied to the column, for which the slope is proportional to the flow resistance. Mercury intrusion porosimetry measurements were made on bulk-polymerized material of the same composition. Table 2.1 and Figure 2.2 shows porosimetry measurements gave almost the same characteristic pore sizes for three bulk polymers synthesized with various solvent percentages, yet they exhibited significantly different flow resistance when formed in microchannels. We conclude that our linear velocity method provides a more accurate and suitable tool for investigating the porous property of monolithic beds formed in microfluidic channels.

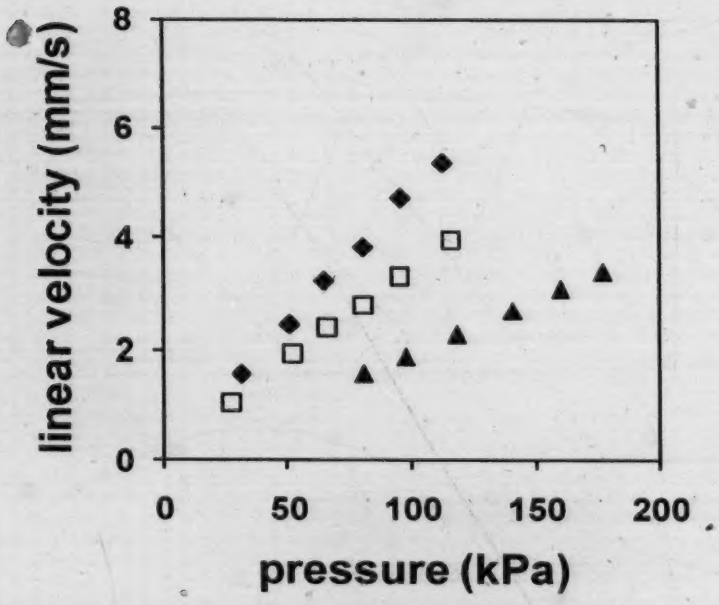

Figure 2.1 The flow resistance of monoliths poly (HEMA-co-EDMA) produced by using different total weight percentages of 1-octanol solvent in a 600-μm wide and 20-μm deep glass channel. ◆ 70% 1-octanol; □ 65% 1-octanol; ▲ 55% 1-octanol. See Table 2.1 for the corresponding pore size measured by Hg intrusion porosimetry.

Table 2.1 Pore sizes of bulk poly (HEMA-co-EDMA) measured by Hg intrusion porosimetry.

Solvent percentage[a] (wt%)	Pore size[b] (μm)	Column length[c] (mm)	Flow resistance (P/V) (10^3 Pa s mm^{-1})
70%	1.05	4.124	20.9
65%	1.06	4.072	28.1
55%	1.04	4.032	51.4

a: The bulk monoliths were formed using different percentages of 1-octanol. b: The values were from two sets of measurements (see Figure 2.2). c: The flow resistance data are shown in Figure 2.1.

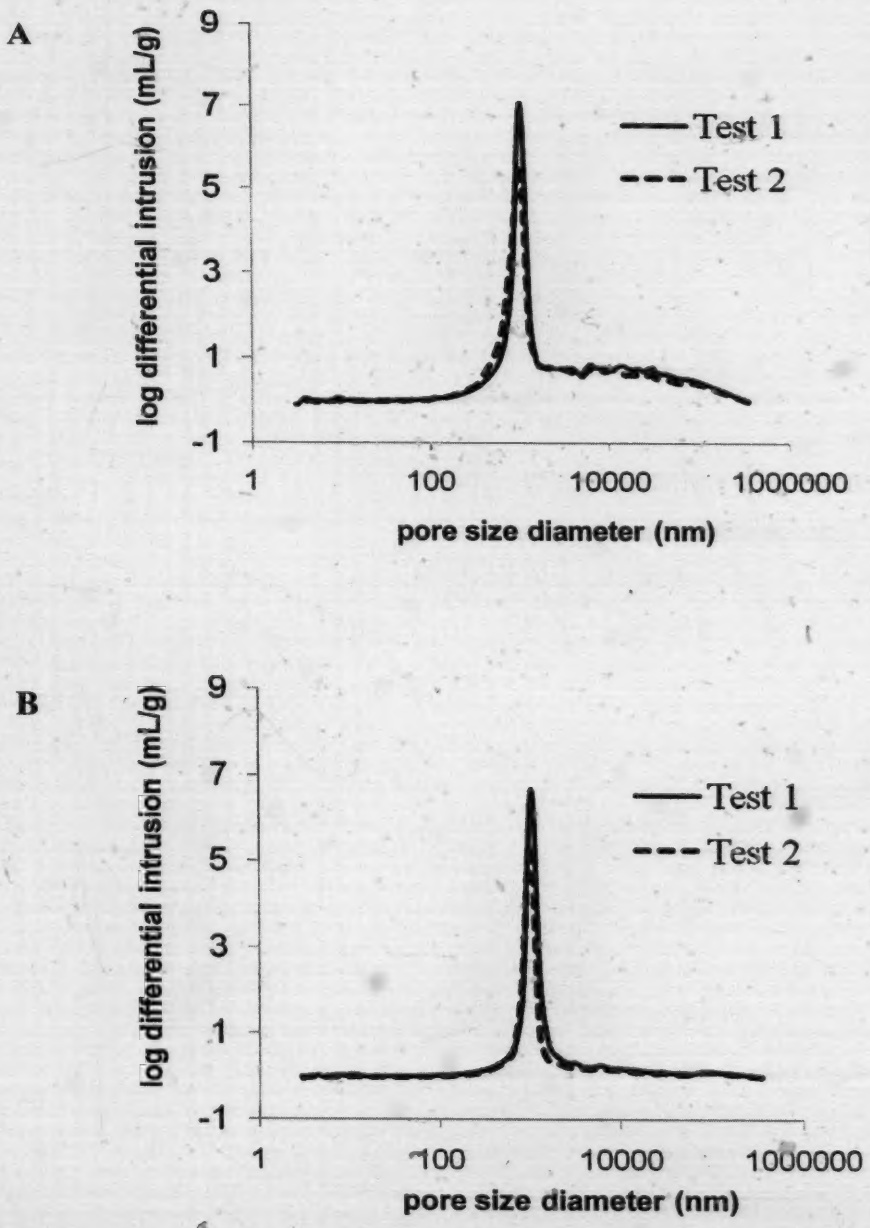

Figure 2.2 Pore size distribution measured by mercury intrusion porosimetry. **A**: 1.05 μm pore size measured twice for the same sample. The recipe was the same as indicated in Figure 2.1, 70% 1-octanol. **B**: 1.04 μm pore size measured from two batches of polymer monoliths. The recipe was the same as indicated in Figure 2.1, 55% 1-octanol.

2.3.2 Porogenic Solvents Selection for Monoliths Localized in Microchannels

Two factors are quite critical in separation column performance within a microchannel; the bed edge must be sharp and well defined in order to reduce band broadening effects, and the porosity should be high enough to allow the use of reasonably low pressures. The choice of pore-forming solvent provides a primary tool for control of the pore size without changing the chemistry of the final monolith [27]. In general, larger pores are obtained in a solvent that is a poor solvent for the monomer and polymer, because of an earlier onset of phase separation [28].

We find that many porogenic solvent/monomer compositions give ill defined edges when photopatterned. It was particularly hard to reproducibly obtain sharp edges using volatile solvents, such as methanol, ethanol and hexane, which are often used to generate large pores [10] (See Chapter 5 for details). In contrast, the use of less volatile solvents greatly improved the quality of photo-patterning within microchannels. The bed quality difference is illustrated in Figure 2.3 A and 2.3 B, comparing a methanol/propanol mixture with 1-octanol as the porogenic solvent, respectively. The difference in behavior may in part be attributed to volatility induced changes in the component ratios in the mixture during preparation and handling. Variations in the solvent ratios of mixed porogenic solvents are known to greatly affect porosity. In addition, viscosity and thermal conductivity differences in the solvents may impact the diffusion and convection of radicals beyond the edge of the photomask.

Figure 2.3 C shows our characterization of the flow resistance of HEMA based polymer monoliths prepared by using different porogenic solvents that give well-defined bed edges in microchannels: including toluene, 1-octanol, 1-heptanol, 1-hexanol, 1-

dodecanol, 1-decanol and cyclohexanol. All the monoliths showed good linear response of flow rate versus applied pressure, in agreement with Darcy's law. That indicates the beds possess good structural stability across the range of pressures applied here. As expected, monoliths prepared using poorer solvents (in the sense they form larger pores) produced higher flow rates, i.e. lower flow resistance. High flow rates can be achieved at low pressure for both Monolith 1 and 2, which have bulk polymer pore sizes larger than 1 μm, whereas the pressure needed to sustain a very modest flow rate is 10 times higher for Monoliths 5, 6 and 7. These results show that toluene and 1-octanol are good candidates for the formation of low back pressure, well defined, HEMA-based monolithic columns within microfluidic devices.

The stability of monolithic structures is very important for their applications in microfluidics, especially in multiplexed microsystems [11]. Monoliths prepared using volatile solvents such as those mentioned above gave significant batch to batch variations in flow resistance (60-200 % depending upon conditions). Even with less volatile solvents not all compositions yielded stable beds. For example, we found the recipe given in reference [23] did not yield a monolith in a microchannel with stable flow resistance over time (the day-to-day variation was 23.2%), as shown in Figure 2.4. Given such variation, it is important to use a sensitive and precise measurement technique such as the time of flight photobleaching apparatus to determine fluid resistance, rather than mercury porosimetry. A wide range of polymerization conditions and monomer /solvent combinations can then be evaluated to determine the compositions that produce robust polymer monoliths within microchannels.

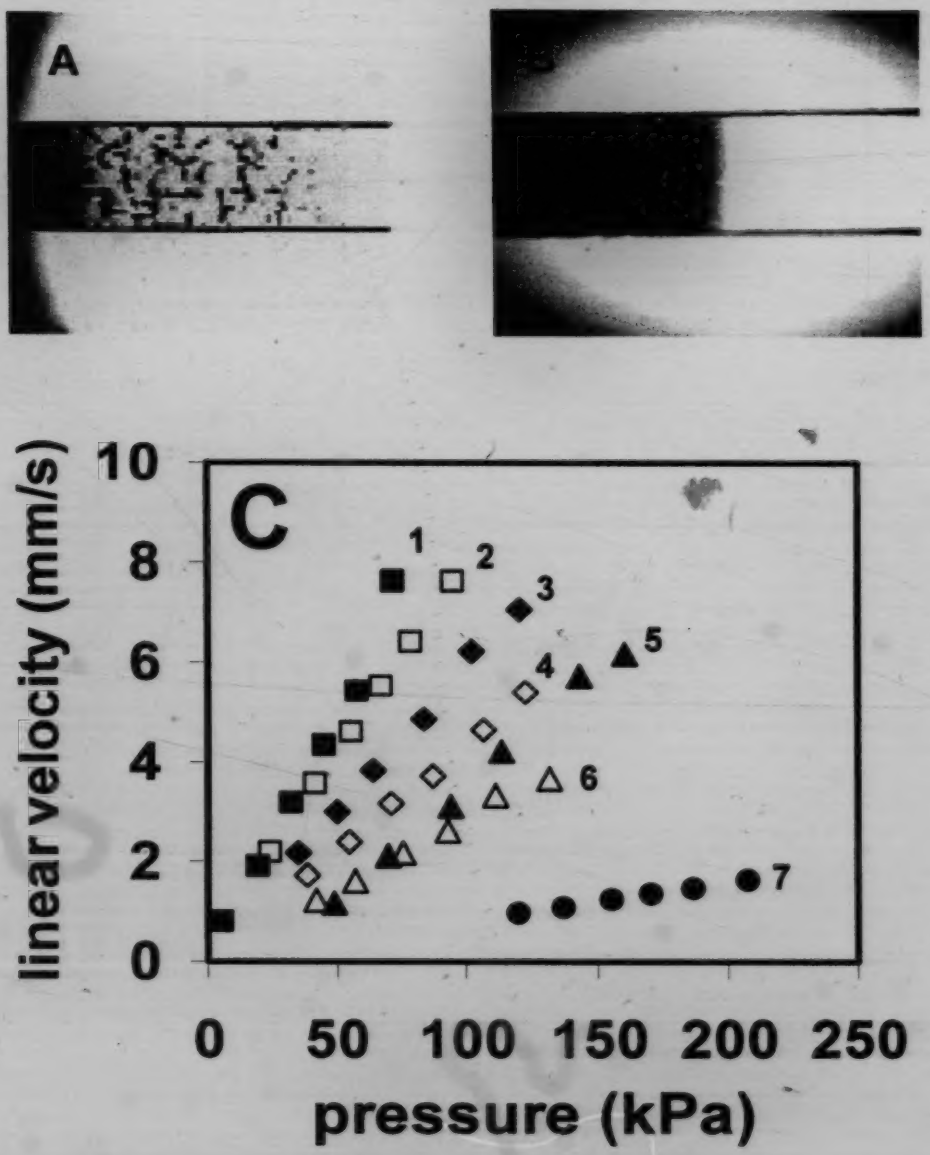

Figure 2.3 A: Diffuse edge of polymer monolith within microchannel produced by volatile porogenic solvents: 30% methanol and 30% 1-propanol. **B**: Sharp edge of monolith produced using 1-octanol. **C**: The flow resistance of monoliths poly (HEMA-co-EDMA) formed using different porogenic solvents. 1: 60% toluene, 2: 65% 1-octanol, 3: 60% 1-heptanol, 4: 60% 1-hexanol, 5: 15% toluene+45%1-dodecanol, 6: 42%1-dodecanol + 18% cyclohexanol, 7: 30%1-decanol+30%1,4-butanediol.

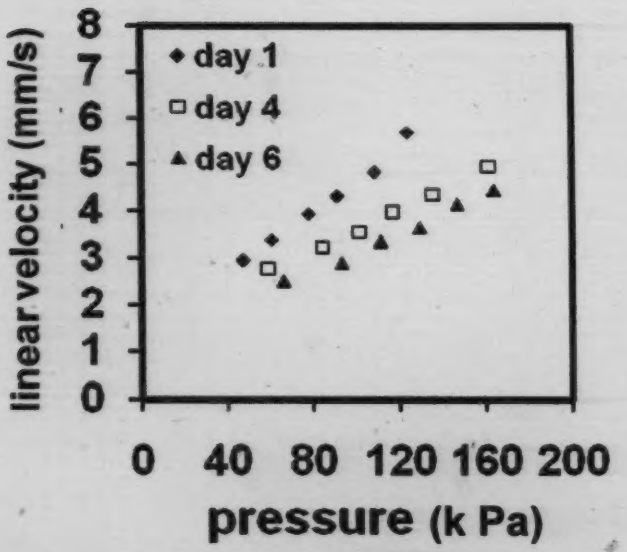

Figure 2.4 The stability of the monolith prepared using the recipe in ref [20]: HEMA 24%, EDMA 16%, 42%1-dodecanol, 18% cyclohexanol. The variation for day-to-day reproducibility is 23.2%.

Table 2.2 Influence of the amounts of monomer HEMA, crosslinker EDMA and porogenic solvent octanol on the monolith structure.

HEMA:EDMA / octanol in total/wt%	20:80	30:70	40:60	50:50	60:40	70:30
80	×	×	×	×	×	×
70	●	●	●	●	○	○
65	●	●	○	○	○	○
60	●	●	●	○	○	○
55	●	●	○	○	○	○
50	∅	∅	∅	∅	∅	∅
40	□	□	□	□	□	□
30	□	□	□	□	□	□

×: easily crushed monolithic structure, ●: structure with stable flow resistance (RSD < 4%),○: structure with unstable flow resistance, ∅: structure with high flow resistance beyond measurement range, □: gel-like impermeable structure.

2.3.3 The Effect of Exposure Time on Structure

The effect of exposure time on the flow resistance of the monolith is presented in Figure 2.5 A, which shows the expected result that higher flow resistance is achieved by longer reaction times. With our photopatterning apparatus the flow rate tends to reach a plateau after 10 min illumination, presumably due to the completion of polymerization. No solid polymer bed was formed within a microchannel before a polymerization time of 5 min, at which point a white solid monolith started to appear. SEM shows that a much denser porous bed was formed after 11 min photoreaction, compared to after a 6 min exposure (Figure 2.5 B and C). No significant change in porous structure was observed for reaction times exceeding 11 min. The morphological changes of the beds over the exposure time are consistent with the trend to increased flow resistance. Monolithic structures formed with 5-7 min exhibited unstable flow resistance over time, appearing to be crushed under the applied pressures. On the other hand, longer exposure times introduce unwanted heat which may deteriorate the bed-edges of the monolith columns. Therefore, 8-9 min was taken as the optimal UV exposure time, and was used for subsequent experiments.

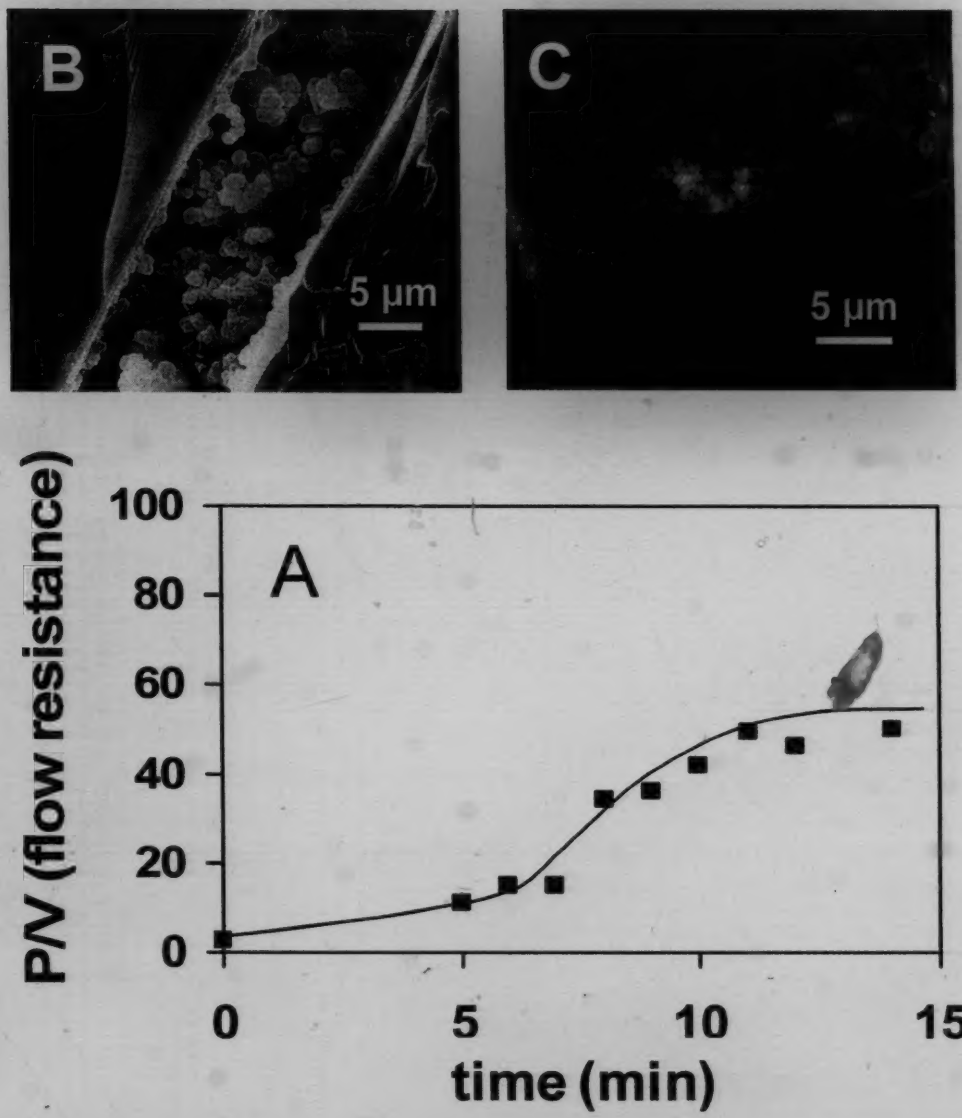

Figure 2.5 The effect of exposure time on the flow resistance (**A**) and porous monolithic structures (**B** 6 min, **C** 11 min). The HEMA based polymer monoliths were prepared from 60 wt% 1-octanol and 40 wt% monomer mixture (EDMA/[HEMA+EDMA]=60 wt%). The solid curve is drawn as a guide to eye.

2.3.4 Fluidic Stability and Reproducibility of Monoliths Photopatterned within Microchannels

The impact of crosslinker to monomer to solvent ratio on the stability and flow resistance of monolithic columns was examined across a fairly large range of compositions. The commonly used HEMA/EDMA mixture was studied as the monomer /crosslinker system. 1-Octanol was selected as the porogenic solvent, because of its good edge-forming characteristics, low volatility, and the relatively low flow resistance of the columns it produced. The porogenic solvent content is a critical parameter for monolith formation. Only monoliths prepared with a solvent content between 55-70 wt% gave desirable and relatively stable flow resistance. Lower solvent content (30-40%) produced gel-like, impermeable monoliths, while 50 wt% solvent resulted in a monolith with a high flow resistance, which is outside the measurement range of our apparatus. Higher (80 wt%) porogen content gave beds that were easily crushed under pressure. The results are summarized in Table 2.2.

Representative flow rate measurement data is presented in Figure 2.6 for various solvent percentages and crosslinker concentrations that gave stable fluidic properties (see below). Higher solvent content at a fixed crosslinker /monomer ratio resulted in a steeper slope of linear velocity plot against the pressure, i.e. a higher permeability of the porous media, as illustrated in Figure 2.6 A. At a fixed porogen wt %, lower flow permeability was obtained for higher crosslinker to monomer ratio, as seen in Figure 2.6 B. This is most likely due to the denser monolith formed with more crosslinker. The linearity observed for all the compositions tested in Figure 2.6 indicates that the patterned monoliths were not compressed or damaged within the pressure range applied (5-60 psi).

The day to day reproducibility of monolithic columns is a very important parameter. Monolithic columns prepared with the recipes listed in Table 2.2 were tested for flow resistance stability over a period of one week. Figure 2.7 and Figure 2.8 showed representative results for monoliths that showed high reproducibility (< 2% RSD) and those that showed low reproducibility (≥ 15 % RSD). Results for all the functioning compositions listed in Table 2.2 are summarized in Figure 2.9, illustrating that a fairly narrow composition range produces highly reproducible flow properties (RSD, n=3-5) over time. The most reproducible results were obtained with 70% crosslinker to monomer content under variety porogenic solvent percentages. The RSD of monoliths with 60%-80% crosslinker to monomer content and 55-70 % 1-octanol was less than 4% over 7 days, which is acceptable in terms of the good reproducibility in fluidic control within microfluidic devices. In contrast, monoliths based on < 60% crosslinker to monomer were relatively unstable over the time. This trend suggests that flow stability is largely controlled by the higher mechanical strength of the monolithic column produced by higher amounts of crosslinker.

The batch to batch variation of monoliths is a highly critical parameter for microfluidic device fabrication, especially in highly parallel device designed with multiple columns on the same device. The variation of a stable composition was evaluated using a recipe of 70 % EDMA to HEMA, and 65 wt% 1-octanol shown in Figure 2.10. Bed to bed variation within one wafer was ± 5.3% (RSD n=3), which is acceptable considering the other variations due to microfabrication (~1%). The results indicates that the bed to bed variation of flow resistance within a single wafer can be sufficiently reproducible for the formation of parallel array within microfluidic devices,

provided the proper formulation is employed. The wafer to wafer variation was 17.9% shown in Figure 2.11, which was less satisfactory. It could be due to the large variation of the channel dimension caused by fabrication among wafer to wafer. However, wafer to wafer variability is less important than bed to bed variation for multiplexed devices.

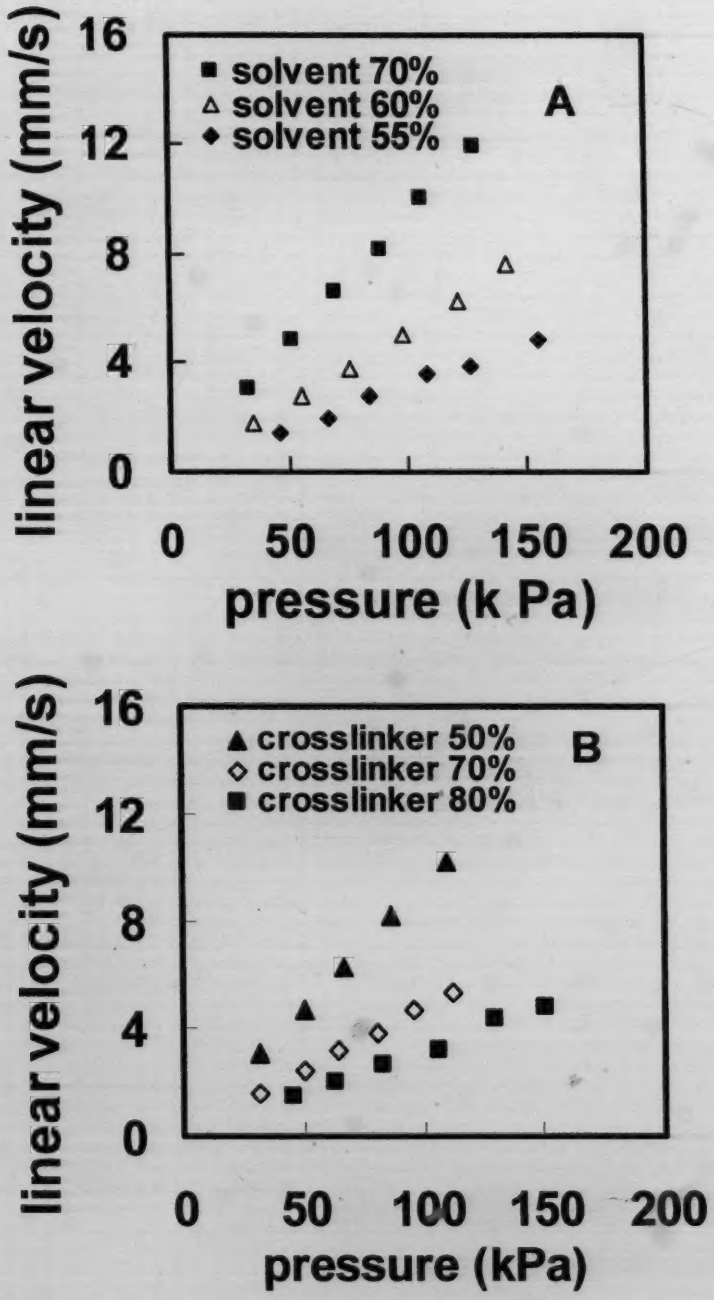

Figure 2.6 Flow properties of different beds formed by using different amounts of porogenic solvent 1-octanol (EDMA/(HEMA+EDMA) fixed at 70 wt% ratio) (**A**) and different ratio of crosslinker EDMA/(HEMA+EDMA) (solvent fixed at 70 wt% 1-octanol)(**B**).

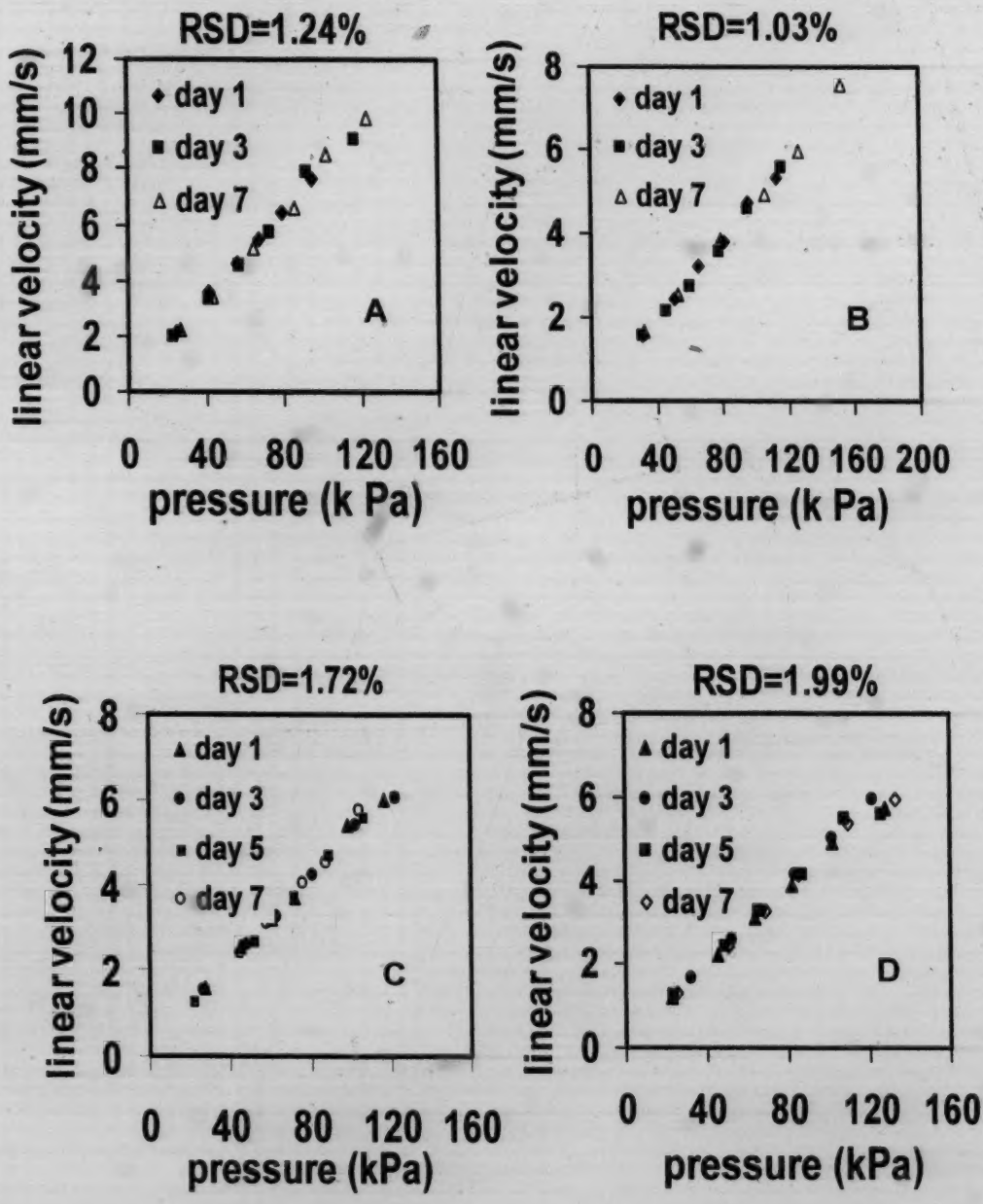

Figure 2.7 The flow stability of the monolithic beds over 7 days for different composition ratios. The graphs of A-D represent the stable and reproducible flow resistance for monoliths with the same amount of 70 wt% EDMA/ (HEMA+EDMA) and different amounts of 1-octanol: **A** 70%, **B** 65%, **C** 60%, **D** 55%.

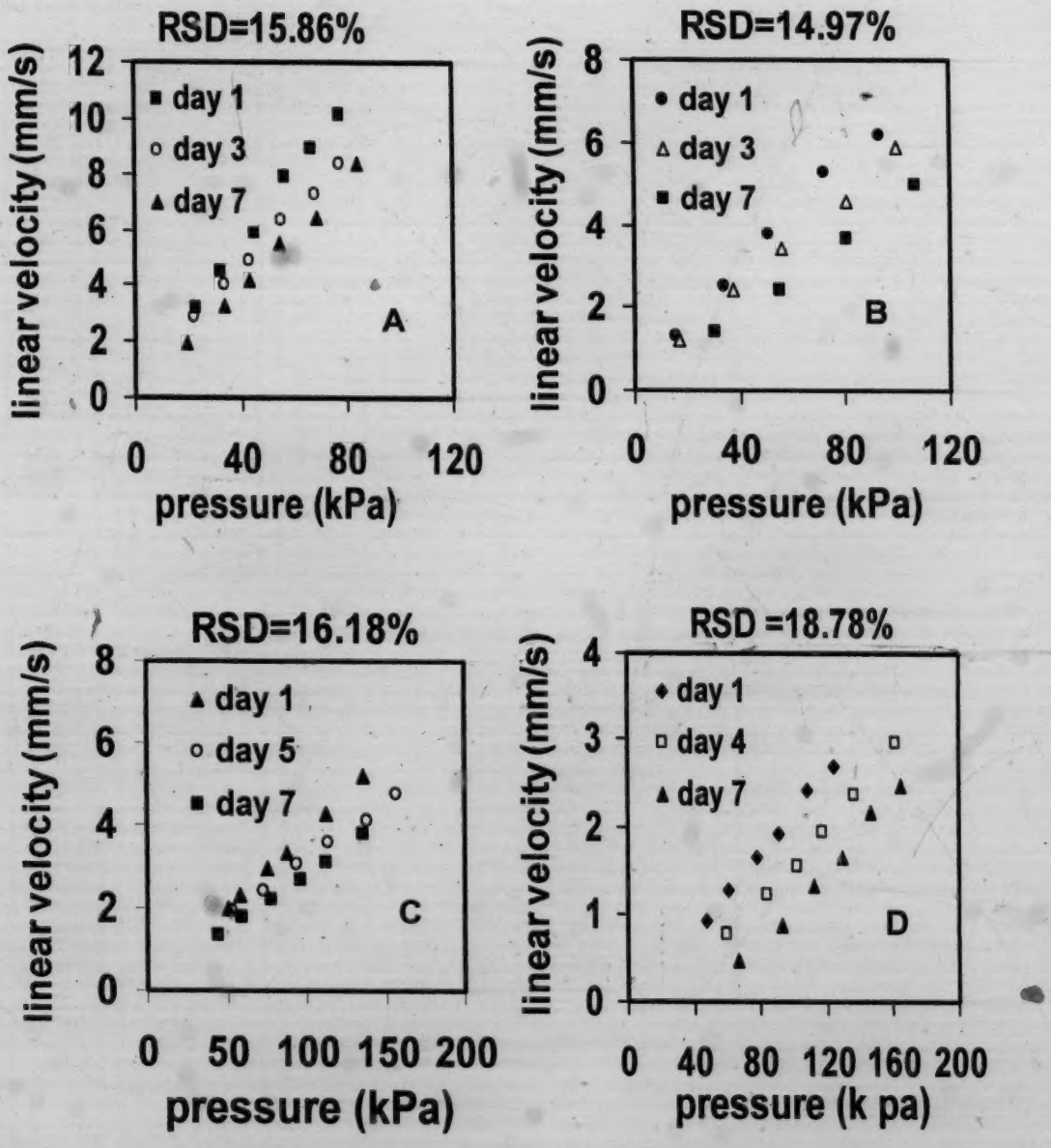

Figure 2.8 The flow stability of the monolithic beds over 7 days for different composition ratios. The graphs of A-D represent the unstable flow resistance for monolith with the same amount of 30 wt% EDMA/ (HEMA+EDMA) and different amounts of 1-octanol: **A** 70%, **B** 65%, **C** 60%, **D** 55%.

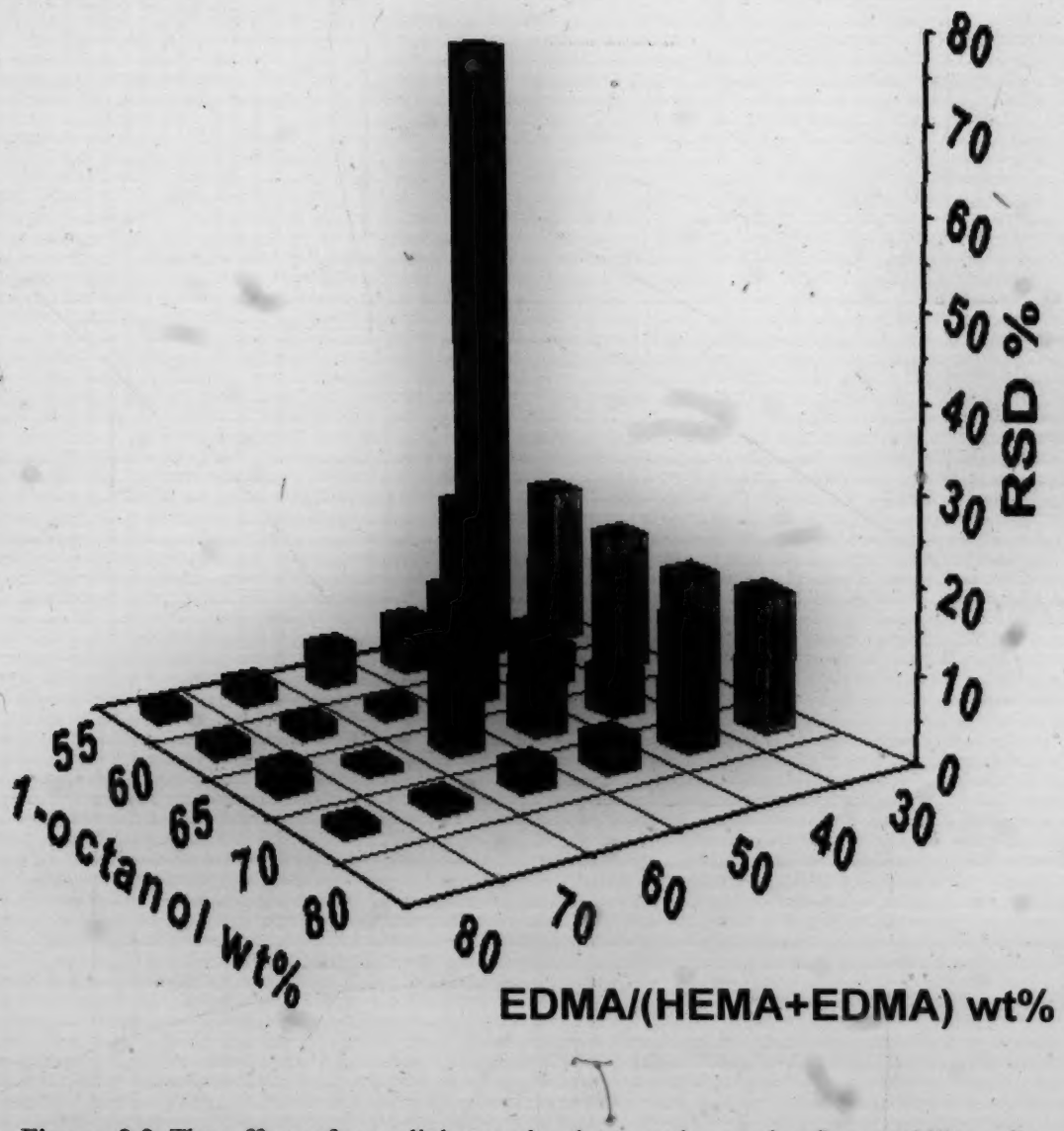

Figure 2.9 The effect of crosslinker and solvent ratio on the flow stability of photopatterned monoliths over 7 days. The RSD was calculated for the slope of the plot of flow rate versus pressure. The pooled RSD shown here is the pooled value measured from two batches of monolithic columns ($n_1+n_2=7$).

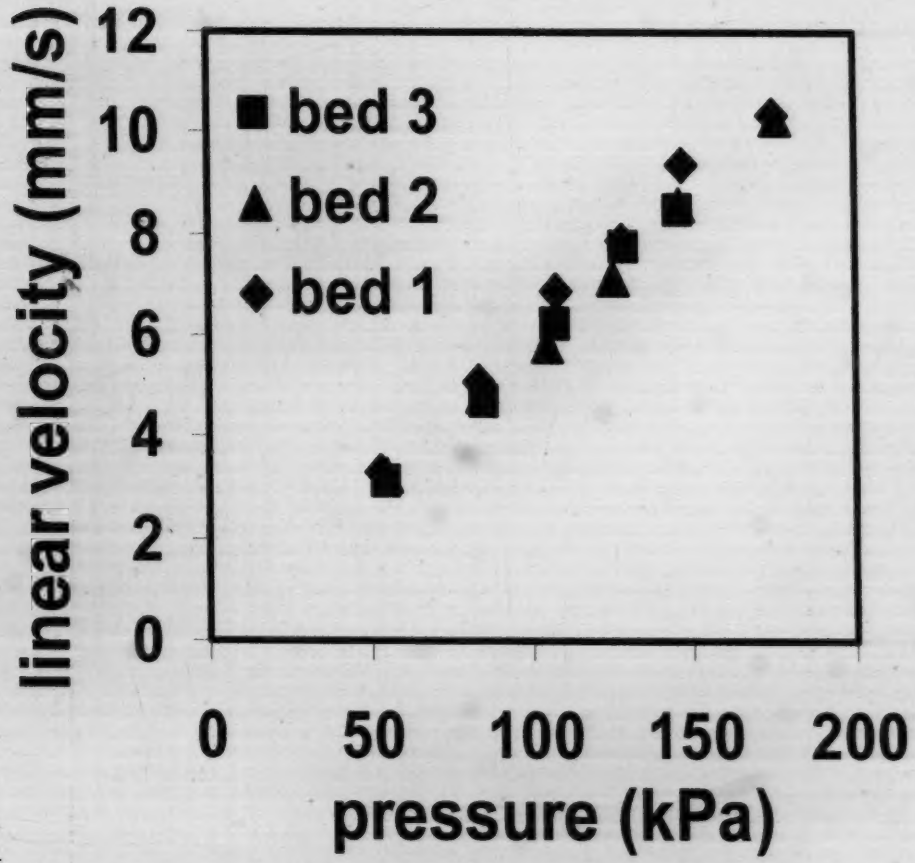

Figure 2.10 Flow measurements for different batches of monolithic beds with the same polymerization conditions on one microfluidic device. The monoliths were prepared with a component ratio within the stable composition range.

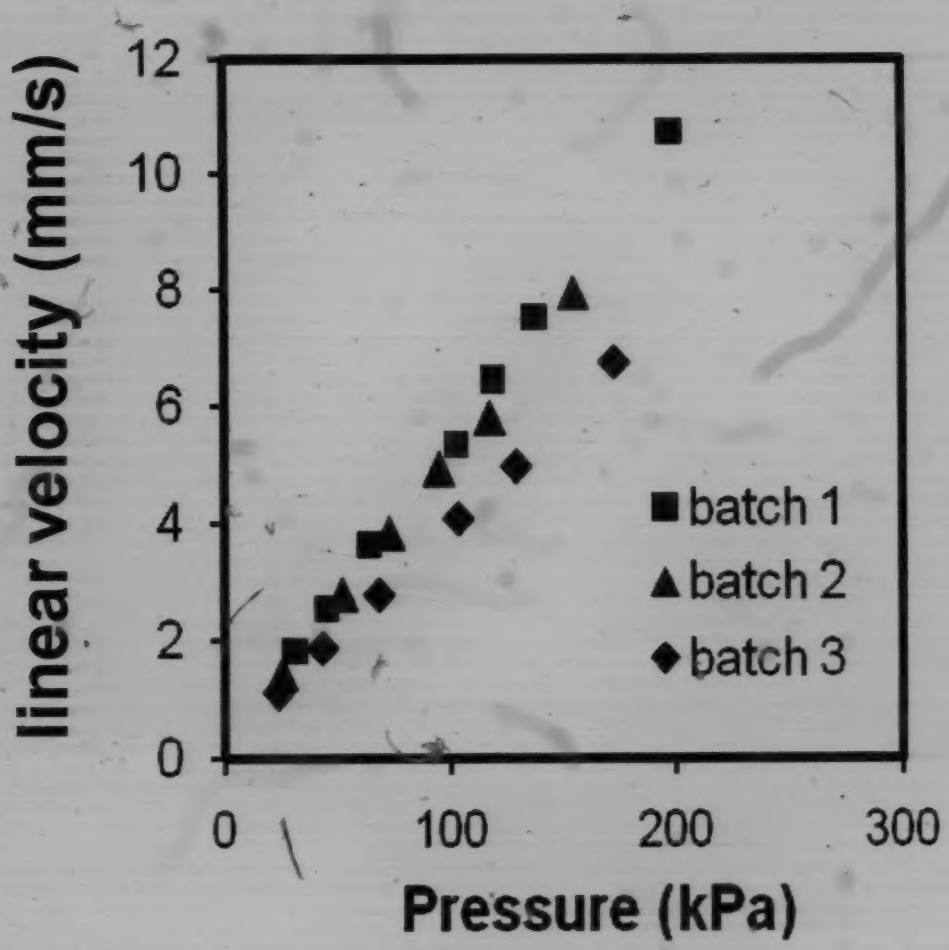

Figure 2.11 Flow properties measured on monolithic beds within different wafers with the same polymerization conditions. The recipe is the same as indicated in Figure 2.10.

2.4 CONCLUSIONS

Reaction and separation columns for protein digestion, solid phase extraction (SPE) and liquid chromatography (LC) are important components, but packing many equivalent columns is very difficult and monolithic columns provide a useful alternative [25]. This paper clearly demonstrates that the preparation of HEMA based monolithic beds within microchannels by photo-initiated polymerization can be made to be highly repeatable, when care is taken to determine the composition range that gives the best stability and reproducibility. Polymerization conditions and recipes based on the stability of flow resistance in microchannels were investigated systematically. Larger amount of solvent result in lower flow resistance, whereas increased crosslinker content results in monoliths with higher flow resistance. A narrow composition range was obtained where good reproducibility and stability are observed, which indicates that the stability was mainly controlled by the amount of crosslinker. Flow resistance evaluation is a much more effective tool for evaluating the flow resistance of monolithic beds than porosimetry, making it a useful tool for designing suitable monolithic materials. These results are critical for designing the integrated multifunctional microfluidic devices with polymerized monoliths.

2.5 REFERENCES

1 Peterson, D. S.; Rohr, T.; Svec, F.; Fréchet, J. M. J. *Anal. Chem.* **2002**, *74*, 4081-4088.

2 Tan, A.; Benetton, S.; Henion, J. D. *Anal. Chem.* **2003**, *75*, 5504-5511.

3 Hedstrom, M.; Grey, C. E.; Gaspar, S.; Mattiasson, B. *J. Chromatogr. A* **2007**, *1146*, 17-22.

4 Duan, J. C.; Sun, L. L.; Liang, Z.; Zhang, J.; Wang, H.; Zhang, L. H.; Zhang, W. B.; Zhang, Y. K. *J. Chromatogr. A* **2006**, *1106*, 165-174.

5 Oleschuk, R.D.; Shultz-Lockyear, L.L.; Ning, Y.; Harrison, D. J. *Anal. Chem.* **2000**, *72*, 585-590.

6 Zeng, Y.; Harrison, D. J. *Anal. Chem.* **2007**, *79*, 2289-2295.

7 Belder, D.; Ludwig, M. *Electrophoresis* **2003**, *24*, 3595-3606.

8 Svec, F. *Electrophoresis* **2008**, *29*, 1593–1603.

9 Wen, J.; Guillo, C.; Ferrance, J. P.; Landers, J.P. *Anal. Chem.* **2007**, *79*, 6135-6142.

10 Reichmuth, D. S.; Shepodd, T. J.; Kirby, B. J. *Anal. Chem.* **2005**, *77*, 2997-3000.

11 Taylor, J.; Wang, C.; Harrison, D. J. *Proc. μTAS 2002*, Netherlands, **2002**, 344-346.

12 James, A.; Brindley, J.; McIntosh, A. C. *Combust. Flame* **2003**, *134*, 193-205.

13 Tan, A.; Benetton, S.; Henion, J. D. *Anal. Chem.* **2003**, *75*, 5504-5511.

14 Yu, C.; Svec, F.; Fréchet, J. M. J. *Electrophoresis* **2000**, *21*, 120-127.

15 Svec, F. *J. Sep. Sci.* **2004**, *27*, 1419-1430.

16 Throckmorton, D. J.; Shepodd, T. J.; Singh, A. K. *Anal. Chem.* **2002**, *74*, 784-789.

17 Gaca, S. L.; Carlierb, J.; Camartb, J. C.; Olivéa, C. C.; Rolando, C. *J. Chromatogr. B* **2004**, *808*, 3-22.

18 Chuda, K.; Jasik, J.; Carlier, J.; Tabourier, P.; Druon, C.; Coaueret, X. *Radiat. Phys. Chem.* **2006**, *75*, 26-33.

19 Bao, J. B.; Harrison, D. J. *AIChE Journal* **2006**, *52*, 75-81.

20 Sing, K. S. W. *Colloids and Surfaces A: Physicochem. Eng. Aspects* **2004**, *241*, 3-7.

21 He, M.; Zeng Y.; Sun, X.; Harrison, D.J. *Electrophoresis* **2008**, *29*, 2980-2986.

22 He, M.; Zeng Y.; Harrison, D.J. *Proc. μ-TAS 2007*, Paris, **2007**, 805-807.

23 Rohr, T.; Yu, C.; Davey, M. H.; Svec, F.; Fréchet, J. M. J. *Electrophoresis* **2001**, *22*, 3959-3967.

24 Cheng, S. B.; Skinner, C.; Taylor, J.; Attiya, S.; Lee, W. E.; Picelli, G.; Harrison, D. J. *Anal. Chem.* **2001**, *73*, 1472-1479.

25 Geiser, L.; Eeltink, S.; Svec, F.; Fréchet, J. M. J. *J. Chromatogr. A* **2007**, *1140*, 140-146.

26 Viklund, C.; Svec, F.; Fréchet, J. M. J. *Chem. Mater.* **1996**, *8*, 744-750.

27 Yu, C.; Davey, M. H.; Svec, F.; Fréchet, J. M. J. *Anal. Chem.* **2001**, *73*, 5088-5096.

28 Sáfrány, Á.; Beiler, B.; László, K.; Svec, F. *Polymer* **2005**, *46*, 2862-2871.

Chapter 3

Confinement Effects on the Morphology of Photopatterned Porous Polymer Monoliths for Capillary and Microchip Wall Coatings*

3. 1 INTRODUCTION

Polymer monoliths formed by photoinitiated free-radical polymerization have been widely explored as an attractive alternative to particle packing in column preparation [1-5]. Their physical and chemical properties can be readily tuned by adjusting the polymerization mixture composition. Additionally, their bicontinuous porous structures cause lower pressure drop along the bed compared to silica beads packing. The most appealing advantage of polymer monoliths for integrated multifunctional microsystems is the relatively simple preparation afforded by photopatterning. Integration of porous polymer monoliths into microfluidic devices has received increased interest in many applications, such as mixers, reactors, solid-phase extraction, and chromatography [6-14]. Lab-on-a-chip devices span a large size range from a few to several hundred micrometers. Here we report that capillary and microfluidic channel dimensions and surface chemistry profoundly affect the porosity and nature of confined monolithic structures. This behavior is similar to that of sol-gel systems, which become much more porous when polymerized under confinement [15-17], even though the polymerization reactions are considerably

*A version of this chapter has been published as He, M.; Zeng, Y.; Sun, X.; Harrison, D. J. *Electrophoresis*. **2008**, 29, 2980-2986.

A portion of this chapter was presented as He, M.; Zeng, Y.; Harrison, D. J. *Proceedings of Micro-Total Analysis Systems*. **2007**, Volume 1, 805-807.

different for the two types of materials. The observed deformation of the random porous structure under confinement make it difficult to predict the polymer monolithic structures that will be realized in a microchannel or narrow bore capillary. To understand and control these effects we have studied the effect of monolith pore size, surface wetability and capillary and microchannel dimensions on polymer monolith morphology. Such information is critical for designing capillary and microfluidic chip devices with polymer monoliths.

In this chapter, monolith structures have been evaluated by Hg intrusion porosimetry, non-destructive three-dimensional laser scanning confocal microscopy and scanning electron microscopy. We have found that the smaller the ratio of capillary to bulk monolith pore size, the greater the deviation of the product morphology from a bulk polymerization product; as the confinement dimension decreases, the uniformity of polymer microglobule dispersion is decreased. The monolithic structure evolves to a single polymer layer on the wall surface in the extreme deformation limit. This observation leads to a versatile method of preparing relatively thick, (~ 300 nm), very uniform surface coatings. We demonstrate that this method provides a novel surface modification method to control electroosmotic flow, and prevent non-specific adsorption of proteins during capillary electrophoresis. Thick coatings have been of interest, due to their greater durability, improved surface coverage, and increased absorption capacity. Eeltink et al [18] formed thick porous monolith wall coatings using a technique in which the capillary was spun rapidly during polymerization, and showed good durability resulted with high quality separations. Huang and Horvath [19] had earlier illustrated the usefulness of thick coatings with a tube in a tube concept to create coatings with similar

performance, although long polymerization times were used *in-situ*. Huang et al [20, 21] used surface-confined living radical polymerization to grow ~20 nm thick films and showed they could achieve better surface coverage with these thicker films. Here, we show that using the confinement effect to give relatively uniform thick wall coatings is fast and efficient, requiring less time and less complication than these other methods. Unlike the spinning capillary approach this method is applicable to the microfluidic chip format, and allows the ability to immobilize various surface functional groups in photolithographically defined patterns.

3.2 MATERIALS AND METHODS

3.2.1 Microfluidic Device Fabrication

Microchannels were fabricated in 0.6-mm thick 0211 glass substrates (Corning Glass Works, Corning, NY, USA) using chemical etching methods described previously [22]. Single straight channels were etched in a series of depths (5, 10, 15, 20, 50 μm), with the same mask feature width of 600 μm, for investigation of confinement effects on monolith morphology. The etched channel plates, with holes drilled for external access, were bonded with 0.17-mm thick 0211 glass cover plates for LSCM observation. For microchip electrophoresis, a 40-μm offset double–T injector was used, as sketched in Figure 3.1. Channels were ~20-μm wide and ~7-μm deep. The buffer and injection channels were 5-mm long, and the separation channel was 2-cm long.

3.2.2 Preparation of Photo-polymerized Monoliths

The internal surfaces of glass channels and fused-silica capillaries with a series of internal diameters (Polymicro Technologies, Phoenix, AZ) were treated with either 1-[3-(trimethoxysilyl)propyl] urea or triethoxy(octyl)silane to generate hydrophilic and hydrophobic surfaces, respectively. Benzoin, toluene, 1-octanol, 1-decanol, cyclohexanol, 2-hydroxyethyl methacrylate (HEMA), ethylene dimethacrylate (EDMA), [2-(methacryloyloxy) ethyl] trimethylammonium chloride (META) and butyl methacrylate (BMA) were obtained from Aldrich. HEMA, EDMA, META and BMA were purified by passing through basic alumina columns (mesh 650, activity I). Functional monomers, crosslinkers, porogenic solvents, and photoinitiator (benzoin, 1 wt% of monomers) were mixed following the recipes listed in Table 3.1. The mixtures were purged with nitrogen for 5 min to remove dissolved oxygen prior to introduction into capillaries or microchannels by syringe pump (PHD2000, Harvard apparatus, USA). Filled capillaries and microchannels were sealed with silicone rubber or tape, and photolyzed immediately. A custom printed photomask was used to selectively expose a portion of the channel to a UV transilluminator equipped with six 15-W 312-nm tubes (model TS-312R, Spectroline, Spectronics Corp., Westbury, NY) as shown in Figure 3.1 (left). To photopattern capillaries, the polyamide outside coating was removed to open an exposure window. Then the formed monoliths were flushed with methanol and water (1:1 v/v) to remove unreacted reagents.

Table 3.1 The recipes and the resultant pore sizes for different photo-polymerized monoliths.

	Monomer (wt %)	Crosslinker (wt %)	Porogenic solvent (wt %)	Exposure[a] (min)	Pore size[b] (μm)
Monolith 1	HEMA 12%	EDMA 28%	Toluene 60%	16	3.18
Monolith 2	HEMA 10.5%	EDMA 24.5%	1-octanol 65%	9	1.05
Monolith 3	BMA 12%	EDMA 28%	1-octanol 60%	9	0.84
Monolith 4	HEMA 10.5%	EDMA 24.5%	1-decanol 19.5% +cyclohexanol 45.5%	9	0.44

a) Photolysis time at 312 nm.
b) Pore size measured using Hg porosimetry on bulk prepared monolith samples

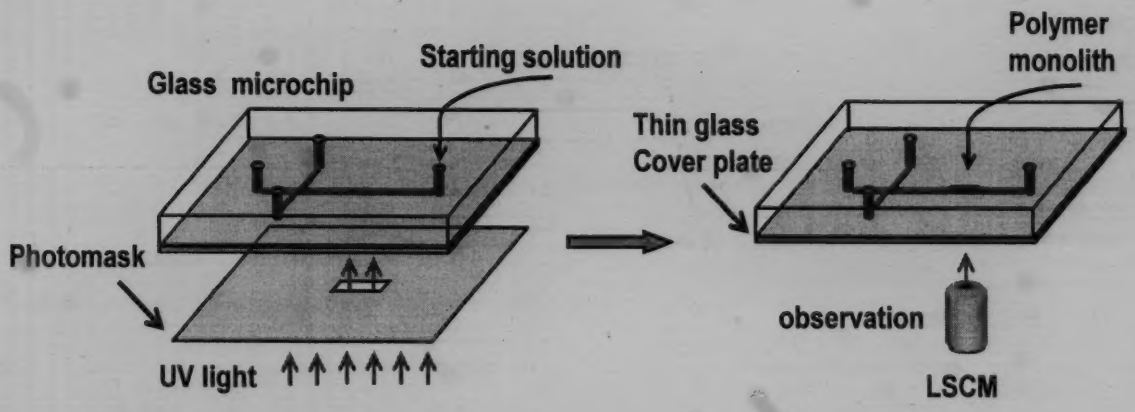

Figure 3.1 Experimental setup for (left) photoinitiated polymerization and (right) laser scanning confocal microscopy, with a double T separation chip illustrated.

3.2.3 Characterization of Monoliths

At least 4 channels or capillaries were prepared for each monolith composition. Capillaries were cut at different positions for characterizing the cross-sectional morphology of monoliths. The cross-sections were coated with gold and observed by SEM (Leo 1430, Oberkochen, Germany). Multiple cross-sections were evaluated by SEM to identify when cutting the capillary might have damaged the monolith morphology, and images presented are for the densest cross sections observed for a given set of polymerization conditions. Pore size measurement using Hg intrusion porosimetry (Autopore IV 9500, Micromeritics) could only be performed on bulk prepared monolith material, since a large amount is required. These polymerizations were done in purged glass vials. Prior to measurement, the resultant bulk monoliths were extracted in a Soxhlet apparatus with methanol for 12 h, and dried in a vacuum for 12 h.

To complement the SEM observations, LSCM (Carl Zeiss, LSM 510) was used to achieve nondestructive 3D characterization of monolithic structures in glass chips. Some glass chip cross-sections (prepared by snapping the chip along a scribe line) were also evaluated by SEM to show that the two methods gave similar results. An oil-immersion Plan-Neofluar, 40×/1.3 objective lens was used. The step size in the z-direction was 0.3 μm for all samples, thus the resolution in the z-direction is estimated to be 0.6 μm according to the Nyquist sampling theorem. A 543-nm HeNe laser was used to scan over a 51.2 × 51.2-μm^2 area in the plane perpendicular to the z-direction (x-y plane), producing a stack of 2D sliced images composed of 512×512 pixels (See right of Figure 3.1). A mixture of dimethyl sulfoxide and benzyl alcohol (4:1 v/v, refractive index ~1.5) containing Rhodamine dye was used to match the refractive index of monoliths for deep

imaging. This solvent was tested to confirm that it does not distort the monolithic structures noticeably over the observation period. The 3D reconstructions of LSCM images were performed using Imaris software with surface rendering (Bitplane AG, Zurich, Switzerland) [23-25]. The volume fraction of monolith was depicted by counting the number of pixels in each 2D binarized image [26, 27] by using image processing software (Metamorph, Molecular Devices, Sunnyvale, CA, USA).

3.3 RESULTS AND DISCUSSION

3.3.1 Monolith Structure as a Function of Confinement

Conventional polymer monoliths are fabricated in fused silica capillaries, typically with an internal diameter larger than 50 μm. In general, the globular internal structure of a molded monolith is porous, dense and uniform, as is illustrated in Figure 3.2. Monolith 1 was formed in capillaries with different internal diameters from 50 to 700 μm. Figure 3.2 shows 8.5 kx magnified images of the porous structure. The porous morphology for the same type of monolith seemed to be the same for capillaries from 50-700 μm diameters. There was no structural difference for polymer monoliths fabricated in several batches of polymerization. The size of the spherical microglobules, flow-through pores and the density distribution are consistent for all capillaries equal to or larger than 50 μm.

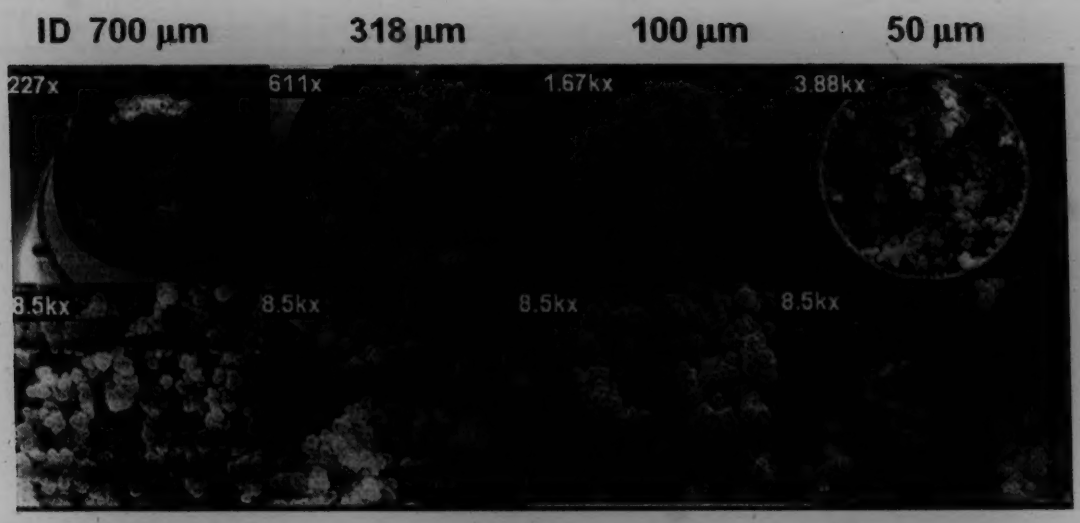

Figure 3.2 The morphology of Monolith 1 photopatterned in fused-silica capillary with different internal diameters. Recipe is listed in Table 3.1.

When we investigated the morphology of photo-polymerized monoliths within the confined geometry of small capillaries, we found a significant impact as a result of spatial restrictions. The monolith formulations, identified in Table 3.1, are numbered in order of decreasing pore size. Monoliths 1, 2 and 4 use HEMA as the monomer and EDMA as the crosslinker with various porogenic solvents. Monolith 3 is a more hydrophobic material, using BMA as the monomer and EDMA as crosslinker. Figure 3.3A shows SEM images of the evolution of the morphology for these four formulations, as the internal diameters of the capillary decreased from 50 to 5 µm. The pore sizes determined by Hg intrusion measurements are shown in Figure 3.3B for the corresponding bulk polymerized materials. As the capillary diameter decreases, structural differences are seen relative to the bulk materials for all the monoliths evaluated. We will refer to these as deformations

and they are evidenced by irregular large voids and sparsely distributed polymer grains. In the extreme case, the spatially random porous structure evolves to a single polymer layer attached to the capillary wall, as seen in Figure 3.3A (a) for 5 and 10-μm i.d. capillaries. Deformation onsets at different confinement dimensions, depending on the bulk pore size of the material. For instance, in Figure 3.3A (a), deformation is seen in a 20-μm i.d. capillary for Monolith 1, which has the largest pore size of 3.18 μm in the bulk material. In Figure 3.3A (b) and (c), Monoliths 2 and 3 with 0.84-1.05-μm pore sizes are not significantly affected in a 20-μm capillary, but show notable deformation in a 10-μm capillary. Monolith 4, with a 0.44-μm pore size in the bulk state, only exhibits significant deformation in a 5-μm capillary, as seen in Figure 3.3A (d).

The typical D-channel shape of a glass microfluidic chip was also studied, in which the channel shape is quite different than a capillary, but the smallest dimension of confinement, the channel depth, is in the same range of 50, 20 and 10 μm. While SEM provides very graphic and readily interpreted images, LSCM provides a non-destructive, direct 3D visualization with better depth resolution over a large volume. LSCM avoids the possible sampling bias that is induced by imaging only cross-sections created by shearing. The reconstructed LSCM images shown in Figure 3.4 and Figure 3.5, illustrate that both Monolith 1 and 3 undergo deformation to give more sparse and irregular structures as the microchannel depth decreased. For example, arrows in Figure 3.5 indicate the more sparse density distribution of Monolith 3 formed within a 10-μm constriction. Monolith 1 deformed in a 20-μm confinement, while Monolith 3 only deformed in a 10-μm deep channel, consistent with the results for capillaries shown in Figure 3.3A.

The observations above indicate that the extent of deviation from bulk porosity under confinement strongly depends on the ratio of the characteristic length of the confined space to the monolith pore size. The exact geometry of the confined space does not seem to be as important. The microchannel geometry is D-shaped and the capillary is cylindrical in shape. Nevertheless, the deformation occurred in the same smallest size dimension regardless of the geometry. We observed that a larger microchannel is better for forming the full porous structure with a sharp interface, which is particularly desirable for microchips integrated with porous polymer monolith.

A rough rule of thumb established from this study is that the bulk-like porosity is observed for a confinement dimension to pore size ratio > 10, and significant deviation is observed for a ratio < 5. Extreme deformation of bulk porous monoliths results in the formation of a fairly smooth polymer layer on the surface of the capillary, and no material in the central region (see Figure 3.3, 5-μm capillaries).

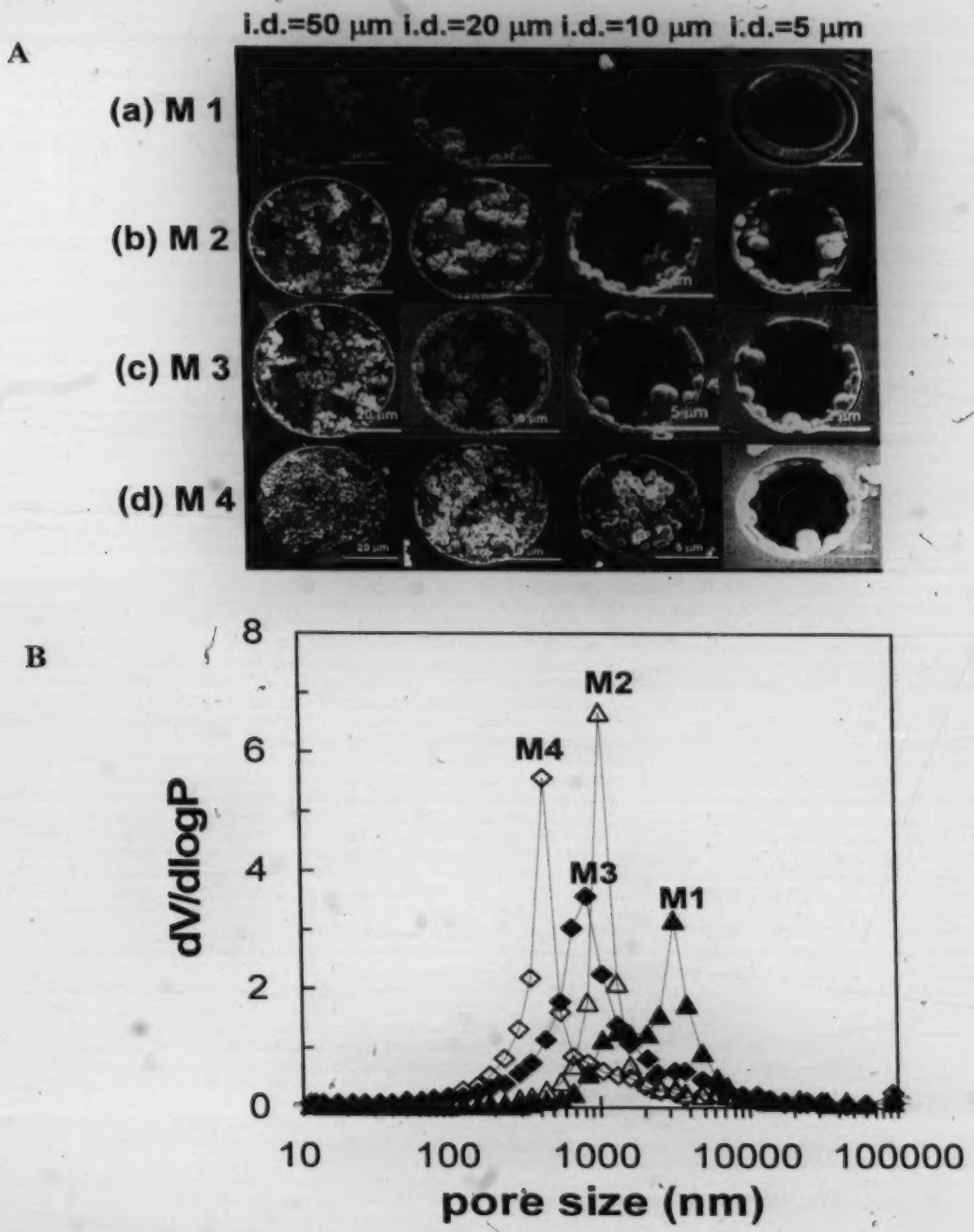

Figure 3.3 Evolution of the morphology of photo-polymerized monoliths with decreasing capillary diameter (**A**), and the corresponding pore size of the bulk polymer by Hg intrusion porosimetry (**B**). Numbers refer to the monolith number. No surface treatment was used on the capillaries. See Table 3.1 for composition of each monolith (M1 refers to Monolith 1, etc.).

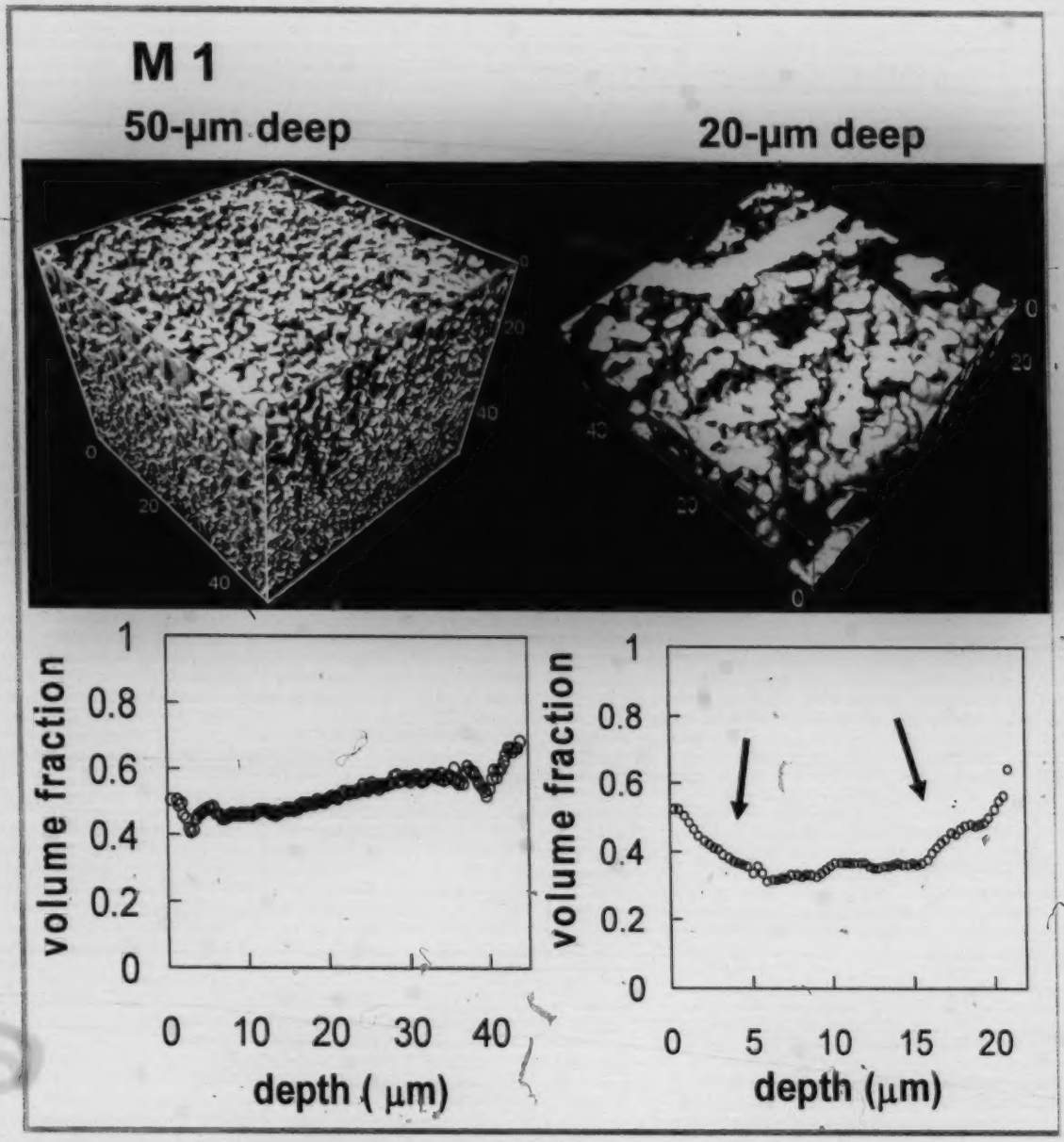

Figure 3.4 The reconstructed LSCM images and depth profiles of volume fractions for hydrophilic Monolith 1 photo-polymerized within microchannels that were not surface treated. LSCM was conducted in negative mode, thus the pore is dark and the solid monolith is bright.

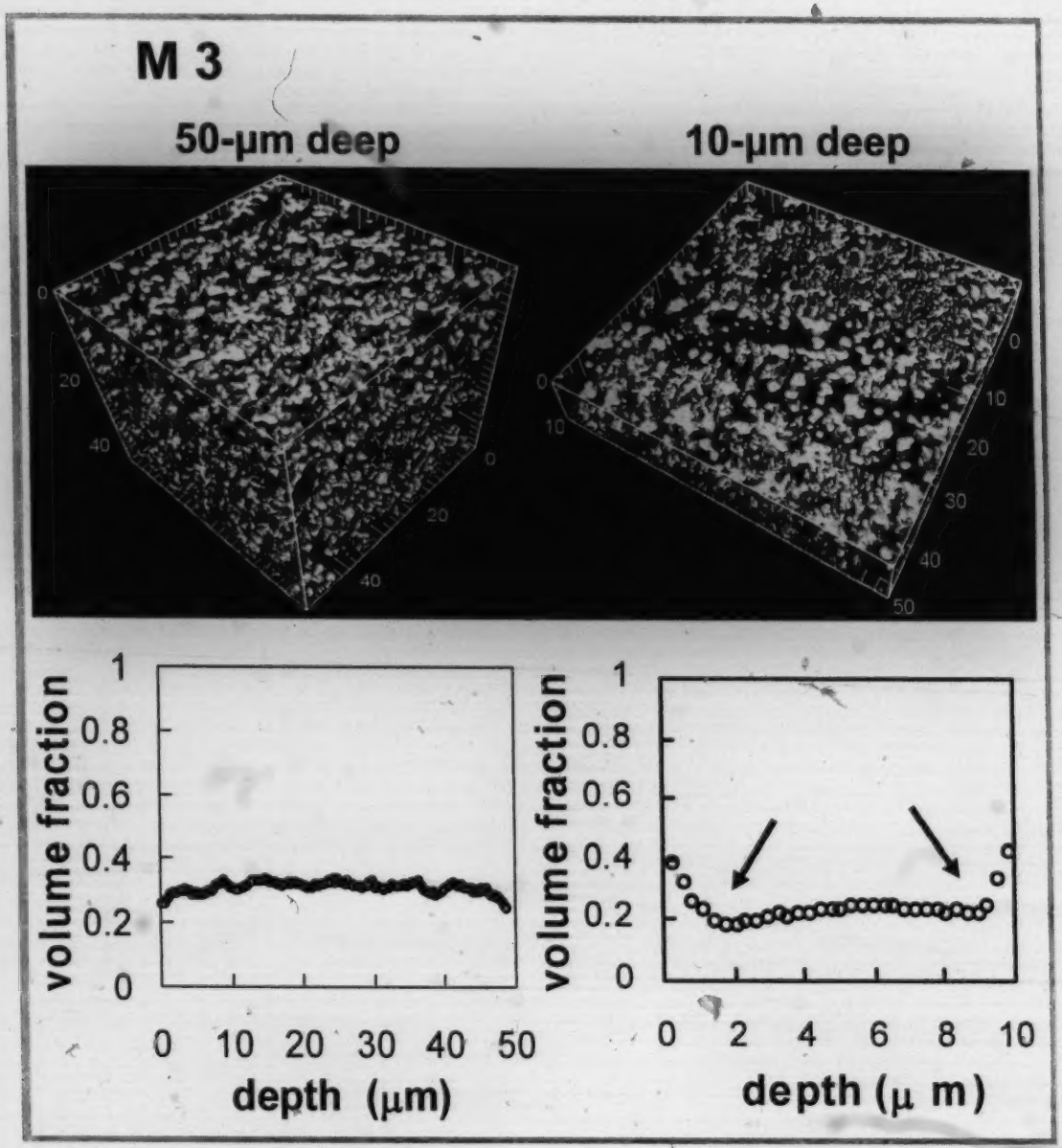

Figure 3.5 The reconstructed LSCM images and depth profiles of volume fractions for hydrophobic Monolith 3 photo-polymerized within microchannels that were not surface treated. LSCM was conducted in negative mode, thus the pore is dark and the solid monolith is bright.

3.3.2 Parameters affecting deformation of monolith materials

We hypothesize that the observed deformations result from wall effects that are related to the interplay of wall-surface wetting with polymer-particle interfacial tension, and the relative dynamics of diffusion-based transport with respect to polymerization kinetics. If the nucleation and polymerization rate for spheroid formation in solution is low compared to the length of time required to diffuse to the capillary surface, then surface coating will be favored. If the opposite is true then conventional bulk polymerization will be favored. This interplay can be manipulated by changing the capillary size, as is evidenced by the results in Figure 3.3. In a 5-μm radius capillary we can estimate a diffusion time from centre to wall, based on the Nernst layer approximation, of about 12 ms for a typical diffusion coefficient of 1×10^{-5} cm^2 s^{-1}, and 312 ms for a 25-μm radius, providing some estimation of the time domain of importance. It has been stated that polymerization kinetics slow down for monoliths with larger pore sizes [28], which is consistent with our observation that such monoliths are deformed to a greater extent in larger diameter capillaries than that of monoliths with smaller pore sizes.

Coating of the wall surface will be dependent upon the wetability of the surface by the polymer material, and this process will compete with the tendency to form the small spheroidal particles observed in bulk monoliths. A high rate of surface coating will induce diffusion-based transport to the surface of the capillary, depleting the bulk zone of monomer. In deformed monoliths we do in fact observe a large decrease in polymer density outside the wall region in the distribution profiles obtained from LSCM image stacks (Figure 3.4 and Figure 3.5, bottom). A change in surface-polymer interaction should affect the tendency to form a surface coating. This effect is demonstrated in Figure

3.6, which shows the morphology of relatively hydrophilic Monolith 1 formed in microchannels with either hydrophilic (a) or hydrophobic surfaces (b). Figure 3.7 (a) shows that for the hydrophilic surface, the density distribution of hydrophilic Monolith 1 in the center region is only 0.37, compared to 0.45 in the presence of a hydrophobic surface. Figure 3.7 A and B demonstrate that when both the surface and polymer are hydrophilic, the deformation is more severe within a confined space (15 μm in this example). Consistent with the proposed role of surface wetability, the hydrophobic Monolith 3, containing BMA monomer, was deformed more under the influence of the hydrophobic surface than the hydrophilic one, as shown in Figure 3.7C. These observations show that the monolith density in the central region varies with surface chemistry of the microchannels and confirm that surface tension or wetting plays a role.

Surface chemistry effects appear to be most significant when the confinement dimension to polymer pore size ratio is around 10, where the deformation phenomenon tends to onset. For large channels (e.g., 50 μm deep), we obtained the same density distribution in both cases of surface chemistry (see Figure 3.8 A and B). Conversely, for polymer to pore size ratios of 2 or less (e.g., 5 μm size with monolith 1), surface coatings are formed regardless of our attempts to control the surface chemistry (hydrophilic, hydrophobic and untreated surfaces all form thick walled coatings.) We conclude the confinement dimensions, and thus transport versus polymerization rate issues, are the main cause of deformation, and that surface chemistry is most relevant to the specific size at which deformation onsets. In small enough dimensions the nucleation and polymerization rate for spheroid formation in bulk is always lower than the time required

to diffuse to the surface and a wall coating is apparently favored regardless of surface chemistry.

This evolved single polymer layer under confinement is localizable by photopatterning, though the structure is deformed and restricted within confined dimension. It indicates that photo-initiated free radical polymerization undergoes to form the evolved polymer layer. It was demonstrated by using a 5-μm i.d. capillary as reaction mold to partially expose under UV light. As seen in Figure 3.9, the SEM images clearly show that the polymer layer was formed under confinement and restricted to the exposure zone, and no polymerization in non-exposure zone. This property and applications will be discussed in detail in Chapter 4.

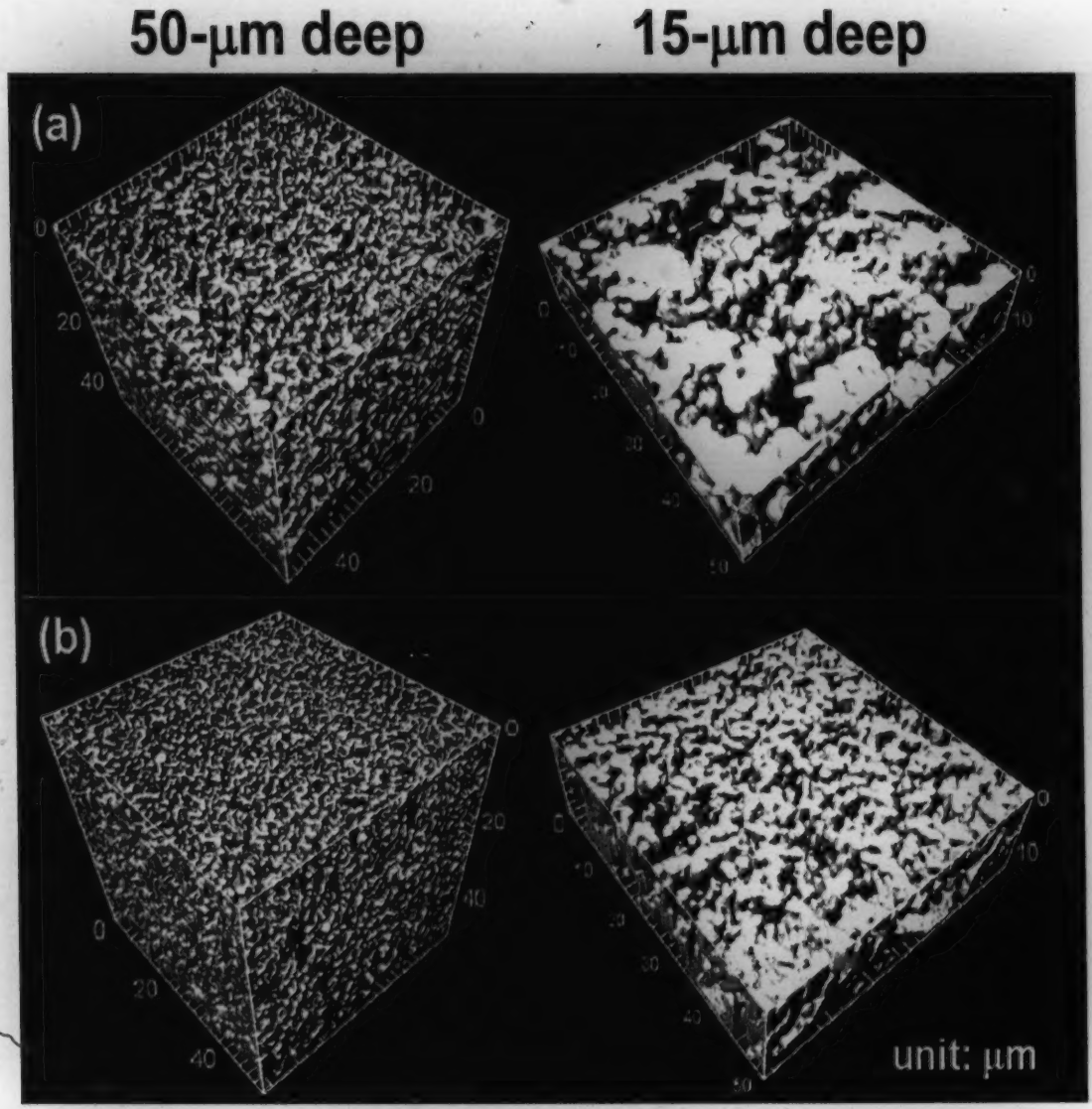

Figure 3.6 The reconstructed laser scanning confocal micrographs of the morphology of Monolith 1 photo-polymerized in microchannels with the indicated depths, and with different surface chemistries: (a) a hydrophilic surface and (b) a hydrophobic surface.

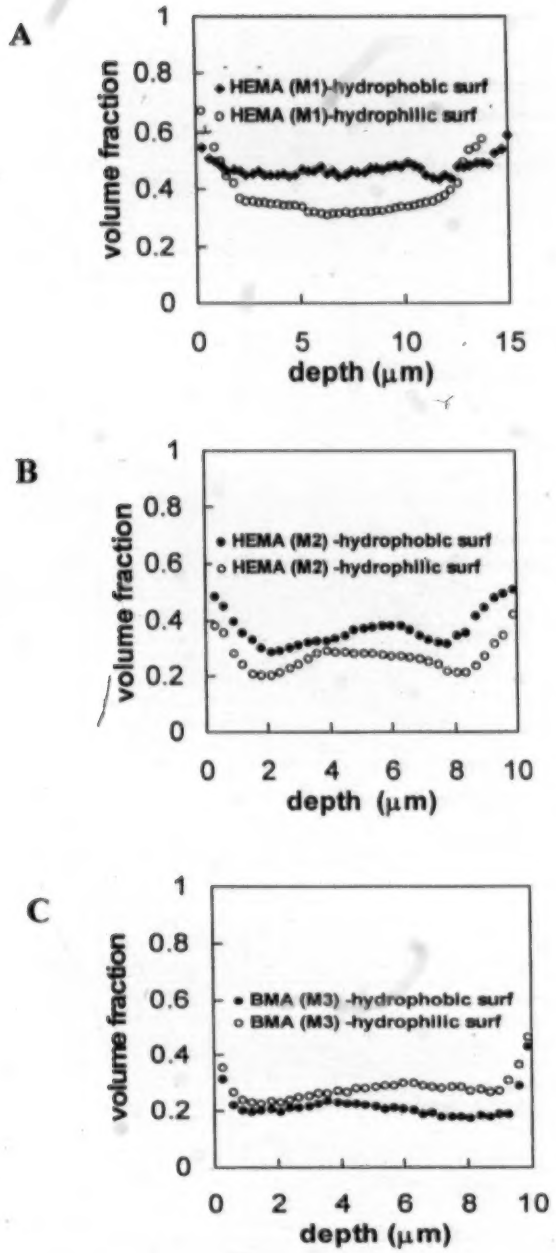

Figure 3.7 The depth profiles of volume fraction for hydrophilic Monolith 1(**A**) and Monolith 2 (**B**), as well as hydrophobic Monolith 3 (**C**) within microchannels with either hydrophilic or hydrophobic surface chemistry.

A

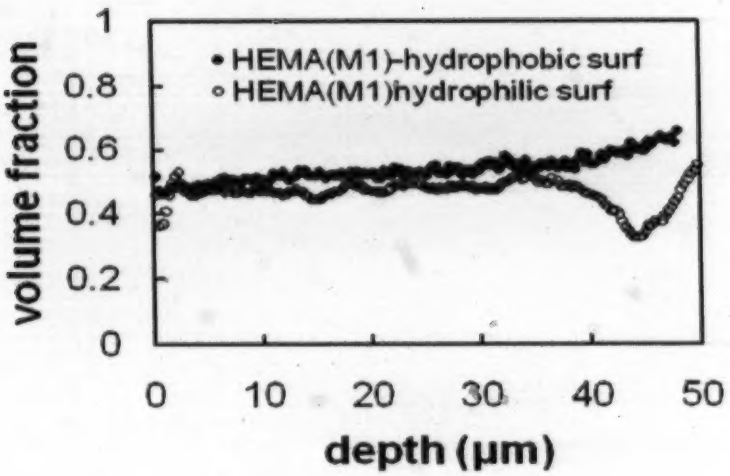

B

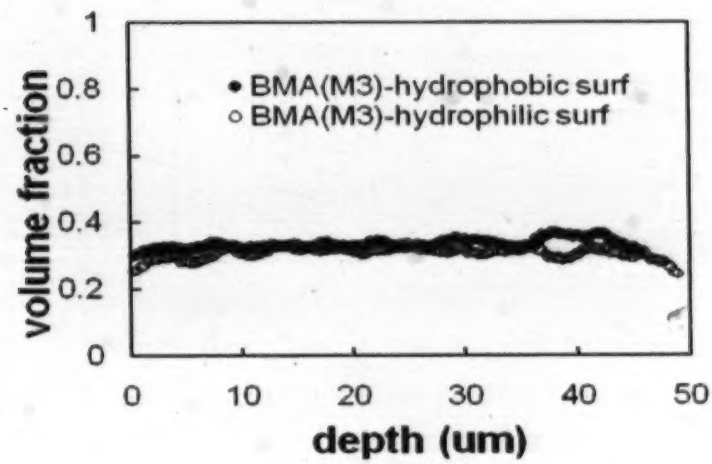

Figure 3.8 The depth profiles of volume fraction for hydrophilic Monolith 1 (**A**) and hydrophobic Monolith 3 (**B**) within microchannels with either hydrophilic or hydrophobic surface chemistry.

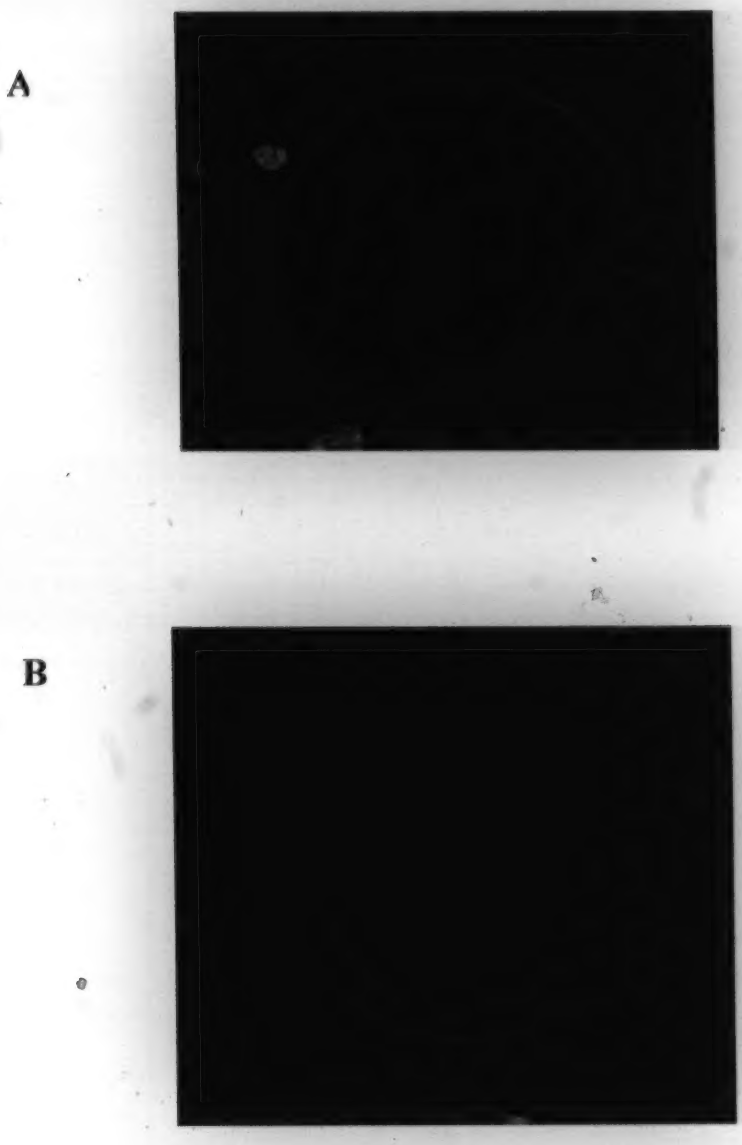

Figure 3.9 The cross-sectional SEM images of the 5-μm i.d. capillary. Monolith 1 was photo-polymerized under confinement with partial UV light exposure. **A**: non-exposure zone; **B**: exposure zone.

3.3.3 Thermal-initiated Polymerization Under Confinement

Photoinitiation has distinct advantages over thermal initiation in a polymerization, such as fast speed, ability to localize the zone of polymerization, and high yield [29]. Nevertheless, thermally initiated polymerization to form the porous media can be useful. In thermally initiated polymerization, the initiator decomposes to form free radicals, but this rate is lower compared to photolysis [30]. We investigated polymer structure evolution under confinement when using thermally initiated polymerization in a 20-μm capillary. The monolith recipe used to produce the structures shown in Figure 3.10 does not create a monolith when using photo-initiated and confined in a 20-μm i.d. capillary, instead giving a film that coated the wall. However, under thermal-initiation, the porous structure does evolve over time. At 10 min and 16 min, a polymer layer with a bumpy surface was formed inside the capillary. With increasing reaction time, this polymer material grows spherical particles from the surface to the center of the capillary, as can be seen in Figure 3.10 at 22 min and 30 min. After 240 min of thermal-polymerization, this polymer material forms a nearly uniform, fully porous structure. Another study was performed in a 10-μm capillary, as shown in Figure 3.11. We always obtained a thick polymer layer on surface wall, regardless of the reaction time from 20 min to 120 min. However, the layer surface becomes much rougher and more bumpy after longer reaction time. It is possible to clog the small capillary after long reaction time, as seen in Figure 3.11 D. We thought the different response of the thermal polymerization under confinement is due to the different kinetics compared with photo polymerization. As seen from the SEM images, the smaller particles and pore size were formed by using thermally initiated polymerization with the same recipe as photopolymerization. The lower

decomposition rate of the thermal-initiator caused the later stage of phase separation, thus formed the smaller pore size of the structure. In turn, particle formation speed will be higher for the smaller pore size monolith. Additionally, the higher temperature will cause the faster speed to form the spheriodal particles. Overall, it has a strong tendency to form the spheroidal particles in bulk by thermal-polymrization and deform in smaller confined dimension, which followed our previous hypothesize in Section 3.3.2 that deformations result from the relative dynamics of diffusion-based transport with respect to spheroid formation speed.

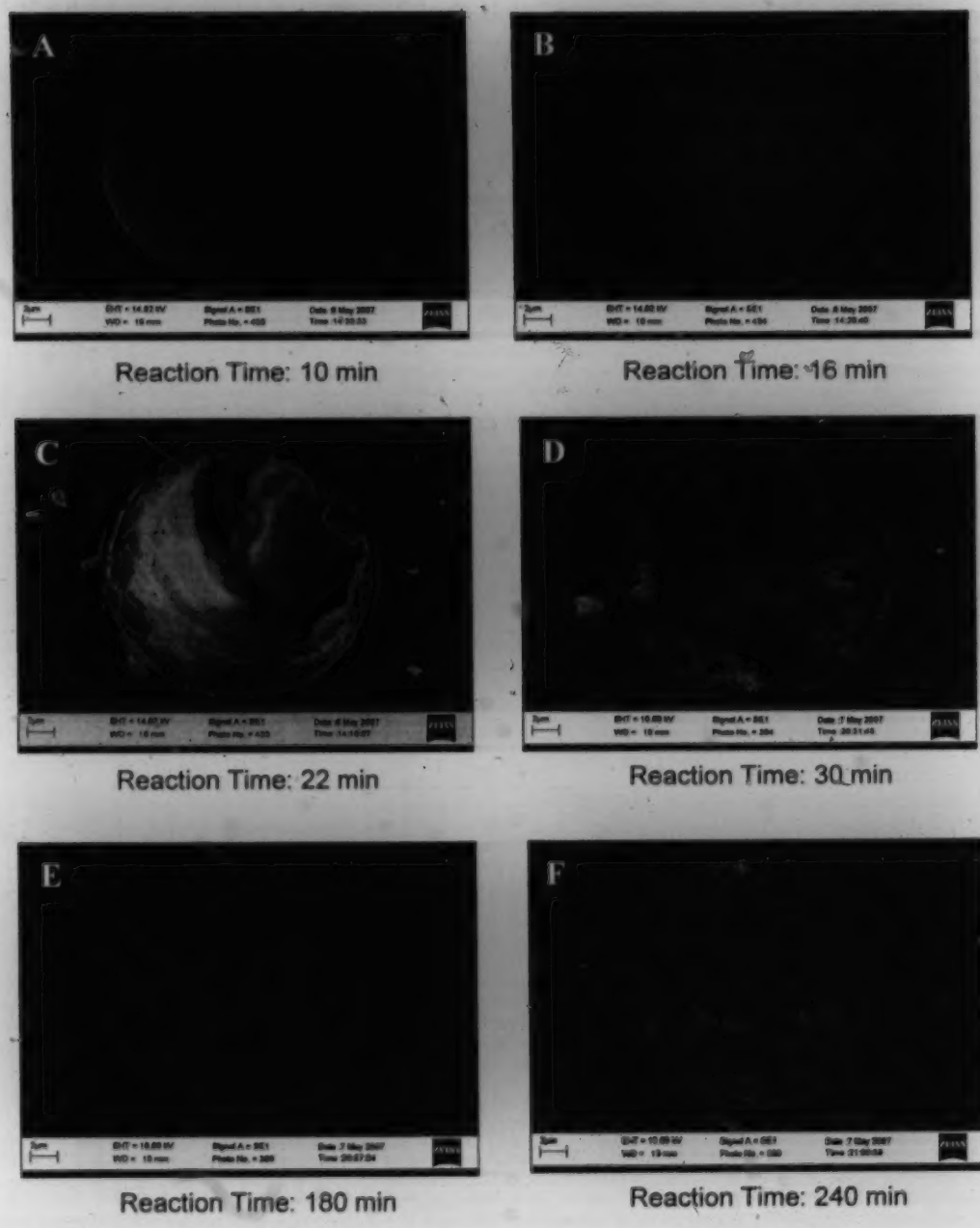

Figure 3.10 The morphology of polymer monolith evolved with the reaction time under confinement (20-μm i.d. capillary) by using thermal-initiated polymerization. Reaction time **A**: 10 min; **B**: 16 min; **C**: 22 min; **D**: 30 min; **E**: 180 min; **F**: 240 min. Polymerization conditions: HEMA 12 wt%, EDMA 8 wt%, toluene 80 wt%, AIBN 0.2 wt%, T= 85 ℃. This recipe only forms the film layer in 20-μm i.d. capillary by using photo-initiated polymerization.

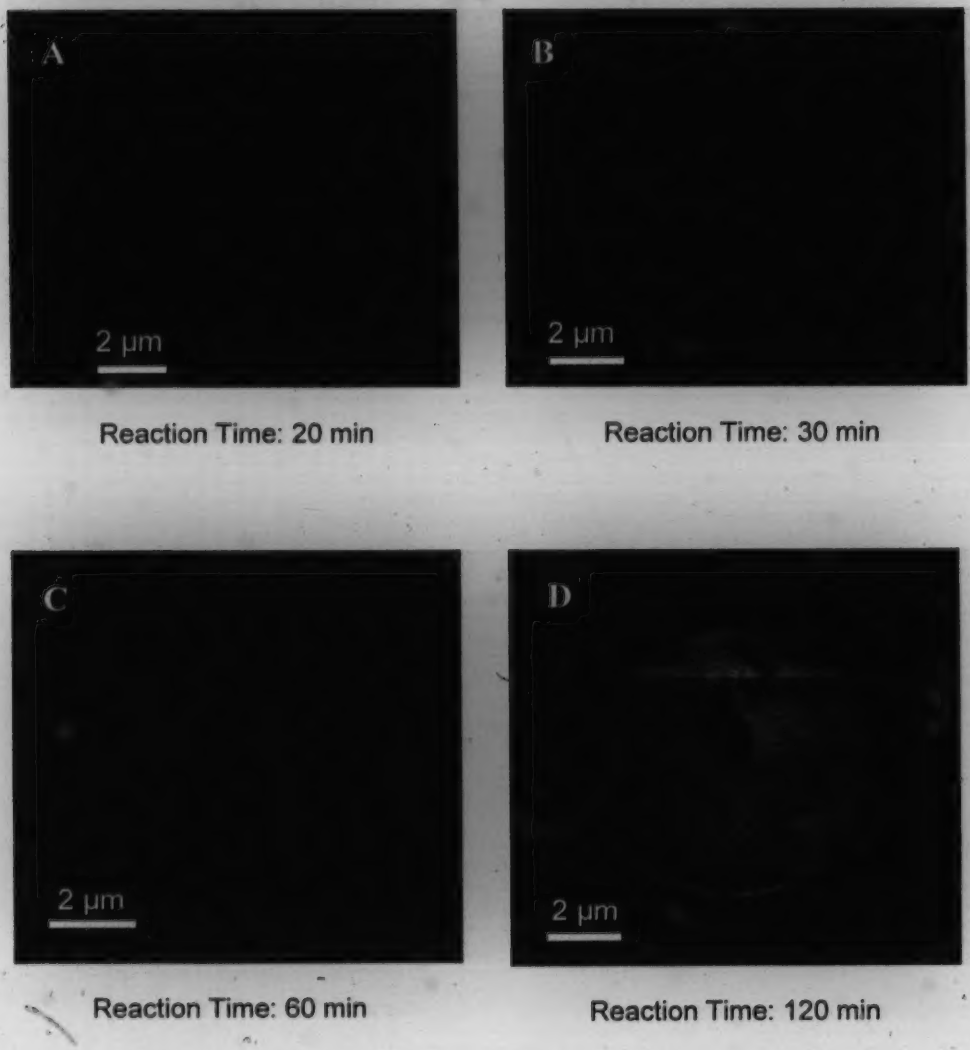

Figure 3.11 The morphology of polymer monolith evolved with the reaction time under confinement (10-µm i.d. cpillary) by using thermal-initiated polymerization. Reaction time **A**: 20 min; **B**: 30 min; **C**: 60 min; **D**: 120 min. Polymerization conditions are the same as indicated in Figure 3.10.

3.3.4 Functionalization of Thick Wall Coatings Formed by Confinement Effect

Our studies clearly lead to a novel coating strategy that takes advantage of deformation under confinement, and provides a route to thick wall coatings with photopatternable properties. This is a fast and effective strategy to create robust, multifunctional coatings for applications such as EOF control, or for the prevention of non-specific adsorption in chromatography or CE.

Particularly interesting, the polymer layer surface can be photografted with versatile functional groups. UV photografting of polymer surface was performed through a single-step in which the grafting solution contains both the photoinitiator and the monomer. UV excitation promotes abstraction of hydrogen atoms from the polymer surface, leading to the formation of surface-bound radicals that may then initiate a surface graft polymerization process [31]. Figure 3.12 shows cross-sectional images of microchannels and a capillary coated with a positively charged film ~300 nm thick used to reverse EOF. We first formed a neutral polymer layer of HEMA and EDMA within the confined structure and then photografted cationic META, bearing a quaternary ammonium group, to obtain exposed charged groups on the surface. From the SEM images, we can clearly see a smooth and uniform polymer film attached to the internal surface of the capillary and glass microchannel. This application will be discussed in detail in Chapter 4.

A

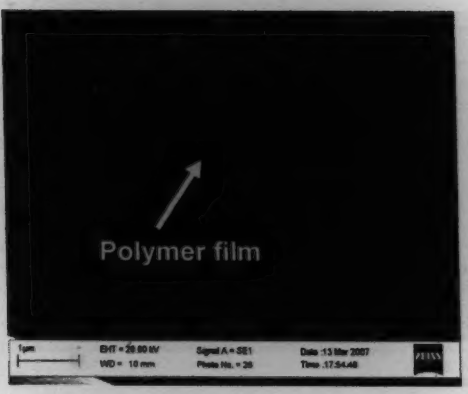

B

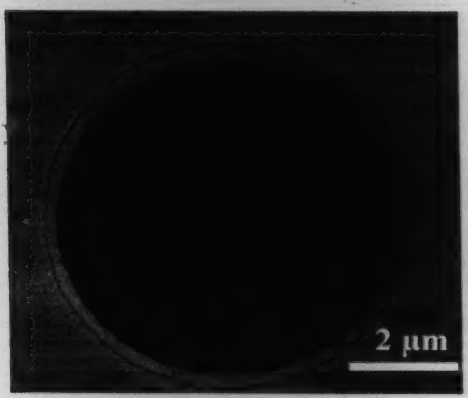

C

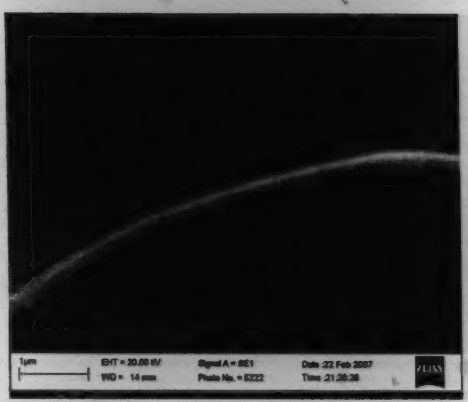

Figure 3.12 The confinement effect was employed to achieve uniform, thick wall coatings in microchannels (**A**) and a capillary (**B**)-(**C**). Microchannel depth is 10 µm and width is 50 µm. The internal diameter of capillary is 10 µm. Polymerization conditions: HEMA 4 wt%, EDMA 6 wt%, toluene 90 wt%, benzoin 0.06 wt%, UV 312 nm for 10 min. Photografting: META 20wt%, tertbutyl alcohol 60 wt%, water 20 wt%, 4-(dimethylamino) benzonphenone 0.2 wt%, UV 312 nm for 120 s.

3.4 CONCLUSIONS

The morphology of porous monolith materials is profoundly affected by polymerization within an enclosed space, once the dimensions are within a factor of 5 to 10 of the pore size of the bulk monolith. Surface tension or surface wetability plays a significant effect once the confining dimension is within a factor of 5-10 of the bulk pore size. The material becomes more porous and the dispersion of the microglobules of polymer becomes less uniform as this ratio decreases. Under extreme deformation of the bulk structure it is possible to obtain uniform surface coatings with thickness in the range of hundreds of nanometers. The results also illustrate that monolith pore size and microfluidic device dimensions must be considered in concert if reproducibly uniform porous monolith materials are to be produced within a microchip. Intriguingly, these morphological changes should allow simple and spatially selective fabrication of both open tubular coatings and porous monolithic structures within a microfluidic device by judicious choice of device dimensions. This extreme deformation provides a novel coating strategy to create robust, thick wall coatings for versatile applications.

3.5 REFERENCES

1 Yu, C.; Xu, M. C.; Svec, F.; Fréchet, J. M. J. *J. Polym. Sci., Polym. Chem.* **2002**, *40*, 755-769.

2 Svec, F.; Fréchet, J. M. J. *Ind. Eng. Chem. Res.* **1999**, *38*, 34-48.

3 Gac,S. L.; Cantier, J.; Camart, J. C.; Olivé, C. C.; Rolando, C. *J. Chromatogr. B* **2004**, *808*, 3-14.

4 Reichmuth, D. S.; Shepodd, T. J.; Kirby, B. J. *Anal. Chem.* **2005**, *77*, 2997-3000.

5 Chirica, G. S.; Remcho, V. T. *J. Chromatogr. A* **2001**, *924*, 223-232.

6 Tan, A.; Benetton, S.; Henion, J. D. *Anal. Chem.* **2003**, *75*, 5504-5511.

7 Throckmorton, D. J.; Shepodd, T. J.; Singh, A. K. *Anal. Chem.* **2002**, *74*, 784-789.

8 Rohr, T.; Yu, C.; Davey, M. H.; Svec, F.; Fréchet, J. M. J. *Electrophoresis* **2001**, *22*, 3959–3967.

9 Peterson, D. S.; Rohr, T.; Svec, F.; Fréchet, J. M. J. *Anal. Chem.* **2002**, *74*, 4081-4088.

10 Logan, T. C.; Clark, D. S.; Stachowiak, T. B.; Svec, F.; Fréchet, J. M. J. *Anal. Chem.* **2007**, *79*, 6592-6598.

11 Stachowiak, T. B.; Svec, F.; Fréchet, J. M. J. *Chem. Mater.* **2006**, *18*, 5950-5957.

12 Hasselbrink, E. F.; Jr.; Shepodd, T. J.; Rehm, J. E. *Anal. Chem.* **2002**, *74*, 4913-4918.

13 Wen, J.; Guillo, C.; Ferrance, J. P.; Landers, J. P. *Anal. Chem.* **2007**, *79*, 6135-6142.

14 Fintschenko, Y.; Choi, W. Y.; Ngola, S. M.; Shepodd, T. J. *Fresenius J. Anal. Chem.* **2001**, *371*, 174-181.

15 Kanamori, K.; Yonezawa, H.; Nakanishi, K.; Hirao, K.; Jinnal, H. *J. Sep. Sci.* **2004**, *27*, 874-886.

16 Kanamori, K.; Nakanishi, K.; Hirao, K.; Jinnai, H. *Langmuir* **2003**, *19*, 5581-5585.

17 Suzumura, Y.; Kanamori, K.; Nakanishi, K.; Hirao, K.; Yamamichi, J. *J. Chromatogr. A* **2006**, *1119*, 88-94.

18 Eeltink, S.; Svec, F.; Fréchet, J. M. J. *Electrophoresis* **2006**, *27*, 4249-4256.

19 Huang, X.; Horváth, C. *J. Chromatogr. A* **1997**, *788*, 155-164.

20 Huang, X. Y.; Doneski, L. J.; Wirth, M. J. *Anal. Chem.* **1998**, *70*, 4023-4029.

21 Huang, X. Y.; Wirth, M. J. *Macromolecules* **1999**, *32*, 1694-1696.

22 Oleschuk, R.D.; Shultz-Lockyear, L.L.; Ning, Y.; Harrison, D. J. *Anal. Chem.* **2000**, *72*, 585-590.

23 Tata, B. V. R.; Raj, B. *Bull. Mater. Sci.* **1998**, *21*, 263-278.

24 Jinnai, H.; Nishikawa, Y.; Koga, T.; Hashimoto, T. *Macromolecules* **1995**, *28*, 4782-4784.

25 Jinnai, H.; Nishikawa, Y.; Morinoto, H.; Koga, T.; Hashimoto, T. *Langmuir* **2000**, *16*, 4380-4393.

26 Jinnai, H.; Nakanishi, K.; Nishikawa, Y.; Yamanaka, J.; Hashimoto, T. *Langmuir* **2001**, *17*, 619-625.

27 Jinnai, H.; Koga, T.; Nishikawa, Y.; Hashimoto, T.; Hyde, S. T. *Phys. Rev. Lett.* **1997**, *78*, 2248-2251.

28 Svec, F.; Fréchet, J. M. J. *Chem. Mater.* **1995**, *7*, 707-715.

29 Joshi, M. G.; Rodriguez, F. *J. Polym. Sci., Polym. Chem.* **1988**, *26*, 819-826.

30 Fouassier, J. P. *Prog. Org. Coat.* **1990**, *18*, 229-252.

31 Stachowiak, T. B.; Mair, D. A.; Holden, T. G.; Lee, L. J.; Svec, F.; Fréchet, J. M. J. *J. Sep. Sci.* **2007**, *30*, 1088-1093.

Chapter 4

Photopatternable Multifunctional Coatings Based on Confinement Effect for Fast Microchip Electrophoresis of Proteins and Peptides*

4.1 INTRODUCTION

Protein separation based on microfluidic chips is a rapidly developing field, in which one of the most important factors is the design of a stable wall coating to minimize adsorption of analytes and improve resolution. A channel with an easily reproducible homogeneous surface is essential for further development of microanalytical systems. Extensive efforts have been devoted to wall coating and surface modification in microfluidic devices [1-4] made of different materials, which include glass [5-8], poly(dimethyl siloxane) (PDMS) [9-13], poly(methyl methacrylate) (PMMA) [14, 15], polycarbonate (PC) [16, 17] and poly(ethylene terephthalate) glycol (PETG) [18, 19]. However, more durable, more uniform coating with better coverage, and that are more easily localized spatially, remain a key target for further improvement of the performance of microchips. In addition, microfluidic devices with complex designs require surface modification with simple preparation procedures that are less time consuming.

---

* This chapter has been presented as He, M.; Harrsion, D. J. *Proceedings of 91st Canadian Chemistry Conference.* **2008**, 104.

A portion of this chapter has been published as He, M.; Zeng, Y.; Sun, X.; Harrison, D. J. *Electrophoresis*. **2008**, 29, 2980-2986.

Currently, surface coating is mainly focused on monolayers, bilayers or covalently bonded polymers utilizing a siloxane bridge [20, 21]. The hydrolytic stability of many thin coatings is generally not sufficient to withstand repeated long term washing, as well as being limited to operation at pH lower than 8 and above ~2 [22, 23]. Coating films with a thickness of more than 20 nm are attracting increased interest [24, 25], due to their improved coverage and enhanced durability. The first covalent bonding of a polymer film for capillary electrophoresis is reported by Hjertén in 1985 [26]. Huang and Horvath [27] had earlier illustrated the usefulness of thick coatings with a "tube in a tube" concept. The Remcho group [28] reported a new procedure for preparing thick polymethacrylate films used for open tubular liquid chromatographic and electrochromatographic separations. Other groups did substantial work in developing thick wall coatings [29-31]. However, the thickness of the film coating is seldom reported to be well controlled. We have reported that the morphology of porous monolith materials is profoundly affected by polymerization within an enclosed space, once the dimensions are within a factor of 5 to 10 of the pore size of the bulk monolith [32, 33]. This observation leads to a versatile method of preparing uniform surface coatings with a tunable thickness. Here, we show that this coating strategy is fast and efficient, requiring less time and less complication than these other methods, and allows the ability to immobilize various surface functional groups in photolithographically defined patterns.

Adsorption of proteins onto the wall of microchips during separation can lead to poor reproducibility, band broadening, and reduced efficiency. Meanwhile, variation in EOF is an even more severe problem. A thick coating of neutral, inert polymer would prevent both protein adsorption and EOF. Thick polymer coatings have the additional

advantages of reducing EOF, because the high viscosity of the polymer film prevents flow in the region of high potential. In this chapter, we present the control of EOF in glass microchannels, using coatings with neutral and charged films that are prepared by photopolymerization in confined spaces. HEMA was chosen in this study because of its wide biocompatible applicability, and its excellent stability against hydrolysis in alkaline solution [25]. The ability of this hydrophilic, neutral thick wall coating to support the electrophoretic separation of proteins was assessed. The durability of the coating was also evaluated by long-term measurement of the reproducibility of protein separations. Separation of proteins in acidic and basic buffer both showed high efficiency and good reproducibility. In addition, the surface chemistry of the coating was tailored to fit specific applications by photografting, which can be precisely localized in the desired location using photomasks [34]. This photopatternable grafting was demonstrated in this chapter by immobilizing sulfobetaine methacrylate (SBMA) for fast separation of proteolysis digest.

4.2 MATERIALS AND METHODS

4.2.1 Microfluidic Device Fabrication

Microchannels were fabricated in 0.6-mm thick corning 0211 glass substrates (Corning Glass Works, Parkridge, IL) at the University of Alberta NanoFab Lab, using published procedures detailed in Chapter 2. For microchip electrophoresis, a cross-injector was used illustrated in Figure 4.3A. Channels were ~24-μm wide and ~7-μm deep. The injection channels were 5-mm long, and the separation channel was 2-cm long.

4.2.2 Samples and Reagents

Benzoin, toluene, HEMA, EDMA, META, SBMA were obtained from Aldrich. HEMA, EDMA, META were purified by passing through basic alumina columns (mesh 650, activity I). Preparation of FITC-labeled protein (Sigma) and peptide solutions used the following procedures: trypsin inhibitor, BSA, IgG, carbonic anhydrase and ovalbumin were dissolved in 500 mM sodium bicarbonate (Ph 9.2) with a final concentration of 1 mg/mL. Protein solution was then thoroughly mixed with 100 mM FITC in acetone (final molar ratio of protein to FITC was 1:3). All protein-FITC solutions were shaken in the dark overnight at room temperature and then purified by centrifugal filter (10 k Da cutoff, Microcon, Millipore) before use. Before separation, native proteins were diluted with running buffer solution (20 mM phosphate buffer) to a final concentration of ~10^{-5} M each. The proteolysis sample was obtained from FITC-conjugated BSA digested by chymotrypsin (Sigma) in 400 mM ammonium bicarbonate buffer (pH 8.0) at 37 °C overnight. The BSA concentration is 2 mg/ml, mixed with chymotrypsin at a ratio of 1:50. Before CE separation, the digest was diluted 120-fold with 20 mM phosphate buffer at a pH of 9.5.

4.2.3 Preparation of Photo-polymerized Coatings

For activation, the microchannels were rinsed with water, 0.2 M sodium hydroxide, water, 0.2 M HCl, and acetone, sequentially. Then a solution of 20% (v/v) 1-[3-(trimethoxysilyl) propyl] urea in ethanol with 10% acetic acid was sucked through each channel for 0.5 h using vacuum tubing. Finally, microchannels were rinsed with ethanol and dried in an oven overnight at 75°C. The glass channels need to be kept in clean and

dry conditions to achieve the successful coating. Figure 4.1 shows a digital photo of a successful coating with clear and transparent channel surface.

Functional monomers, crosslinkers, porogenic solvents, and photoinitiator (benzoin, 1 wt% of monomers) were mixed, then purged with nitrogen for 5 min to remove dissolved oxygen, prior to introduction into microchannels. Filled microchannels were sealed with tape and photolyzed immediately. The channels were exposed to a UV transilluminator equipped with six 15-W 312-nm tubes (model TS-312R, Spectroline, Spectronics Corp., Westbury, NY). After coating, microchannels were flushed with methanol and water (1:1 v/v).

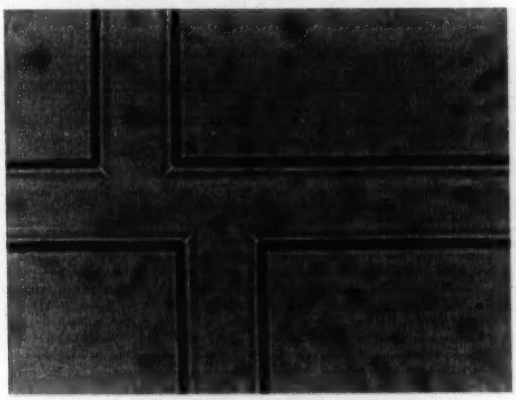

Figure 4.1 Digital photo of one μCE device coated with polymer film based on confinement effect. Polymerization conditions: HEMA 4 wt%, EDMA 6 wt%, toluene 90 wt%, benzoin 0.06 wt%, UV 312 nm for 10 min. The film is invisible due to its thickness ~200 nm.

4.2.4 Microchip Electrophoresis Conditions

Samples were prepared with deionized water (18.2 MΩ) obtained from an Ultrapure water system (Millipore, Milford, MA). Solutions were passed through a 0.22-μm pore size filter before use. EOF was measured using the current-monitoring method [35]; the

two buffers used were 20 mM and 18 mM phosphate, adjusted to different pH values from 3 to 10, as shown in Table 4.1, and measured by a pH meter (model 875MP, Fisher Scientific, U.S.A.). To measure the stability of the EOF over time, the channels were flushed and stored in water between measurements. Protein samples were loaded from reservoir 1 by applying a 1000-V potential to reservoir 2 with other reservoirs grounded to form a "pinched" injection plug illustrated in Figure 4.3 A and Figure 4.7. Separations were monitored using epifluorescence microscopy and a photomultiplier tube with an optical bandpass filter (508-533nm). Fluorescence signals were obtained by exciting with a 488-nm argon ion laser beam. Labview programs (National Instruments Corp., Austin, TX) written locally were used for data acquisition with a sampling rate of 200 Hz.

Table 4.1 Buffer prepared with varied pH value for EOF measurement.

pH	3	4	5	6	7		8	9	10
Na_2HPO_4 (mM)	6.8	11.1	13.5	15.6	18.6	NaH_2PO_4 (mM)	5.4	5.0	4.7
citric acid (mM)	13.2	8.8	6.4	4.3	1.4	Na_3PO_4 (mM)	14.6	15.0	15.3

pH was adjusted by NaOH or H_3PO_4 to the exact value.

4.3 RESULTS AND DISCUSSION

4.3.1 Photopatternable Properties of Coatings in Confined Channels

The photo-polymerization process enables spatial definition of the location of columns within a multiplexed chip design. Figure 4.2 illustrates the ability to photopattern this coating. A glass microchannel with ~24-μm width and ~7-μm depth was partially coated with neutral hydrophilic polymer film (HEMA), using a mask on the

right part of the channel, as shown in Figure 4.2 A. FITC-BSA (0.5 mg/mL) was introduced into the channel and incubated for 10 min, then rinsed away with 20-mM phosphate buffer solution (pH 7.0) for 5 min. The fluorescent signal after washing was collected by an epifluorescence microscopy for both coated and uncoated parts, as shown in Figure 4.2 B. The signal was compared with background from a coating that was not incubated with FITC-BSA. The fluorescence intensity across the channel was analyzed using ImageJ software. Nonspecific interaction between the surface and protein is always present, and the magnitude depends on the surface properties. As can be seen, the fluorescent signal due to FITC-BSA was dramatically decreased by coating the channel, which indicates the coating was quite effective for reducing non-specific adsorption of protein. This well known effect is due to the polar surface of glass, which electrostatically interacts with proteins. The small spots in the image were from tiny beads of solution on the surface. The signal from the two side-walls of the channel is much stronger than that of center, which is due to the increased accumulation of fluorescent signal using top-view observation. Comparison of the background signal for the coating verses the signal after exposure to FITC-BSA shows that there must still be some proteins adsorption. The spatially defined interface between the coated and uncoated parts of the channel can be clearly seen in Figure 4.2 A. A sharp and clear interface indicates this photo-polymerized coating method allows lithographical patterning in microfluidic devices.

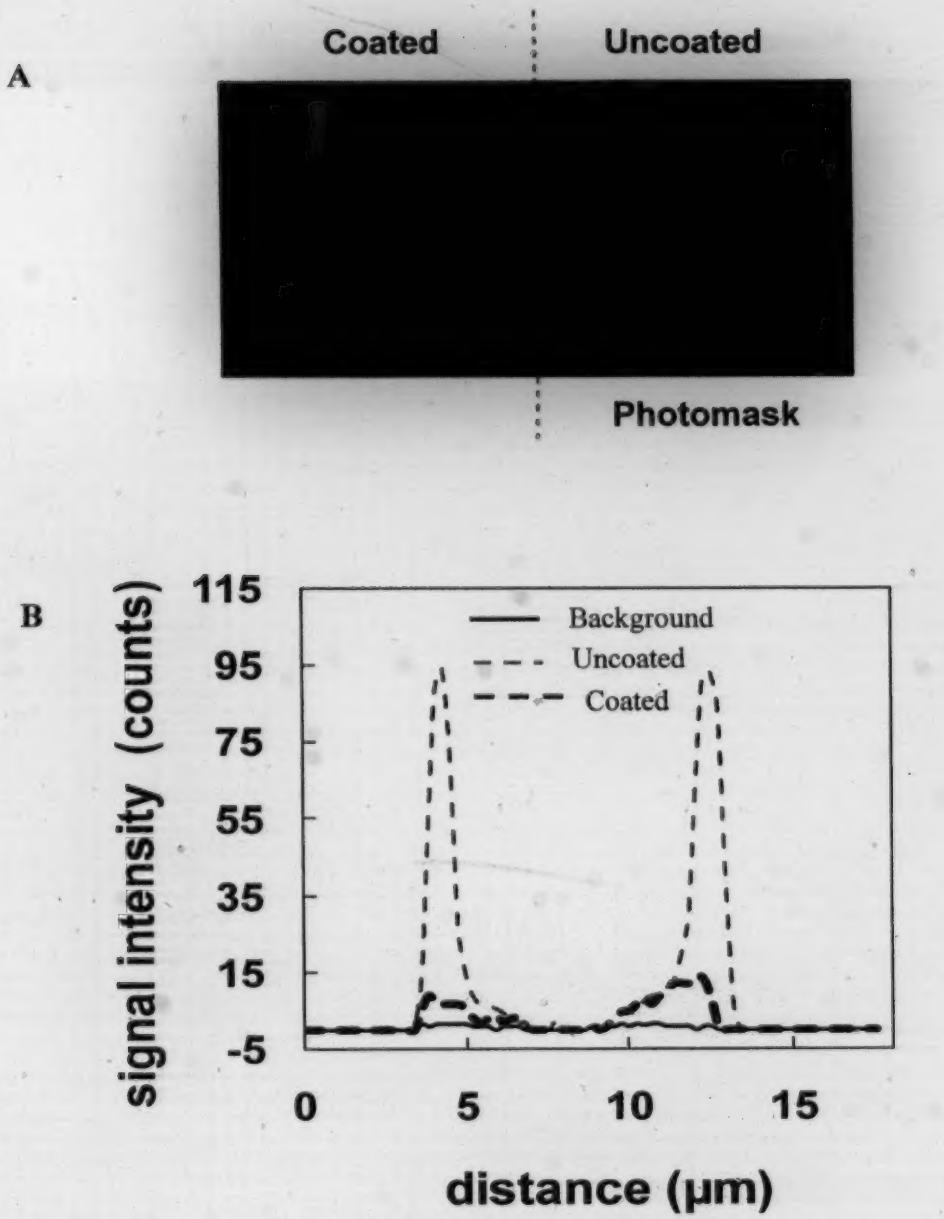

Figure 4.2 A: The fluorescent digital photo of a glass microchannel with half coated film. **B**: Intensity of fluorescence signal as a function of distance across the microchannel. Polymerization conditions: HEMA 4 wt%, EDMA 6 wt%, toluene 90 wt%, benzoin 0.06 wt%, UV 312 nm for 10 min.

4.3.2 Tunable Thickness of the Photopolymerized Coating

The extreme deformation of bulk porous monoliths in narrow capillaries results in the formation of a thick polymer layer on the surface. It is possible to obtain uniform surface coatings with a thickness in the range of hundreds of nanometers. We designed a microfluidic electrophoresis device with ~24-μm wide and ~7-μm deep channel dimensions, as illustrated in Figure 4.3 A. A solution containing the monomer, crosslinker and solvent was transferred into the microchannel and polymerized under UV light exposure. As sketched in Figure 4.3 B, photografting then allows the ability to immobilize various surface functional groups. The total preparation time of the graft is less than 10 min. Figure 4.3 C shows the cross-sectional image of a microchannel coated with a positively charged polymer film, formed by grafting META onto a HEMA/EDMA coating. The enlarged images clearly show the fairly smooth polymer layer attached on the wall of the glass channel, with 260-nm thickness. Most interestingly, the thickness of the coating can be varied by tuning the monomer concentration, as shown in Figure 4.3 D. Here, the monomer concentration is given as a weight percentage, which is defined by the weight of (HEMA+EDMA) divided by total weight of (HEMA+EDMA+toluene). The ratio of (HEMA: EDMA) is kept at 4:6. Toluene is used as the solvent. The film thickness was measured by using image analysis software. We measured the thickness of 20 batches of polymer coatings formed within different confinement dimensions, as listed in Table 4.1. Under extreme deformation, the thickness of the film, made using the same monomer concentration, is almost the same, regardless of the confined space. This result indicates that the thickness is directly related to the concentration of the monomer and not influenced by the confined space. As we can see, the film thickness is 212 nm when using

a polymerization mixture containing 10 wt% monomer. Moreover, the thickness is increased to 642 nm when the monomer content is 40 wt%. This thickness depends non-linearly on increased monomer concentration, as shown in Figure 4.4 A. The above results demonstrate that we can use capillary size and monomer concentration to control the formation of cross-linked films and their film thickness. However, continuously increasing the monomer concentration to 60 wt% gave the gel-like structure shown in Figure 4.4 B. Referring to Table 2.2, when the monomer content is larger than 50 wt%, the polymer structure changes dramatically, loosing the normal monolith properties, and the confinement effect is not applicable when this occurs.

Table 4.2 The film thickness measured from 20 batches of coatings in different space dimensions.

Capillary i.d.	Film thickness in different batches of coatings (nm)					Average thickness (nm)
5 μm	656.4	672.3	680.5	560.5	680.5	658.9±42.5
	711.5	637.4	668.5	693.7	627.9	
10 μm	662.2	701.1	623.2	681.7	603.8	626.6±43.1
	584.3	603.8	564.8	610.5	631.2	

Polymerization conditions: total monomer 40%, toluene 60%, UV 312 nm for 16 min.

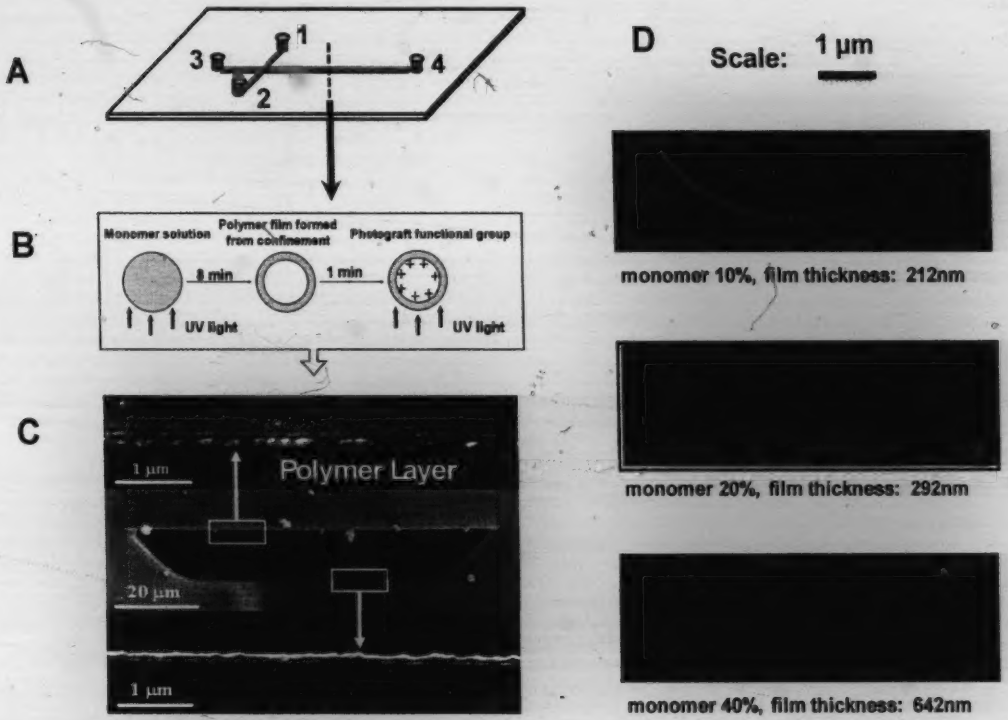

Figure 4.3 A: Microfluidic scheme for μCE separation. 1: sample reservoir, 2: sample waste reservoir, 3: buffer reservoir, 4: buffer waste reservoir. **B**: Schematic illustration of photopatternable polymeric coatings based on the confinement effect and it was employed to achieve uniform, cationic thick wall coatings in microchannel shown in SEM image **C** by photografting. Conditions: HEMA 4 wt%, EDMA 6 wt%, toluene 90 wt%, benzoin 0.06 wt%, UV 312 nm for 10 min. Photografting: META 20wt%, tertbutyl alcohol 60 wt%, water 20 wt%, 4-(dimethylamino) benzonphenone 0.2 wt%, UV 312 nm for 120 s. **D**: SEM images showing the dependence of film thickness on monomer concentration. The polymerization was conducted in 10-μm internal diameter silica -fused capillaries and the recipe for each film thickness is indicated in Figure 4.4 A.

A

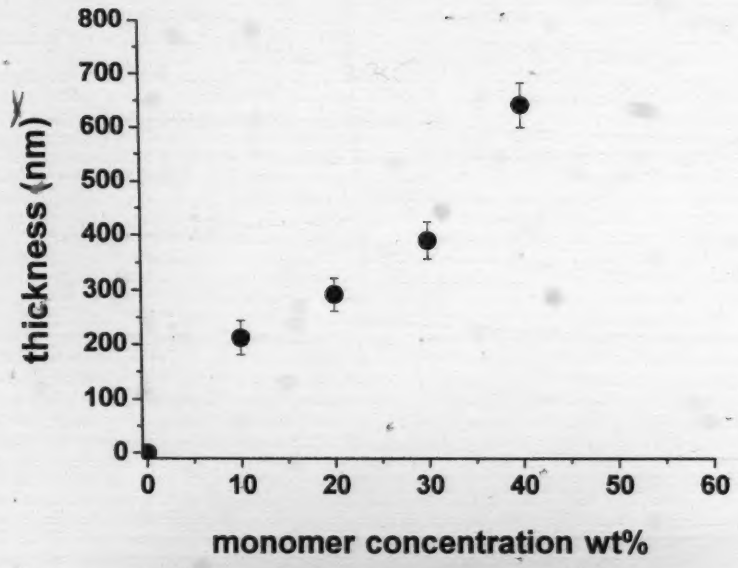

B

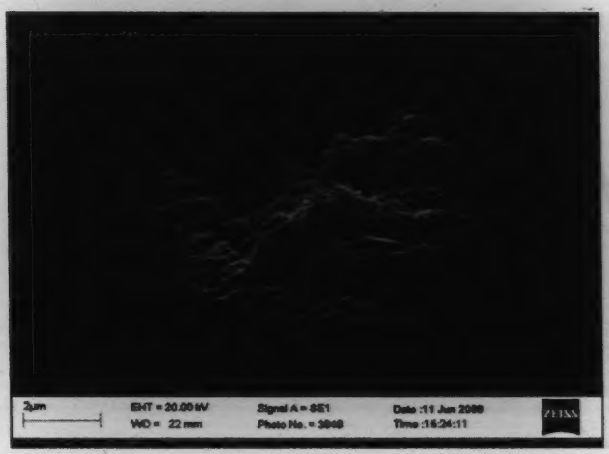

Figure 4.4 A: The relationship between the film thickness and the monomer concentration. Monomer percentage = (HEMA+EDMA)/(HEMA+EDMA+toluene), which varied from 0 wt% to 60 wt%. The ratio of HEMA: EDMA is fixed at 4:6. Each deviation is calculated from 10 batches of polymerization. **B**: SEM image showing the polymer morphology with component ratio lies in the gel-like structure range in Table 2.2. The polymerization was conducted in 10-μm internal diameter silica -fused capillaries. UV 312 nm exposed for 16 min.

4.3.3 EOF Monitoring for Evaluating the Surface Modification

EOF directly reveals the surface properties and charge status by showing the flow rate and direction. Therefore, surface coatings can be evaluated by measuring EOF. In our first study, we prepared a coating layer using a one-step method, by directly adding the positively charged monomer META into the starting mixture. The polymer layers contain the quaternary ammonium group of META and produce a reversed EOF. The magnitude of the EOF was measured, and is shown in Table 4.2 to be in the range of 5×10^{-5} $cm^2 V^{-1}s^{-1}$. Due to the cross-linked polymerization, the charged functional group is largely buried in the polymer network. This EOF magnitude is relatively small and not sufficient to maintain stable electrokinetically controlled flow for many applications, for which 10^{-4} cm^2/Vs is preferable.

Table 4.3 EOF measurements for one-step coating method by adding META into starting mixture.

	Column 1	Column 2	Column3	bare capillary
Average EOF $cm^2V^{-1}s^{-1}$ (n=6)	-5.12×10^{-5}	-5.82×10^{-5}	-6.11×10^{-5}	6.18×10^{-4}

Polymerization conditions: HEMA 2 wt%, EDMA 4 wt%, META 4 wt%, toluene 90 wt%, benzoin 0.1wt%, UV 312 nm for 10 min. The measurements were performed in 10 μm i.d. capillaries at room temperature with 20 mM phosphate buffer (pH7.0).

Compared to the one-step method, two-step photografting can produce a larger reversed EOF in the range of 10^{-4} $cm^2 V^{-1}s^{-1}$. Surface grafting ensures specific groups are on the surface. Figure 4.5 shows the EOF is dependent on the photografting time when using the two-step method. Longer grafting time gives a bit larger reversed EOF, but not dramatically, as seen by comparing the results for grafting 60 s to 240 s. The grafting reaction is fast enough to give close to the maximum density of functional groups on the

surface within a short time. Meanwhile, the two-step grafting method is quite repeatable, as shown by the error bars in Figure 4.5 (RSD ~3%, n=4 different batches).

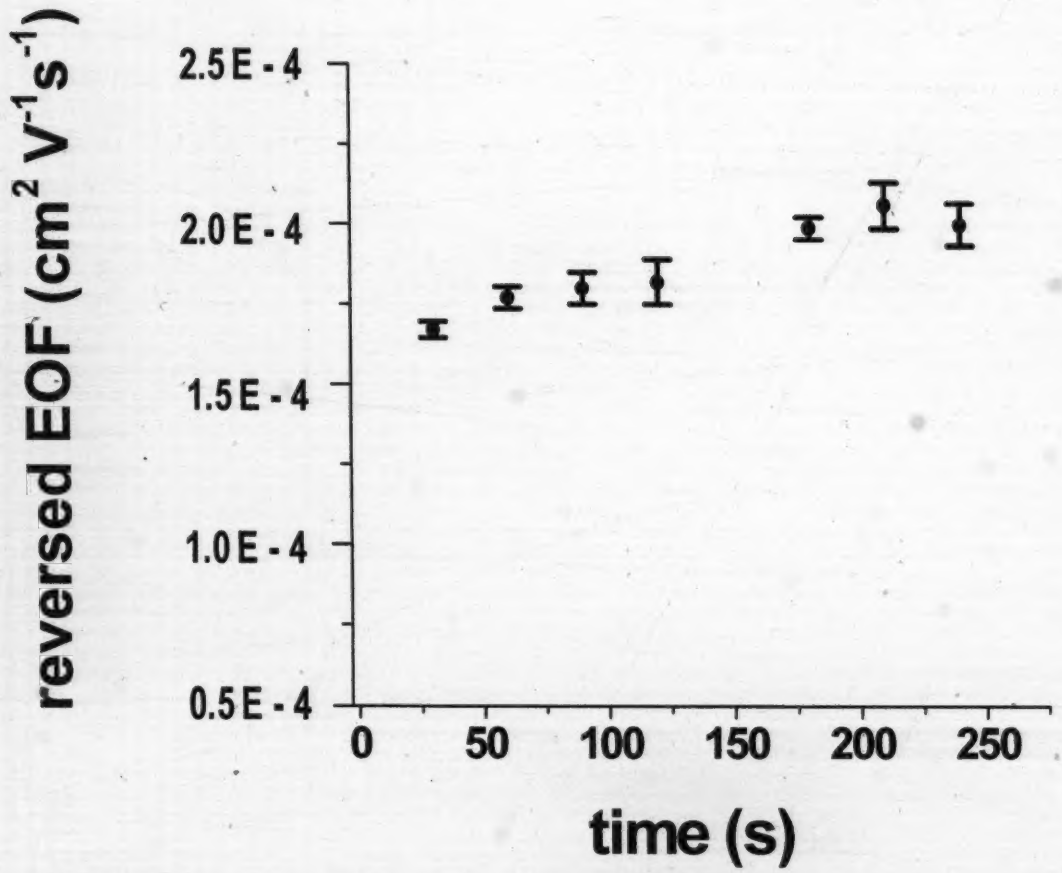

Figure 4.5 The reversed EOF magnitude affected by photografting time and the reproducibility of two-step photografting method. The deviation is from four batches of coatings. Polymerization conditions: HEMA 4 wt%, EDMA 6 wt%, toluene 90 wt%, benzoin 0.1 wt%, UV 312 nm for 10 min. Photografting: META 20wt%, tertbutyl alcohol 60 wt%, water 20 wt%, benzonphenone 0.2 wt%, UV 254 nm. The polymerization was conducted in 10-μm internal diameter silica -fused capillaries. The measurements were performed at room temperature with 20 mM phosphate buffer (pH7.0).

4.3.3.1 The Dependence of EOF on Buffer pH Value

The unmodified glass surface is negatively charged at most pH values and exhibits considerable cathodic EOF, which is significantly influenced by the pH, due to the protonation or deprotonation of silanol sites on the glass surface. The EOF mobility in an uncoated glass microchannel increased markedly with the pH in the range of 3-10, as seen in Figure 4.6 A (curve a). In contrast, a channel coated with a neutral HEMA polymer film is almost unaffected over this pH range, as shown in Figure 4.6 A (curve b). A cation-coated channel produced obviously reversed EOF over the same pH range, as seen in Figure 4.6 A (curve c). Photografted cationic META, bearing a quaternary ammonium group, creates positively charged groups on the surface at all pH values. The rate of EOF at pH 3 was up to 4×10^{-4} cm^2 V^{-1} s^{-1}. Perhaps surprisingly, a variation of the flow velocity is observed as a function of the pH. An increase in pH results in a decrease in EOF, this decrease continues up to pH 10, where the flow remains in a reversed direction with a magnitude of 10^{-4} cm^2 V^{-1} s^{-1}. This decrease may be due to increasing ionic strength of the buffer at higher pH.

4.3.3.2 Long-term Stability of EOF

The stability of the EOF during repetitive runs is a crucial parameter, and is a direct function of the performance of the coating. In order to evaluate the performance of the coating generated here, the stability of the EOF in a META-coated glass microchannel was investigated for 15 days, with continuous operation for 3 h per day. The measurements were performed at room temperature by using 18 mM and 20 mM phosphate buffer (pH 7.0) and the current-monitoring method. The results shown in

Figure 4.6 B illustrate a fairly stable reversed EOF during the investigation, which indicates a successful coating. We found adding 5% acetonitrile into the buffer solution could improve the repetitive measurements. The average values of reversed EOF measured from the first-day and the last-day are $1.76 \pm 0.04 \times 10^{-4}$ cm^2 V^{-1} s^{-1} (n=16) and $1.69 \pm 0.05 \times 10^{-4}$ cm^2 V^{-1} s^{-1} (n=16), individually. The average value of reversed EOF for a total of half-month measurements is 1.72×10^{-4} cm^2 V^{-1} s^{-1} (RSD=2.6%, n=64).

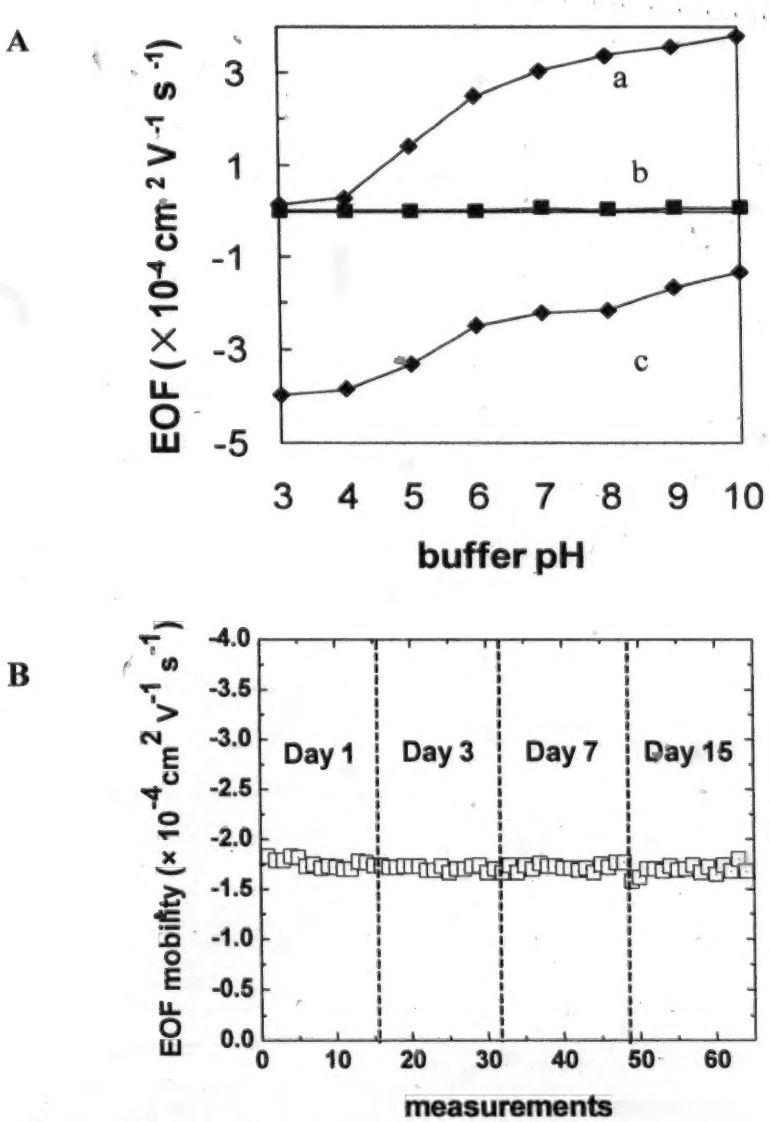

Figure 4.6 A: EOF measured within glass microchannel responsed to the different buffer pH illustrating the surface coverage effect of the total coating process. Curves: (a) Activated glass microchannel, (b) Neutral HEMA-coated glass microchannel, (c) Cationic META photografted glass microchannel. The polymerization conditions were indicated in figure 4.3 C. **B**: The reproducibility of EOF produced by cationic META coating. The measurements were performed at room temperature with 20 mM phosphate buffer (pH7.0). Glass microchannel is ~24-μm wide and ~7-μm deep.

4.3.4 Injection Geometry Optimization for Separation

The injection system on a microfluidic chip is one of the key elements in the sample handling process, and its characteristics determine the efficiency and quality of the separation. The loading of sample ions within electrokinetically controlled microfluidic devices is determined by electrophoretic mobility and by electroosmotic forces. We evaluated the injection quality in devices coated with neutral, hydrophilic HEMA polymer. The polymerization conditions were the same as indicated in Figure 4.3, without photografting of META. EOF was substantially suppressed and the movement of sample ions depended only on the electrophoretic mobility. In order to effectively control the sample plug geometry, a "full shaping" method was used to effectively pinch the plug at both the top and bottom of the injector, and was expected to produce unbiased, reproducible injection plugs [36]. Figure 4.7 shows the fluorescent images for the sample loading process. Trypsin inhibitor and BSA were chosen as model proteins. Shaped, narrow sample plugs were achieved in both the double-T injector and the cross injector, as shown in Figure 4.7 A and B. The sample plug in the injector intersection was focused by the buffer streams from the separation channel. Full plug shaping in the double-T injector is analogous to "pinching" in the cross injector, shown in Figure 4.7 B for injection of BSA in a cross injector. Such a narrow sample band contributes to the high separation efficiency.

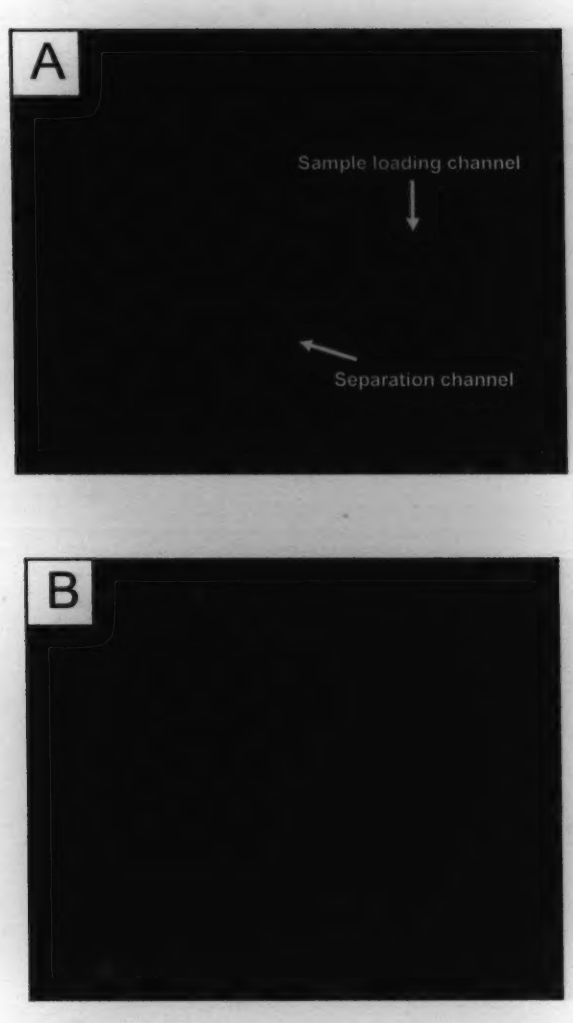

Figure 4.7 Fluorescent images for pinched protein injection in HEMA polymer coated microchips. Protein concentration is 50 μM in 20 mM phosphate buffer (pH 9.0). **A:** Trypsin inhibitor injected in a 10-μm off double-T injector with 1000 V injection voltage. Other three reservoirs are grounded. **B**: BSA injected in a cross injector with 1000 V injection voltage. Other three reservoirs are grounded.

The reproducibility of the injection process was investigated, as shown in Figure 4.8. BSA, IgG and trypsin inhibitor were injected individually, with different loading times. The migration time and peak shape were quite repeatable for different loading times from 10 s, 20 s to 30 s. This indicates that the sample plug is well shaped and that an optimized injection process is reliable and reproducible, which is good for achieving high separation efficiency. Multiple peaks in Figure 4.8 arose from sample preparation caused protein aggregation and degradation. Therefore native protein samples should be carefully kept in 4°C and the sample in reservoir needs to be refreshed frequently. Improved protein samples were shown in Figure 4.10 and 4.11 with pure single peak.

Differences in conductivity between the sample and running buffer can result in sample stacking or electromigration dispersion, which will change peak shapes and heights. Here, we always used the running buffer to prepare the sample. In addition, changes in composition can consequently affect the migration velocity and peak areas. This effect can be corrected for by dividing peak area by migration time to obtain a quantity proportioned to the amount injected, as shown in Figure 4.9. The amounts injected as a function of injection time for geometrically defined injections were investigated. The peak areas of trypsin inhibitor, BSA and IgG increased initially with injection time, and eventually reached a plateau. All sample amounts achieved a plateau after a given injection time. This suggests that the injections are indeed geometrically defined. The faster moving trypsin inhibitor required about 7 s to reach steady state, and BSA required about 10 s, while IgG required about 15 s. This migration order is consistent with the order of magnitudes of the mobilities themselves.

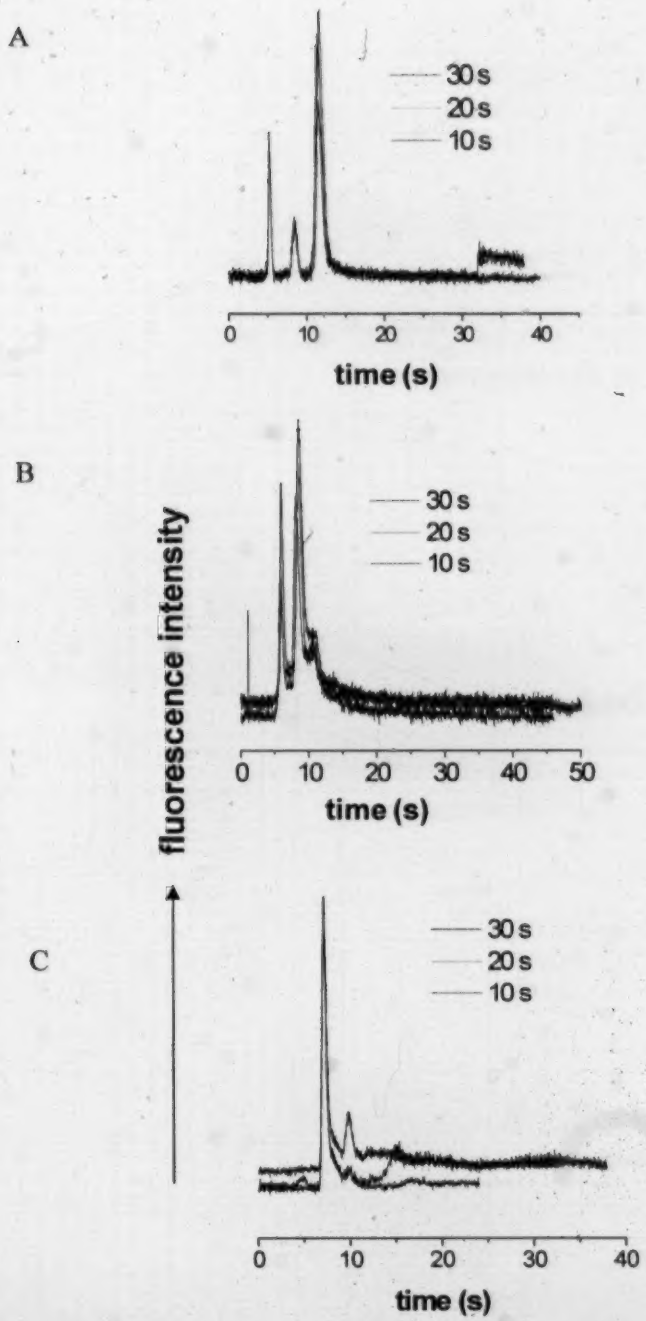

Figure 4.8 Electropherograms of proteins with different injection times. **A**: BSA; **B**: IgG; **C**: Trypsin inhibitor. Proteins in 20 mM phosphate buffer (pH 9.0) were injected in a cross injector coated with HEMA polymer layer and the injection voltage is 1000 V.

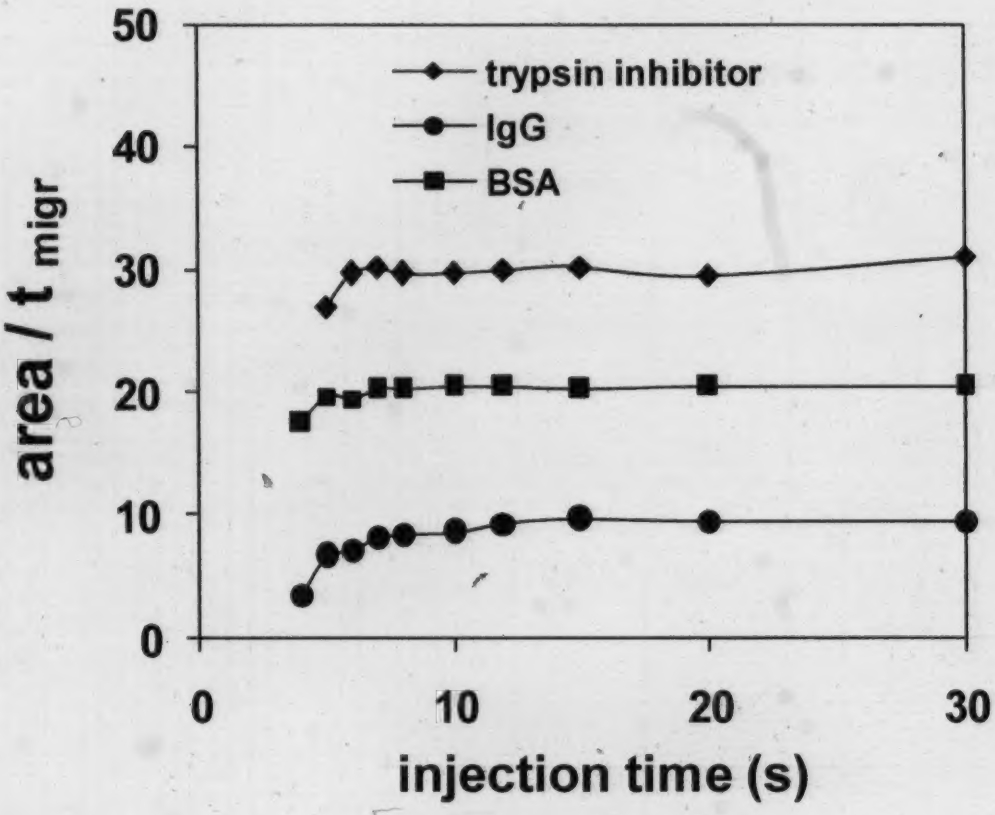

Figure 4.9 Plot of peak area/t_{migr} versus length of sample loading time for proteins in 20 mM phosphate buffer, pH 9.0. Electrophoretic conditions are the same as Figure 4.8.

4.3.5 Protein Separation Performance

The nonspecific adsorption of proteins on surfaces is a crucial problem, with a need to minimize adsorption in order to improve the resolution of electrokinetic separations. In the case of blood serum proteins, albumin adsorption is a major problem [2]. For example, the electrophoretic separation of BSA in free solution usually shows tailing of the peak, a loss of efficiency, as well as a lack of reproducibility. For this reason, BSA was chosen as a model protein, along with the trypsin inhibitor. These proteins are negatively charged at pH 9.0, requiring a positive voltage for electrophoresis. The separation efficiency and resolution were evaluated at different separation lengths with HEMA coating, as shown in Figure 4.10. The separation resolution for these two proteins is 3.91 at a 0.5-cm separation length, increasing to 7.75 with better efficiency at a 1-cm length.

Separations of native BSA and trypsin inhibitor in 20-mM phosphate running buffer were repeated consecutively 20 times. Repetitive electropherograms are shown in Figure 4.11. Peak migration times for the two components were not much different between the first five and last five runs, as shown in Table 4.3. The RSD value of migration times for the consecutive runs was less than 3%. The results indicate the coating was quite effective in reducing protein adsorption. The separation efficiency and reproducibility from this confinement coating strategy are comparable with literature [20, 25, 30].

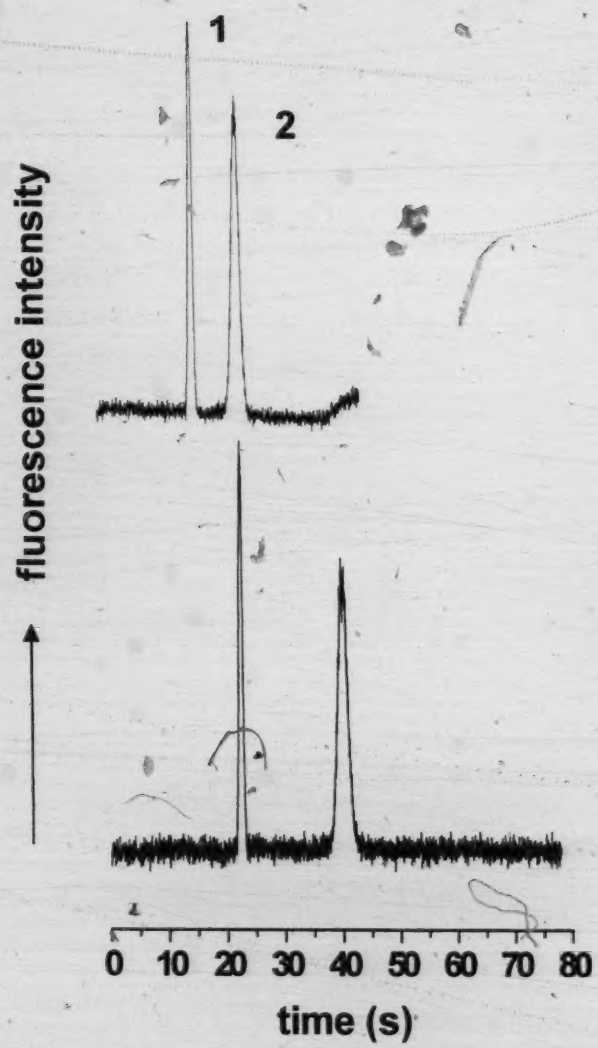

peak	N/m	Rs
1	6.6×10^5	3.91
2	3.7×10^5	

Separation length: 0.5 cm
Voltage: 300 V/ cm

peak	N/m	Rs
1	7.6×10^5	7.75
2	3.2×10^5	

Separation length: 1.0 cm
Voltage: 300 V/ cm

Figure 4.10 Electropherograms for protein separation under the influence of the separation length. The first peak is trypsin inhibitor and the second peak is BSA. The HEMA polymerization condition is the same as given for Figure 4.3, without photografting of META. Proteins were mixed in 20 mM Phosphate buffer (pH 9.0). Injection time is 10 s.

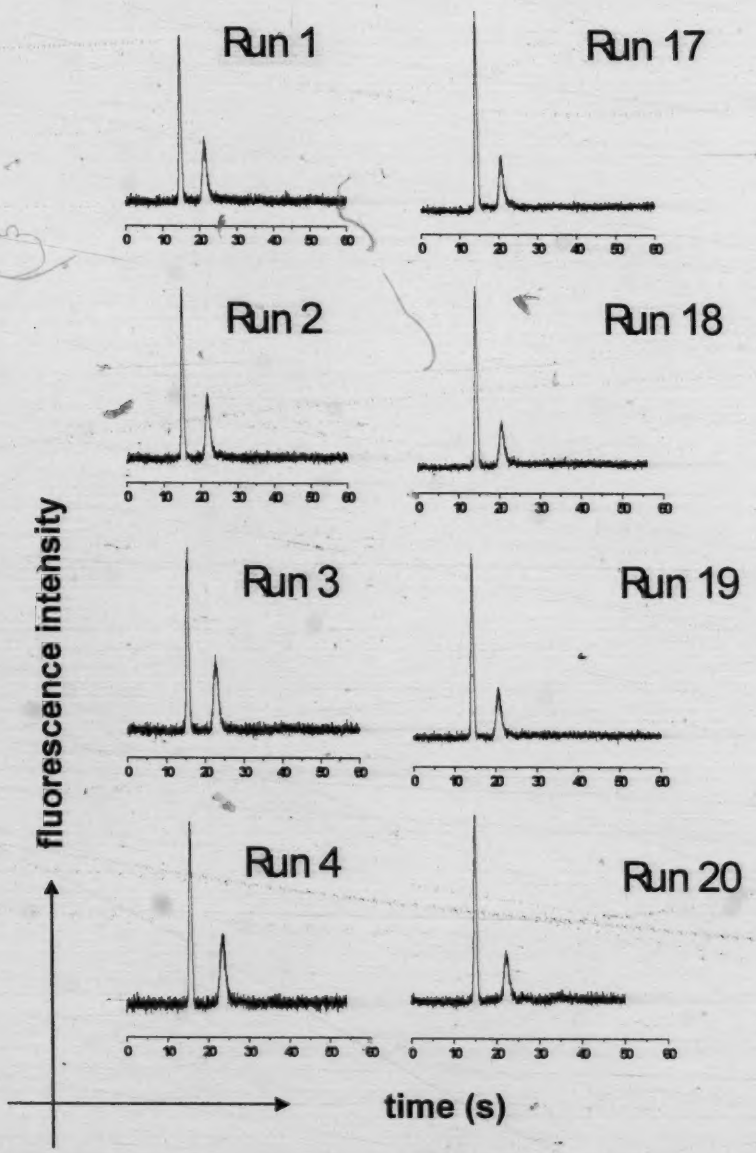

Figure 4.11 Electropherograms of 20 repetitive runs for model protein separation. Microchannel was coated with neutral hydrophilic HEMA polymer film. The first peak is trypsin inhibitor and the second peak is BSA. Polymerization condition is the same as given for Figure 4.3, without photografting of META. Proteins were mixed in 20 mM Phosphate buffer (pH 9.0). Injection time is 10 s and the separation voltage is 300 V/cm. The separation length is 0.5 cm.

The long-term reproducibility of a coating is usually improved by rinsing. Sodium hydroxide solution (0.1 M) with 50% methanol was used in our conditioning procedure. In addition, the protein sample was refreshed every five runs to avoid thermal or electrolysis-induced degradation.

The day-to-day reproducibility of the columns for separation was investigated, as seen in Figure 4.12 and analyzed in Table 4.3. The separations were conducted continuously for 3 hours per day at voltage of 300 V/cm. The RSD values of the migration time of proteins over three days were less than 4%. This indicates that protein separation and analysis using this polymer coating is quite stable and reproducible.

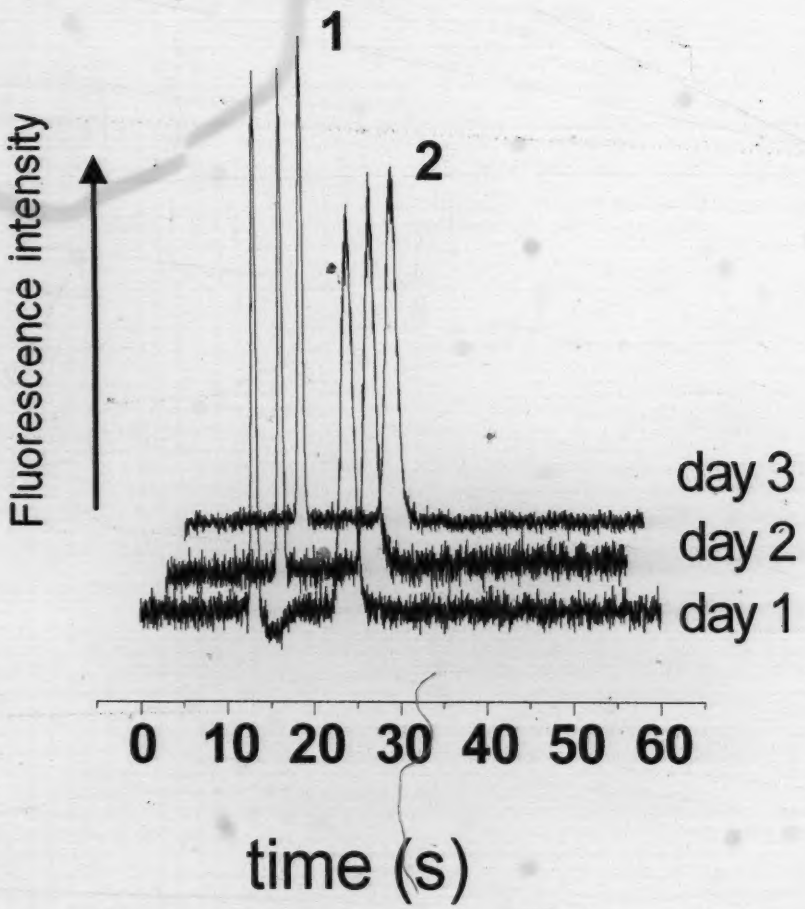

Figure 4.12 Day-to-day reproducibility of migration time of proteins in neutral HEMA-coated microchannel. Conditions are the same as given in Figure 4.11. Peak 1: trypsin inhibitor. Peak 2: BSA.

The prevention of positively charged protein adsorption during separation has proved to be especially challenging. The applicability of a neutral, hydrophilic HEMA/EDMA coating for the separation of positively charged proteins was investigated. Separation of two native proteins, trypsin inhibitor and carbonic anhydrase, positively charged in 20-mM phosphate running buffer, pH 3, was repeated 20 times consecutively within the coated channels, without rinsing. Two separated peaks were detected each run, with a separation efficiency of ~ 2×10^6 theoretical plates per meter, as shown in Figure 4.13. Peak migration times (and widths) were 29.6 ± 0.3 s and 35.8 ± 0.3 s (0.98 ± 0.01 and 0.88 ± 0.02 intensity-s) for the two components, with no statistical difference (95 % confidence) between the first five and last five runs, as listed in Table 4.4. Runs in uncoated chips gave broad, poorly reproducible peaks that degraded rapidly with each run. This separation efficiency is higher compared to BSA, which may imply less adsorption of trypsin inhibitor and carbonic anhydrase on the wall.

Three native proteins, trypsin inhibitor, ovalbumin and BSA were separated within a 1-cm long microchannel, as shown in Figure 4.14. BSA and ovalbumin are the classic proteins that readily adsorb on the surface, due to strong hydrophobic properties. Peak 2 and 3 in Figure 4.4 are for those two proteins, have an almost symmetrical profile without tailing, indicating little interaction with the HEMA/EDMA polymer coating. The resolution for these two proteins is 2.1 and efficiencies are in the range of 4×10^5 N/m. This efficiency is comparable with literature (~5×10^5 N/m) [27, 30]. Four consecutive runs showed good reproducibility of migration time with an RSD less than 3%.

Table 4.4 Separation efficiency, migration time, and relative standard deviation for protein separation with 20 consecutive runs and day-to-day runs. The data was calculated from Figure 4.11 and Figure 4.12 within one device.

Protein	N/m ($\times 10^5$)	t /s	RSD	t /s			
				day 1	day 2	day 3	RSD(n=15)
Trypsin inhibitor				12.7	12.9	13.4	2.7%
Runs 1-5	5.7	15.3	2.5%				
Runs 16-20	6.7	15.5	1.7%				
BSA				22.3	23.3	24.1	3.8%
Runs 1-5	3.6	22.9	1.3%				
Runs 16-20	3.3	22.7	2.5%				

Table 4.5 Separation efficiency, migration time, half peak width and relative standard deviation for protein separation with 20 consecutive runs. The data was calculated from Figure 4.13 within one device.

Peak	Protein	N/m	t /s	RSD	W_h/s	RSD
1	Carbonic anhydrase					
	Runs 1-5	1.1×10^6	30.2	1.0%	1.0	4.2%
	Runs 16-20	1.0×10^6	29.7	1.1%	1.0	2.7%
2	Trypsin inhibitor					
	Runs 1-5	1.8×10^6	36.2	1.2%	0.9	3.5%
	Runs 16-20	1.9×10^6	36.4	0.8%	0.8	4.6%

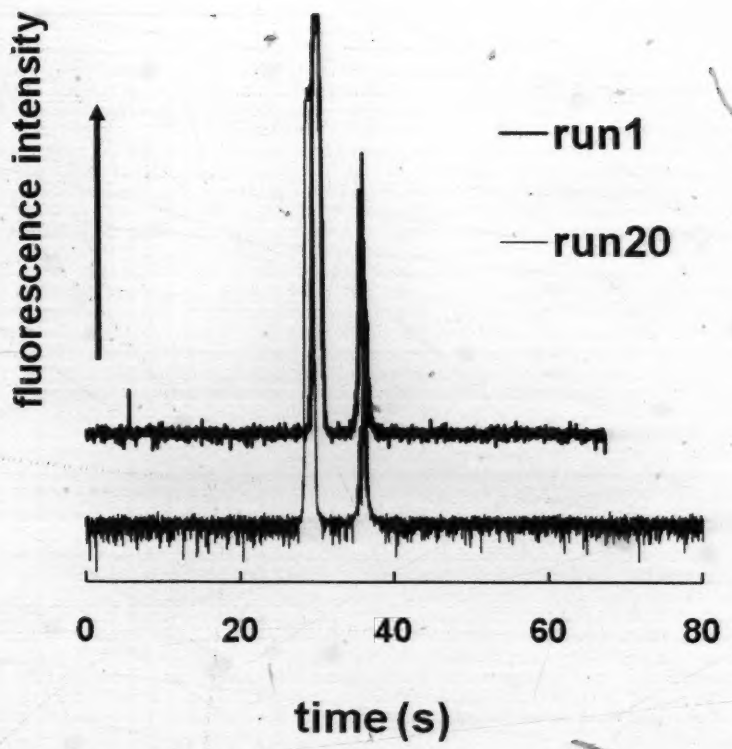

Figure 4.13 Electropherograms of 20 repetitive runs for protein separation based on neutral hydrophilic surface coating (HEMA) used for prevention of non-specific adsorption; the first peak is carbonic anhydrase and the second peak is trypsin inhibitor. Two runs are shown, offset on the y-axis for clarity. The HEMA polymerization condition is the same as given for Figure 4.3, without photografting of META. Proteins were mixed in 20 mM phosphate buffer (pH 3.0). Injection time is 8 s and the separation voltage is 150 V/cm. The separation length is 0.5 cm.

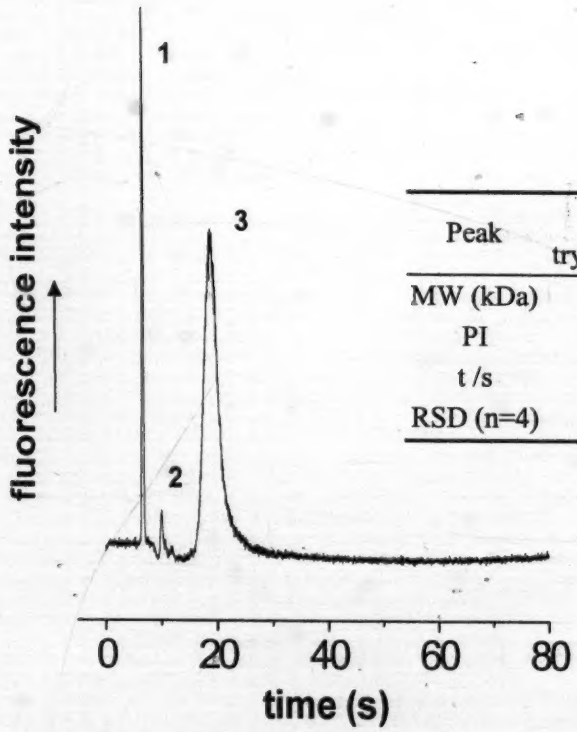

Peak	1 trypsin inhibitor	2 ovalbumin	3 BSA
MW (kDa)	21	45	66
PI	4.5	4.6	4.9
t /s	6.6	9.9	18.9
RSD (n=4)	1.5%	2.2%	3.1%

Figure 4.14 Electropherogram for three model proteins separated within a HEMA polymer coated glass microchannel; the first peak is trypsin inhibitor, the second is ovalbumin and third is BSA. Proteins were mixed in 20 mM Phosphate buffer (pH 9.0). Injection time is 10 s and the separation voltage is 400 V/cm. The separation length is 1 cm.

4.3.6 Separation of Enzymatic Digest Mixtures

FITC-conjugated BSA was digested by chymotrypsin. Separations of the digests were conducted using a μCE chip coated with a neutral HEMA polymer layer, using the protocol discussed above. As presented in Figure 4.15A, the separation was completed in 15 seconds in a 1-cm channel length, with a total of 9 peaks resolved, illustrating the high efficiency and rapid separation performance. The calculated theoretical plate number is ~

4×10^5 N/m and the plate height is ~2.5 μm. This result demonstrates the applicability of this surface coating method in peptide digest analysis, an important area of proteomics research.

The separation of a complex mixture could be improved by immobilization of functional groups on the coating surface for increased resolving ability. SBMA, which contains both cationic and anionic groups on the same monomer residue, has been proved to be a nonfouling material with good biocompatibility [37-40]. It has been reported that SBMA can be immobilized on glass and silica surfaces through atom transfer radical polymerization [41]. Here, we demonstrated modification of the polymer film coating in the microchannels, by photografting SBMA through a photo-initiated free radical polymerization. The acrylate group of the SBMA is involved in the radical polymerization, forming a covalent bond to link this zwitterionic functional group to the surface of the hydrophilic HEMA coating, as illustrated in the Figure 4.15 B. In order to keep the same injection strategy, only the separation channel was selectively modified by SBMA, using a photomask. Separation of FITC-conjugated BSA digests is shown in Figure 4.15B, with 15 peaks observed within 25 seconds and a 1-cm separation length. Compared with the result in Figure 4.15A using unmodified HEMA coating, photografting SBMA gives longer retention time and more observed peaks under the same electrophoretic conditions, which suggests better separation ability. The two oppositely charged functional groups of SBMA and the hydrophilic property of HEMA both contribute to analyte retention, which may be due to simultaneous electrostatic attraction and repulsion of analyte ions [42-46]. Jiang *et al.* covalently bonded SBMA on the surface of silica-fused capillary and proved this modification has improved separation

for model proteins, with an efficiency 4.3×10^5 N/m [47, 48]. Our results are comparable with that literature and have demonstrated the feasibility for versatile functionalities. The multifunctional feasibility of photografted coating allows one to extend resolving power for mixture separation. This coating strategy reduced nonspecific adsorption on separation devices, and allowed a higher chromatographic resolving power.

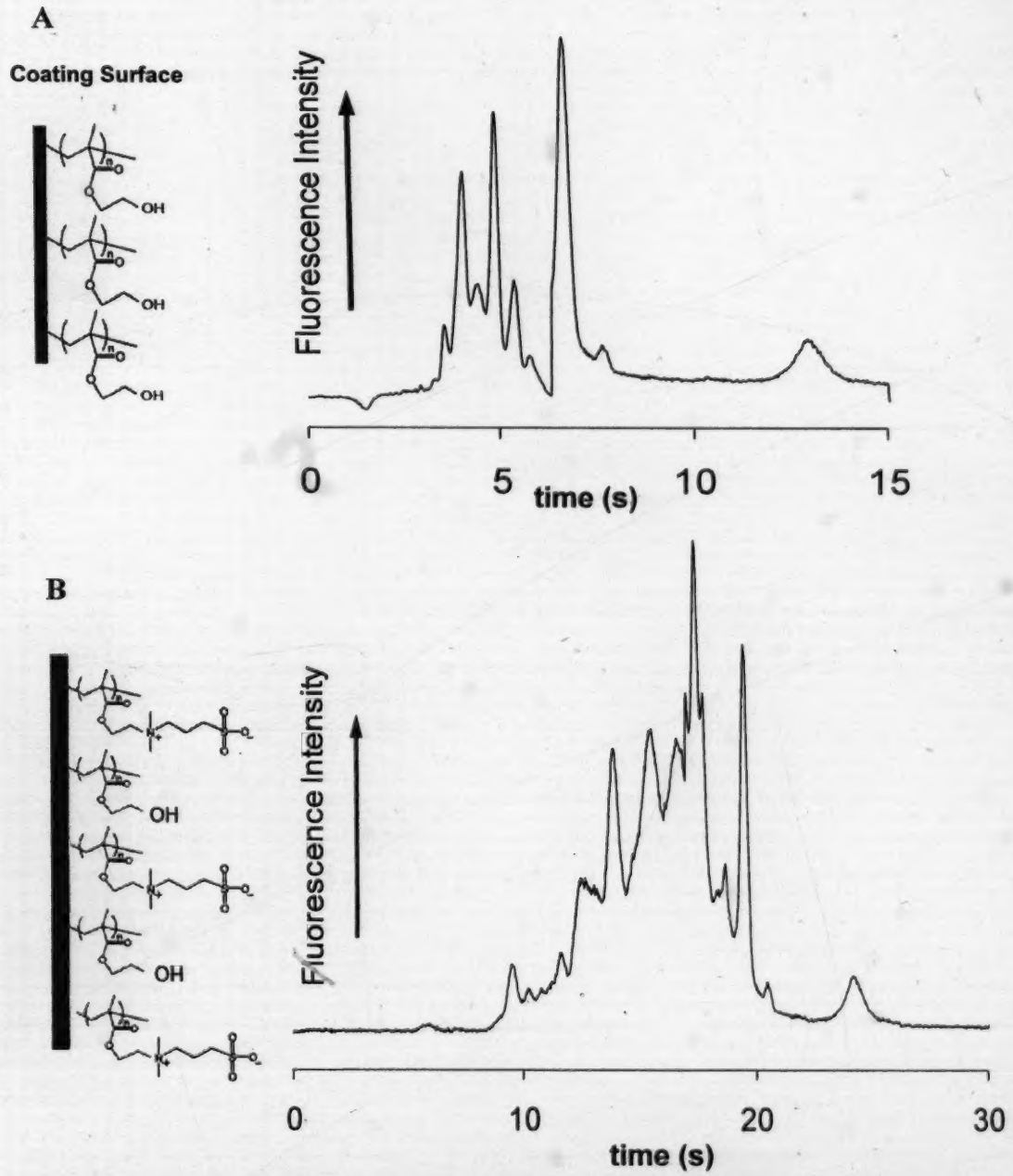

Figure 4.15 Electropherograms for separation of FITC-conjugated BSA digests whthin glass channel coated with (**A**) HEMA polymer layer and (**B**) HEMA polymer layer with SBMA photografting. Conditions: 20 mM Phosphate buffer (pH 9.5). Injection time is 10 s and the separation voltage is 700 V/cm. The separation length is 1 cm. The HEMA layer polymerization condition is the same as given for Figure 4.3. Photografting: SBMA 5 wt%, water 35 wt%, 1,4-butanediol 60 wt%, 4-(dimethylamino) benzonphenone 0.2 wt%, UV 312 nm for 150 s.

4.4 CONCLUSIONS

Extreme deformation of a polymer monolith under confinement was employed to obtain uniform surface coatings with a tunable thickness from ~100 to ~700 nm. Photo-initiated polymerization enables the coating to be localized in the desired portion of the microfluidic device, and the surface chemistry can be tailored to fit the specific application. The results establish that this thick film coating can be readily prepared in a short time and with little complication using the confinement effect. Appropriate surface films show good efficiency for protein separations. In both acidic and basic buffers, the protein separations showed high efficiency and good reproducibility, and the EOF could be controlled by the choice of surface functionalities. Meanwhile, photopatternable grafting was demonstrated by immobilizing specific functional groups for fast separation of proteolysis digest. This coating method proved to be capable of multifunctionality and improved resolving power. Our results provide a novel coating strategy to create robust, thick wall coatings for applications such as surface chemistry control, surface biocompatibility, capillary electrophoresis and open tubular chromatography.

4.5 REFERENCES

1 Dolník, V. *Electrohphoresis* **2004**, *25*, 3589-3601.

2 Peng, Y. Y.; Pallandre, A.; Tran, N. T.; Myriam, T. *Electrophoresis* **2008**, *29*, 157-178.

3 Doherty, E. A. S.; Meagher, R. J.; Albarghouthi, M. N.; Barron, A. E. *Electrohphoresis* **2003**, *24*, 34-54.

4 Belder, D.; Ludwig, M. *Electrohphoresis* **2003**, *24*, 3595-3606.

5 Lu, J. J.; Liu, S. *Electrohphoresis* **2006**, *27*, 3764-3771.

6 Xu, Y.; Takai, M., Konno, T., Ishihara, K. *Lab Chip* **2007**, *7*, 199-206.

7 Liu, S. R.; Ren, H. J.; Gao, Q. F.; Roach, D. J.; Loder, R. T.; Armstrong, T. M.; Mao, Q. L.; Blaga, D. L.; Jovanovich, S. B. *Proc. Natl. Acad. Sci. U.S.A.* **2000**, *97*, 5369-5374.

8 Munro, N. J.; Hühmer, A. F. R.; Landers, J. P. *Anal. Chem.* **2001**, *73*, 1784-1794.

9 Hu, S.; Ren, X.; Bachman, M.; Sims, C. E.; Li, G. P.; Allbritton, N. L. *Anal. Chem.* **2004**, *76*, 1865-1870.

10 Abate, A. R.; Lee, D.; Do, T.; Holtze, C.; Weitz, D. A. *Lab Chip* **2008**, *8*, 516-518.

11 Wang, A. J.; Xu, J. J.; Chen H. Y. *J. Chromatogr. A* **2007**, *1147*, 120-126.

12 Sibarani J.; Takai M.; Ishihara, K. *Colloids Surf., B* **2007**, *54*, 88-93.

13 Xu, Y.; Jiang, H.; Wang, E. *Electrophoresis* **2007**, *28*, 4597-4605.

14 Rohr, T.; Ogletree, F. D.; Svec, F.; Fréchet, J. M. J. *Adv. Funct. Mater.* **2003**, *13*, 264-270.

15 Horvath, J.; Dolník, V. *Electrohphoresis* **2001**, *22*, 644-655.

16 Liu, J.; Lee, M. L. *Electrohphoresis* **2006**, *27*, 3533-3546.

17 Li, C.; Yang Y.; Craighead, H. G.; Lee, K. H. *Electrohphoresis* **2005**, *26*, 1800-1806.

18 Barker, S. L.R.; Tarlov, M. J.; Canavan, H.; Hickman, J. J.; Locascio. L. E. *Anal. Chem.* **2000**, *72*, 4899-4903.

19 Henry, A. C.; Waddell, E. A.; Shreiner, R.; Locascio. L. E. *Electrohphoresis* **2002**, *23*, 791-798.

20 Diress, A. G.; Lucy, C. A. *Can. J. Chem.* **2007**, *85*, 540-546.

21 Razunguzwa, T. T.; Warrier, M.; Timperman, A. T. *Anal. Chem.* **2006**, *78*, 4326-4333.

22 Finkler, C.; Charrel, H.; Engelhardt, H. *J. Chromatogr. A* **1998**, *822*, 120-126.

23 Wootton, R. C. R.; Demello, A. J. *Lab Chip* **2006**, *6*, 471-473.

24 Eeltink, S.; Svec, F. *Electrohphoresis* **2007**, *28*, 137-147.

25 Leinweber, F. C.; Stein, J.; Otto, M. *Fresenius J. Anal. Chem.* **2001**, *370*, 781–788.

26 Hjertén, S. *J. Chromatogr.* **1985**, *347*, 191-196.

27 Huang, X.; Horváth, C. *J. Chromatogr. A* **1997**, *788*, 155-164.

28 Tan, Z. J.; Remcho, V. T. *J. Microcol. Sep.* **1998**, *10*, 99-105.

29 Eeltink, S.; Svec, F.; Fréchet, J. M. J. *Electrophoresis* **2006**, *27*, 4249-4256.

30 Huang, X. Y.; Doneski, L. J.; Wirth, M. J. *Anal. Chem.* **1998**, *70*, 4023-4029.

31 Xu, L.; Sun, Y. *J. Chromatogr. A* **2008**, *1183*, 129-134.

32 He, M.; Zeng Y.; Sun, X.; Harrison, D.J. *Electrophoresis* **2008**, *29*, 2980-2986.

33 He, M.; Zeng Y.; Harrison, D.J. *Proc. μ-TAS 2007*, Paris, **2007**, 805-807.

34 Stachowiak, T. B.; Svec, F.; Fréchet, J. M. J. *Chem. Mater.* **2006**, *18*, 5950-5957.

35 Huang, X. H.; Gordon, M. J.; Zare, R. N. *Anal. Chem.* **1998**, *60*, 1837-1840.

36 Shultz-Lockyear, L. L.; Colyer, C. L.; Fan, Z. H.; Roy, K. I.; Harrison, D. J. *Electrophoresis* **1999**, *20*, 529-538.

37 Chen, S.; Zheng, L.; Li, L; Jiang, S. *J. Am. Chem. Soc.* **2005**, *127*, 14473-14478.

38 Chen, S.; Yu, F. C.; Yu, Q.; He, Y.; Jiang, S. *Langmuir* **2006**, *22*, 8186-8191.

39 Li, L.; Chen, S.; Zheng, J.; Ratner, B. D.; Jiang, S. *J. Phys. Chem. B* **2005**, *109*, 2934-2941.

40 Zhang, Z.; Chao, T.; Chen, S.; Jiang, S. *Langmuir* **2006**, *22*, 10072-10077.

41 Zhang, Z.; Chen, S; Chang, Y.; Jiang, S. *J. Phys. Chem. B* **2006**, *110*, 10799-10804.

42 Vikingsson, S.; Kronstrand, R.; Josefsson, M. *J. Chromatogr. A* **2008**, *1187*, 46-52.

43 Cook, H. A.; Dicinoski, G. W.; Haddad, P. R. *J. Chromatogr. A* **2003**, *997*, 13-20.

44 Cook, H. A.; Hu, W.; Fritz, J. S.; Haddad, P. R. *Anal. Chem.* **2001**. *73*, 3022-3027.

45 Lucy, C. A.; Macdonald, A. M.; Gulcev, M. D. *J. Chromatogr. A* **2008**, *1184*, 81-105.

46 Boersema, P. J.; Divecha, N.; Heck, A. J. R.; Mohammed, S. *J. Proteome Res.* **2007**, *6*, 937-946

47 Jiang, W. *Umeå University Thesis*, Sweden, **2003**.

48 Jiang, W.; Awasum, J. N.; Irgum, K. *Anal. Chem.* **2003**. *75*, 2678-2774.

Chapter 5

Polymer Monoliths Photopatterned within Microfluidic Devices as Enzymatic Microreactors

5.1 INTRODUCTION

Miniaturized and integrated microfluidic devices are of great interest in the fields of analytical and biology chemistry, offering the possibility of easier easy sample handling, decreased sample loss and contamination, and the opportunity for fast, automated analysis [1-5]. It is possible to integrate various functional components within one microfluidic device to perform multiple preparation steps with complex protein samples, such as desalting, purification, concentration, and enzymatic digestion. Such capability is especially valuable for proteomics, which represents the next major target in the postgenomic era [6-10]. Peptide-mass mapping is one of the routine methods that is commonly used to determine both protein identity and posttranslational modifications [11]. These methods typically involve the digestion of the protein of interest by a proteolytic enzyme, e.g. trypsin, in free solution, followed by MS identification of the resulting peptides. Based on an understanding of the cleavage processes, this approach offers a peptide map that is unique for each protein, allowing its identification with existing databases [12-15]. However, for the most commonly used free-solution protein digestion, the reaction time employed is typically 24 hours, since the trypsin-to-substrate ratio has to be kept very low (1:50) to avoid excessive autodigestion of trypsin and the

resulting formation of additional peptide fragments [16,17]. Such unwanted autodigestion can be eliminated by site isolation of the enzyme moieties, realized by immobilization of enzyme molecules on the surface of a solid support [18]. The ideal solid support for immobilization should have particular characteristics, such as a large surface area, permeability, hydrophilic character, insolubility, chemical, mechanical and thermal stability, high rigidity and chemical reactivity for coupling of the ligands and resistance to enzymatic attack [19]. Several types of supports, including magnetic beads and monolithic chromatographic supports, are commercially available [20].

Enzyme decorated beads remain seldom used in microfluidic devices due to the difficulty of packing in the microchannels [21]. In contrast, porous polymer monoliths are much easier to introduce into microchannels with *in-situ* photo-patternable methods [22]. Photopatterning offers an attractive means for the integration of multiplex components for microfluidic proteomics. The Fréchet research group reported an enzymatic microreactor fabricated in microfluidic device by immobilizing trypsin on porous polymer monoliths consisting of the monomer 2-vinyl-4,4-dimethylazlactone, EDMA [23, 24]. The performance of the enzyme microreactor was characterized and the peptide fragments were identified with a sequence coverage of 67% in a 11.7 s residence time [25]. The Massonili group immobilized chymotrypsin on a polymer monolith through an epoxy group, and used it for HSA digestion with online coupling to an LC-ESI-MS. A complete protein digestion and analysis in 120 min was achieved with a sequence coverage of 97.3% [26].

In order to incorporate multiplexed monolith-based microreactors into complex microfluidic devices, tight control of structural properties, fluidic stability, and the

enzymatic reaction performance of the polymer beds is particularly important. This chapter systematically investigates the conditions for patterning of photopolymerized monoliths within microscale channels, which include the resolution of photopatterning, surface chemistry selection, pore structure control and porogenic solvent selection. The conditions were optimized to establish a fast and easy protocol for enzymatic microreactor applications. The performance of trypsin immobilization on monolithic bed was also examined and the digestion efficiency in these patterned microreactors with stable flow resistance was evaluated.

5.2 MATERIALS AND METHODS

5.2.1 Reagents and Samples

Benzoin, 1-octanol, ammonium acetate, cytochrome C from horse heart (M.W. = 12,384 g/mol), TPCK trypsin from bovine pancreas, benzamidine, NaCl, aspartic acid, HEMA, EDMA, GMA, BMA and 3-(trimethoxysilyl)propyl methacrylate were purchased from Aldrich (Milwaukee, WI, USA). All aqueous solutions were made in ultrapure water (Millipore) and filtered before use (0.2 μm, Chromatographic Specialties). Chip fabrication and photopolymerization procedures were described in Chapter 2.

5.2.2 Trypsin Immobilization Procedure

The monolith was formed by photopolymerization following the recipe listed in Table 5.1. The mechanism of immobilization is illustrated in Figure 5.1 [16].

Table 5.1 The recipe for the photopolymerization of microreactor.

70%	21%	9%	0.3%	Reaction time
EDMA	1-octanol	HEMA+GMA	Benzoin	9 min

The monolith was pre-washed with 50 mM carbonate buffer, pH 10.5, for 10 min. A solution of TPCK treated trypsin (4 mg/ml) dissolved in carbonate buffer with benzamidine 0.2 mg/mL, was flowed through the monolith at 100 nl/min for 8 h. The nonspecific enzyme absorbant was eluted by flushing with 50 mM carbonate buffer containing 1 M NaCl for 1 h. Finally, the non-reacted epoxy group was blocked by flushing with 50 mM sodium carbonate buffer containing 1 mg/mL aspartic acid for 1 h.

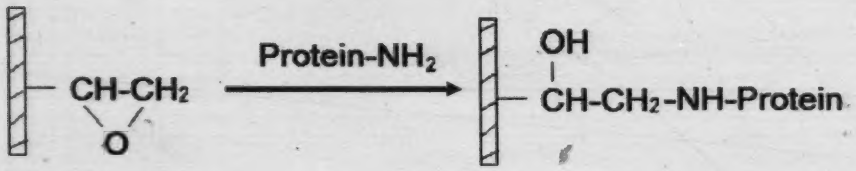

Figure 5.1 The scheme of immobilization procedure for covalent attachment of enzyme *via* epoxy group.

5.2.3 Mass Spectrometry Conditions

Cytochrome C from horse heart (Sigma-Aldrich, M.W. = 12,384 g/mol) was prepared in 10 mM ammonium acetate buffer (20% v/v methanol), pH 6.7. The trypsin bed was 7-mm long. A 0.05 mg/ml Cytochrome C solution was introduced into the microchannel by syringe pump (PHD2000, Harvard apparatus, USA) at a flow rate of 0.021 µl/min to give a 180 s residence time on the trypsin bed, or a flow rate of 0.063 µl/min for a 60 s residence time. Then effluent was collected at the outlet, followed by MALDI-TOF MS (Voyager ™ Biospectrometry ™ Workstation, Applied Biosystem,

USA) analysis. HCCA was used as a matrix. On-spot washing of the MALDI sample with water was performed to remove any salts. The sample spot was scanned with a 337 nm nitrogen laser beam under video observation and the MS was operated in positive ion mode.

5.3 RESULTS AND DISCUSSION

5.3.1 Photoinitiator

A photoinitiator undergoes a photoreaction upon absorption of light and produces a reactive species. The reactive species initiate chemical reactions, which result in significant changes in the solubility and physical properties of suitable formulations. Commonly used photoinitiators include azobisisobutyronitrile (AIBN), benzoin methyl ether (BME) and its derivatives. The UV absorption profiles for typical photoinitiators are shown in Figure 5.2. It is recommended to choose the maximum absorption wavelength of the photoinitiator to induce polymerization, because this gives the highest efficiency for producing the reactive initiator. This wavelength is usually ~250 nm. However, we use 0211 glass to fabricate the microchip. The UV light transmittance for 0.6-mm thick 0211 glass is ~0% around 250 nm and over 70% above 300 nm. Therefore, we chose 312 nm as the exposure wavelength. Benzoin was selected as the photoinitiator, because it is inexpensive and a better photoinitiator than AIBN. Benzoin absorbs UV light and undergoes homo-cleavage to form a free radical, initiating chain polymerization. Benzophenone and 4-(dimethylamino)-benzophenone undergo different decomposition mechanism by hydrogen abstraction, which is more suitable for photografting.

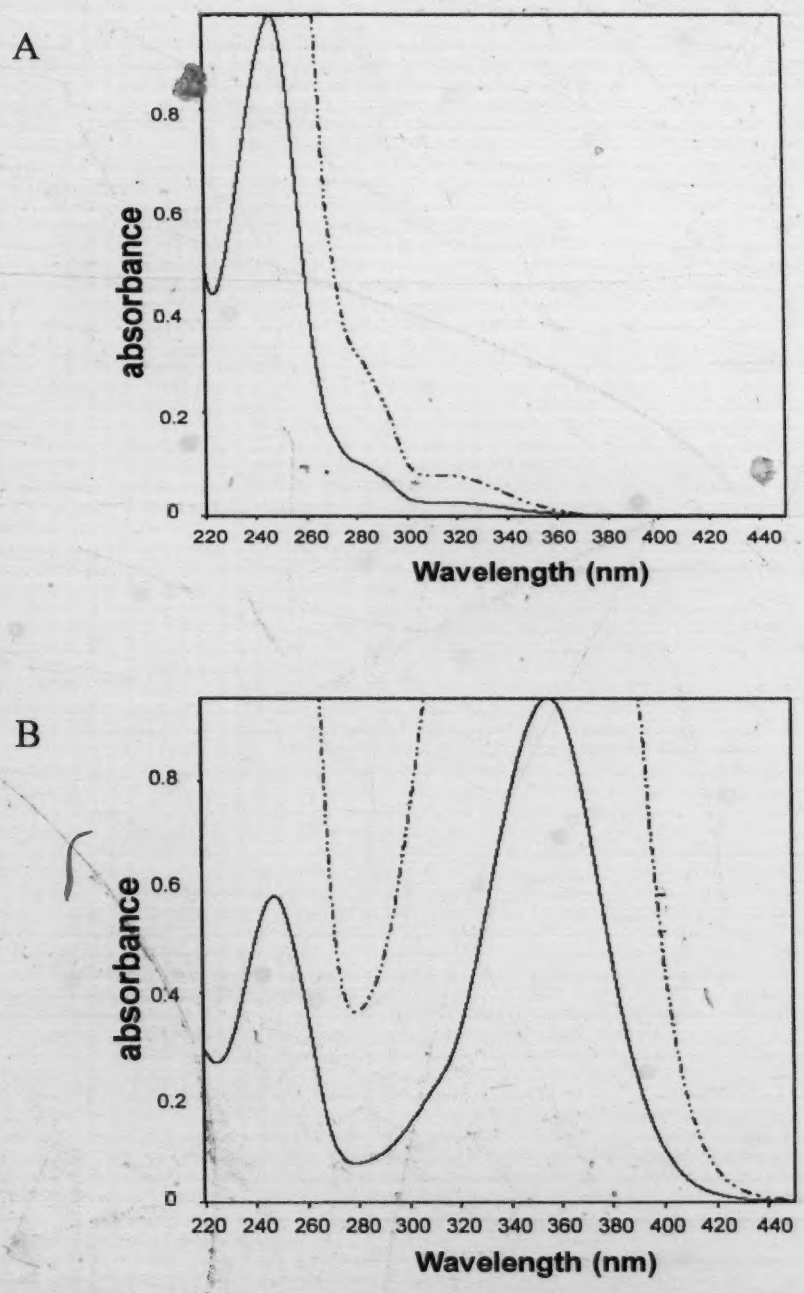

Figure 5.2 The UV absorption profiles for photoinitiators. **A**: benzoin; **B**: 4-(dimethylamino) benzophenone. The graphy was adapted from website.

5.3.2 Photopatterning Resolution

Photo-polymerization is restricted to UV-exposed regions and monomers from the unexposed regions can be flushed away after the irradiation step, leaving a patterned surface chemistry. The photo-mask can be made by transparency printing for patterning high-resolution features and complicated design, or with a handmade mask for low-resolution features using black cardboard or black tape. Figure 5.3 shows a typical example of simultaneous photopatterning of several monolithic beds in individual microfluidic channels. A polymer monolith bed is indicated in Figure 5.3 by an arrow, showing the opaque and white color in the dry state. The length and position of the monolithic bed can be defined by the mask design.

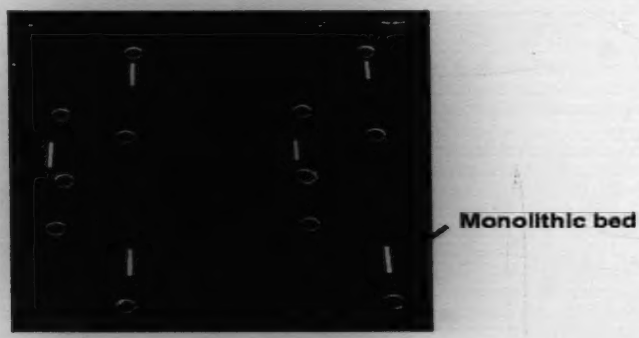

Figure 5.3 Digital photo of polymer monoliths photopatterned within microfluidic devices.

Good control over photopatterning is an important factor in obtaining a sharp edge for monoliths in microchannels. The resolution of a photopatterned polymer in a channel is determined by two factors: (1) photolithographic resolution and (2) diffusion of free radicals from the exposed region to the unexposed region [27]. The resolution limit b_{min} is given as:

$$2\, b_{min} = 3\, [\lambda(s+z/2)]^{1/2} \qquad (5.1)$$

λ is the wavelength, s is the distance between the mask and polymer surface, and z is the polymer thickness. In this experiment, the wavelength is 312 nm. s is 0.6 mm, because the mask is in contact with the 0.6-mm thick glass wafer. z is the depth of the channel and is typically 20-40 μm. Based on this equation, the theoretical resolution limit is 20 μm. In practice, we observed the offset of the bed edge from the mask is about 100 μm, which indicates that transport of free radicals by diffusion or convection is the limiting factor in edge definition. The UV transilluminator can lead to a heating effect, causing convective flow and the possibility of heat induced polymerization in the unexposed regions. A cooling fan was used to reduce the heat produced from the transilluminator and help maintain a constant temperature, in an effort to minimize heat-induced polymerization.

Figure 5.4A shows the top view of the edge of a polymer in a channel. The left, dark region is the monolith, and the right, clear region is microchannel without monolith. The sharp interface and the uniform structural distribution indicate good control over photopatterning, which is compared to results from the literature [27] shown in Figure 5.4 B. The reproducibility of photopatterning control was also investigated in this chapter. Photopolymerization was repeated several times in different batches of glass chips. Typical results are shown in Figure 5.5 for the top-view of the bed edges formed in different batches, showing the reproducibility of photopatterning.

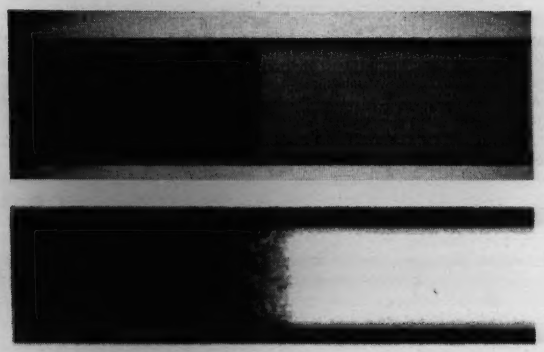

Figure 5.4 The top-view of the edge of polymer monolith cast in microchannel. The left dark part is monolith and right clear part is microchannel without monolith. **A**: the result from experiment. HEMA 16 wt%, EDMA 24 wt%, 1-octanol 60 wt%, Benzoin0.004 wt%, 312nm UV for 9 min. **B**: A result from literature [27]. 30%1,3-butanediol diacrylate, 0.5% AMPS, 0.3% trimethoxysilylpropyl acrylate, 6.92% lauryl acrylate, 62.28% butyl acrylate, and 0.5 wt % of the initiator AIBN.

Figure 5.5 The top-view of the edges of polymer monoliths cast in microchannels for different bathes. The bottom dark part is monolith and top clear part is glass microchannel without monolith. The polymerization conditions are the same as indicated in Figure 5.4 A.

5.3.3 Solvent Selection

The selection of the porogenic solvent is an important, but complex tool, which may be used for control of porous properties without changing the chemical composition of the final polymer. The final pore size of the monolith is not completely predictable based on the solvents, and optimization is required. The results for the pore size of monoliths related to different recipes reported in 67 articles are given in the Appendix. The commonly used solvents include cyclohexanol, 1-propanol, methanol, toluene and alcohols with a long carbon chain. We repeated many recipes reported in the literatures. Many of the systems tested did not give well defined edges when photopatterned, as discussed in Section 2.3.2. Additionally, many binary solvent mixtures have been reported to give widely varying pore sizes as a result of very small variations in solvent composition, making them unattractive for the generation of reproducible columns. A number of these solvent choices, especially mixtures containing methanol or hexane, can be identified by close examination of the information in the Appendix. Less volatile solvents also produce widely different flow resistance, an observation which is again detailed in Section 2.3.2. From the various systems tested we selected 1-octanol, because it gives a reasonably low flow resistance with pores on the 1 μm scale, stable monoliths, and good photo-pattern definition.

5.3.4 Pore Structure

Polymer monoliths are characterized by a permanent porous structure formed during their preparation, which persists even in the dry state. The current knowledge of factors that control pore size is mostly empirical. The monomers control the surface chemistry of

the monoliths. Figure 5.6A shows a monolith with hydrophobic surface chemistry, photopolymerized in a microchannel using the monomer BMA. In Figure 5.6B, a hydrophilic monolith is shown that was formed using the monomer HEMA. The same porogenic solvent 1-octanol was added in both recipes, and produced similar clusters of globules with large through-pores. The pore size distribution was significantly different for those two recipes, likely due to the different solubility of monomer and polymer in the solvent. Solubilities are key factors that define the phase separation onset and it results in different pore size distributions. The corresponding pore size distributions for these two recipes are shown in Figure 5.6 C and D. The characteristic pore diameter of the monolith is represented as the highest peak of the pore size distribution profile. As seen from Figure 5.6, the pore diameter of the hydrophobic monolith is 0.84 μm (C) and the pore diameter of the hydrophilic monolith is 1.05 μm (D). The formation of the relative larger pore is due to the poorer solubility of HEMA in the solvent 1-octanol compared to BMA. In addition photoinitiator benzoin could be another factor to affect the final structure by changing the solubility. The finite peak width shown there is a significant pore size distribution, showing the fact there are smaller pores contribute to the surface area of the monolith and larger pores or cavities contribute to the flow-through permeability.

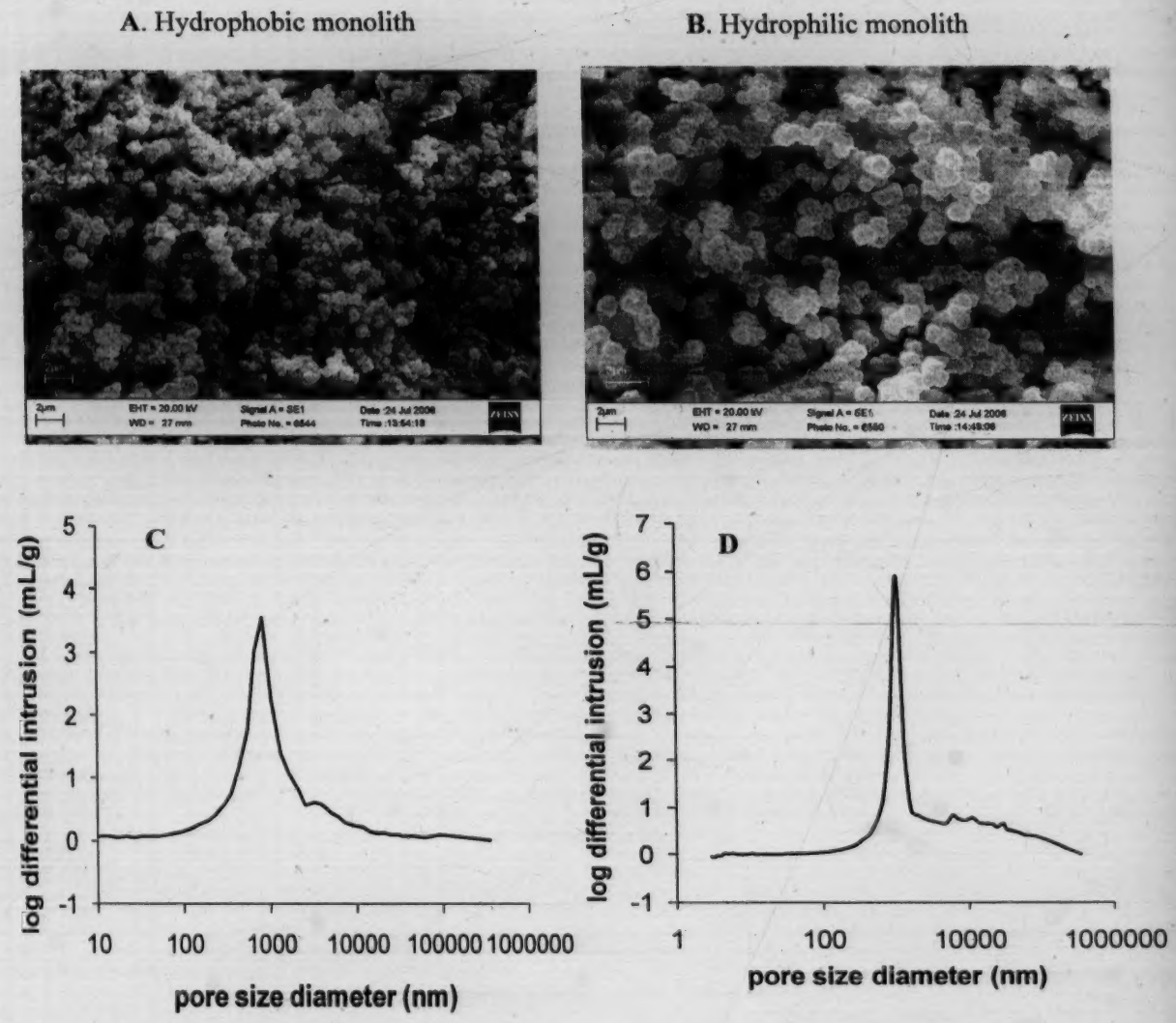

Figure 5.6 The morphology and pore size distributions of monoliths with different surface chemistries. **A and C:** SEM image and pore size distribution of hydrophobic monolith, BMA 16 wt%, EDMA 24 wt%, 1-octanol 60 wt%, Benzoin 0.004 wt%, 312nm UV for 9 min. **B and D**: SEM image and pore size distribution of hydrophilic monolith, HEMA 16 wt%, EDMA 24 wt%, 1-octanol 60 wt%, Benzoin 0.004 wt%, 312 nm UV for 9 min.

5.3.5 Enzymatic Microreactor

HEMA was chosen as the monomer to fabricate the enzymatic microreactor in the microchannel, because HEMA gives a hydrophilic functional group and, therefore, provides a protein friendly environment that reduces non-specific adsorption onto the surface. GMA was chosen as the co-monomer, because GMA contains the epoxy group, which can covalently bond with amine groups of the enzyme.

The morphology and porous properties obtained for the microreactor are shown in Figure 5.7. As seen from the SEM image in Figure 5.7A, the clusters of microglobules were regular distributed, with flow-through pores. The characteristic pore diameter of the bulk material was 0.83 μm and the porosity was 78% as shown in Figure 5.7B. Around 40% of the pores were in a range below the characteristic pore diameter, which contributes to the surface area and enhances the capacity.

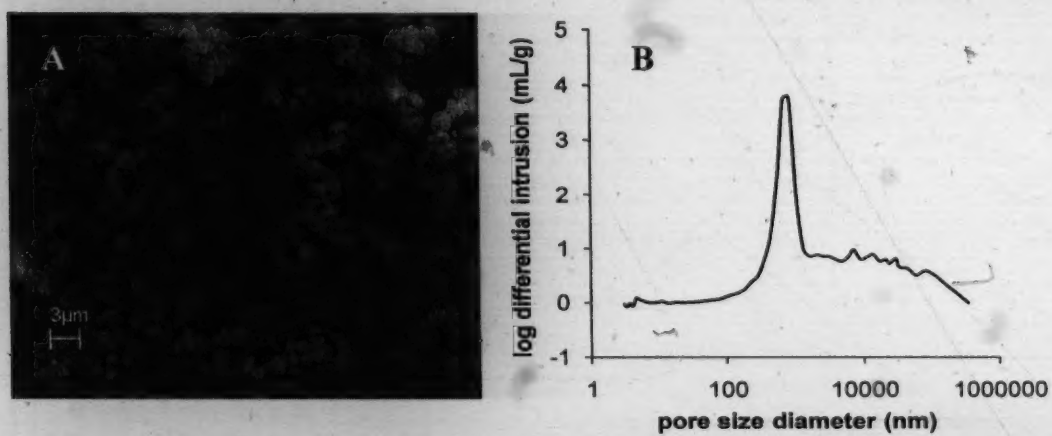

Figure 5.7 A: The morphology of the microreactor shown by SEM image; **B**: The pore size distribution of the microreactor measured by mercury intrusion porosimetry. The porosity is 78%. The recipe for the polymerization was list in Table 5.1.

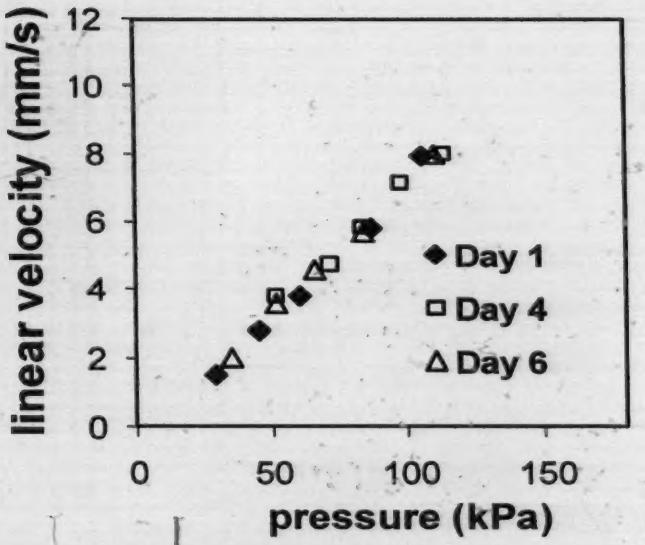

Figure 5.8 The stability of the flow resistance for microreactor measured over one week. The recipe was shown in Table 5.1.

The stability of the flow-through characteristic is essential for the function of trypsin beds. The flow resistance of the monolithic bed was measured as described in Chapter 2. The linear relationship between the pressure and the flow rate shown in Figure 5.8 indicates that the monolithic bed persists in a stable porous structure. The back pressure for the monolithic bed remained very low. The repeatable flow resistance measured within one week indicates good stability and reproducibility of this monolithic bed obtained from the recipe list in Table 5.1. The RSD of the reproducibility of the flow resistance was 2%.

Immobilization of enzyme onto a solid support allows for repetitive use and also facilitates product isolation, once digestion has been carried out. Immobilization of trypsin also avoids auto-digestion of the trypsin itself, and reduces interference [23]. Cytochrome C solution was flowed through the trypsin bed with a residence time of 180 s. The digested peptide mass spectrum is shown in Figure 5.9 and the mass assignments are

shown in Table 5.2. Nine peaks were assigned to the digested peptides. The sequence coverage was 78% and no auto-digested trypsin fragment peaks were found with amount of 0.05mg/ml Cytochrome C. The rate-determining step for on-bed digestion is the diffusion of large substrate molecules to the active sites. The digested peptide mass spectrum for 60 s residence time is shown in Figure 5.10, and the mass assignments are shown in Table 5.3. The sequence coverage was 45.2% and no auto-digested trypsin fragment peaks were found. The sequence coverage is lower compared with the 180 s residence time. This is because the faster flow rate limited the diffusion time and decreased the possibility of the proteolysis during the diffusion of protein to the enzymatic active sites.

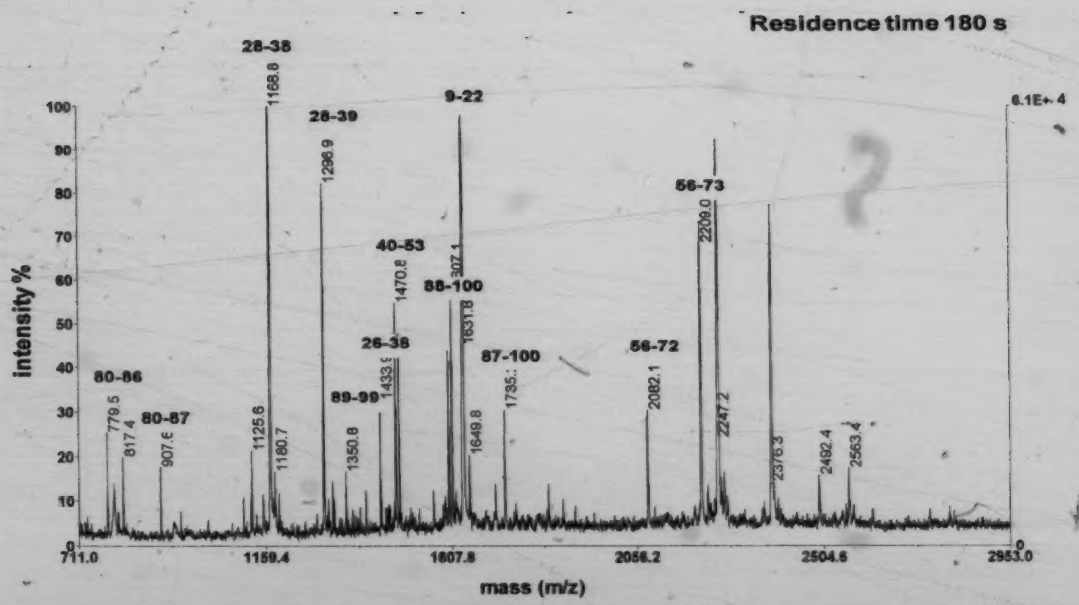

Figure 5.9 The m/z spectra of digested Cytochrome C by using trypsin immobilized monolithic microreactor. The length of the monolithic bed is 7 mm. The residence time is 180 s. The residues position is labeled on the top of the assigned peak. The sequence coverage is calculated as 78%. No auto-digested trypsin fragment peaks were found.

Table 5.2 Experimentally identified peptides from Figure 5.9.

Peptide mass	Theoretical (MH+)	Residues position	Missed cleavages
779.5	779.4484	80-86	0
907.6	907.5433	80-87	1
1168.8	1168.6221	28-38	0
1296.9	1296.7171	28-39	1
1350.8	1350.7263	89-99	1
1433.9	1433.7760	26-38	1
1470.8	1470.6859	40-53	0
1631.8	1633.8189	9-22	1
2209.0	2209.1209	56-73	2

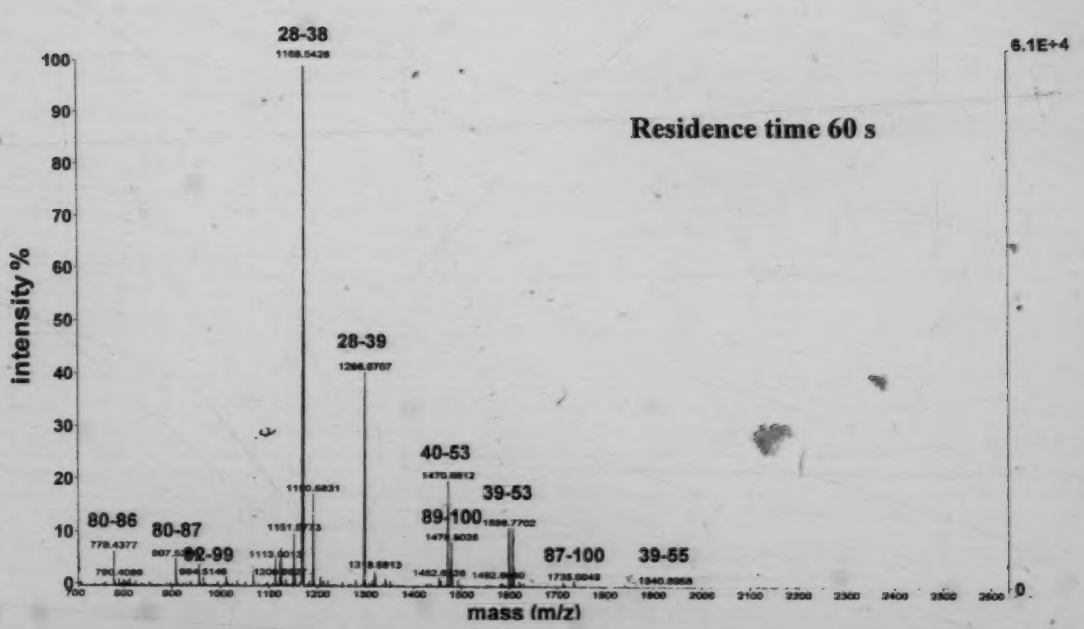

Figure 5.10 The m/z spectra of digested Cytochrome C by using trypsin immobilized monolithic microreactor. The residence time is 60 s. The residues position is labeled on the top of the assigned peak. The sequence coverage is calculated as 45.2%. No auto-digested trypsin fragment peaks were found.

Table 5.3 The Experimentally identified peptides from Figure 5.10.

Peptide mass	Theoretical (MH+)	Residues position	Missed cleavages
779.4	779.4484	80-86	0
907.5	907.5433	80-87	1
964.5	964.5349	92-99	0
1168.5	1168.6221	28-38	0
1296.6	1296.7171	28-39	1
1470.6	1470.6859	40-53	0
1478.8	1478.8213	89-100	2
1598.7	1598.7809	39-53	1
1840.8	1840.9188	39-55	2

5.4 CONCLUSIONS

To conclude, the conditions for polymer monolith microreactor photopatterned within glass microfluidic chips were investigated and optimized, which include the photopatterned resolution, surface chemistry selection, pore structure control and porogenic solvent selection. On-bed protein digestion was successfully performed by this microreaction immobilized with trypsin. The sequence coverage for Cytochrome C digestion is 78% for 180 s residence time. The flow-through property of the microreactor was investigated, and was found to be quite stable and reproducible over one week.

5.5 REFERENCES

1 Auroux, P. A.; Iossifidis, D.; Reyes, D. R.; Manz, A. *Anal. Chem.* **2002**, *74*, 2637-2652.

2 Herr, A. E.; Molho, J. I.; Drouvalakis, K. A.; Mikkelsen, J. C.; Utz, P. J.; Santiago, J.G.; Kenny, T. W. *Anal. Chem.* **2003**, *75*, 1180-1187.

3 Liu, J.; Lin, S.; Qi, D.; Deng, C.; Yang, P.; Zhang, X. *J. Chromatogr. A.* **2007**, *1176*, 169-177.

4 Tan, A.; Benetton, S.; Henion, D. J. *Anal. Chem.* **2003**, *75*, 5504-5511.

5 Lazar, M. L.; Li, L.; Yang, Y.; Karger, B. L. *Electrohphoresis* **2003**, *24*, 3655-3662.

6 Broyles, B. S.; Jacobson, S. C.; Ramsey, J. M. *Anal. Chem.* **2002**, *74*, A-G.

7 Srbek, J.; Eickhoff, J.; Effelsberg, U.; Kraiczek, K.; Goor, T. V. D.; Coufal, P. *J. Sep. Sci.* **2007**, *30*, 2046-2052.

8 DeVoe, D. L.; Lee, C. S. *Electrophoresis* **2006**, *27*, 3559-3568.

9 Cooper, J. W.; Wang, Y.; Lee, C. S. *Electrophoresis* **2004**, *25*, 3913-3926.

10 Figeys, D. *Proteomics* **2002**, *2*, 373-382.

11 Gac, A. L.; Carlier, J.; Camart, J. C.; Olivé, C. C.; Rolando, C. *J. Chromatogr. B* **2004**, *808*, 3-14.

12 Eeltink, S.; Geiser, L.; Svec, F.; Fréchet, J. M. J. *J. Sep. Sci.* **2007**, *30*, 2814-2820.

13 Solazzo, C.; Fitzhugh, W. W.; Rolando, C.; Tokarski C. *Anal. Chem.* **2008**, *80*, 4590–4597.

14 Choi, H.; Ghosh, D.; Nesvizhskii, A. I. *J. Proteome Res.* **2008**, *7*, 286–292.

15 Martens, L.; Hermjakob, H.; Jones, P.; Adamski, M.; Taylor, C.; States, D.; Gevaert, K.; Vandekerckhove, J.; Apweiler, R. *Proteomics* **2005**, *5*, 3537-3545.

16 Křenková, J.; Bilková, Z.; Foret, F. *J. Sep. Sci.* **2005**, *28*, 1675-1684.

17 Luo, Q.; Page, J. S.; Tang K.; Smith, D. R. *Anal. Chem.* **2007**, *79*, 540-545.

18 Geiser, L.; Eeltink, S.; Svec, F.; Fréchet, J. M. J. *J. Chromatogr. A* **2008**, *1188*, 88-96.

19 Křenková, J.; Foret, F. *Electrohphoresis* **2004**, *25*, 3550-3563.

20 Liu, Y.; Svec, F.; Fréchet, J. M. J. *Anal. Chem.* **1997**, *69*, 61-65.

21 Taylor, J.; Wang, C.; Harrison, D. J. *Proc. μTAS2002*, Netherlands, **2002**, 344-346.

22 Peterson, D. S.; Rohr, T.; Svec, F.; Fréchet, J. M. J. *J. Proteome Res.* **2002**, *1*, 563-568.

23 Peterson, D. S.; Rohr, T.; Svec, F.; Fréchet, J. M. J. *Anal. Chem.* **2003**, *75*, 5328-5335.

24 Logan, T. C.; Clark, D. S. *Anal. Chem.* **2007**, *79*, 6592-6598.

25 Peterson, D. S.; Rohr, T.; Svec, F.; Fréchet, J. M. J. *Anal. Chem.* **2002**, *74*, 4081-4088.

26 Temporini, C.; Calleri, E.; Campèse, D.; Cabrera, K.; Félix, G.; Massolini, G. *J. Sep. Sci.* **2007**, *30*, 3069-3076.

27 Throckmorton, D. J.; Shepodd, T. J.; Singh, A. K. *Anal. Chem.* **2002**, *74*, 784-789.

Chapter 6

Conclusions and Future Work

6.1 SUMMARY OF THE THESIS

Monolithic materials have developed rapidly during the last 15 years and currently hold an impressively strong position in separation science, and in other areas of chemistry. Integration of this polymer material into microfluidic devices has attracted increasing interest recently. However, there is a lack of systematic study on photopolymerization in micro-scale channels, yet the information from such studies is essential for the development and application of monoliths in microfluidics. This doctoral dissertation has concentrated on the fundamental and systematic investigation of photopolymerization conditions under microscale confinement, and the fluidic properties of various polymer monoliths patterned within microfluidic chips, as well as their applications for separation science and proteomics.

First, we systematically examined a wide range of polymerization conditions in order to establish a useful protocol for photo-patterning well-defined monolithic beds with stable fluidic properties. A time of flight, photobleaching method we developed previously allows us to accurately measure the flow rate inside various monolithic columns, in contrast to the mercury intrusion porosimetry which is restricted to measurement of the dry state of a bulk-scale prepared monolith. The polymerization conditions, including porogenic solvent, monomer composition, and photo-exposure time,

have been optimized to obtain good fluidic stability and reproducibility for photopatterned monolithic beds, which are critical for their applications in multiplexed microfluidic systems, such as parallel functional arrays.

During these studies, we found that the physical confinement of microchannels induces significant spatial variation of monolithic structures, which leads to a new strategy to manipulate the morphology of polymer monoliths within micrometer-scale confinement. The extent of deformation from the bulk porous structure under confinement strongly depends on the ratio of the characteristic length of the confined space to the monolith pore size. Bulk-like porosity was observed when the ratio of critical confinement dimension to pore size is larger than 10, while significant deformation was observed for a ratio smaller than 5. At the extreme limit of deformation a smooth polymer layer is formed on the surface of the capillary or microchannel. The films created by extreme deformation provide a rapid and effective strategy for robust wall coating, which can be further modified by photografting to create various surface chemistries onto the coating. To our knowledge, this was the first report to manipulate the structure of polymer monoliths for localizable surface modification.

Using this new coating strategy, we have realized several types of coating films within microchannels with tunable thicknesses ranging from ~100 nm to ~700 nm. HEMA-based neutral and hydrophilic coatings have been demonstrated for reducing non-specific adsorption during protein separation. We also demonstrated photografting the monolithic coating with positively charged META for EOF control, and with zwitterionic SBMA for open channel CEC separation of proteins. The results established that this thick film coating can be readily prepared with less time and less complication based on

the confinement effect compared to other methods. The film produced can be generated with many different surface functionalities and did achieve improved separation resolving power. This method provides a novel surface modification strategy for applications such as surface chemistry control, surface biocompatibility, capillary electrophoresis and open tubular chromatography.

6.2 FUTURE WORK

In this section, we will briefly discuss the future perspectives of this work.

In Chapter 2, a protocol was established to prepare well-defined monolithic beds with stable fluidic properties, which enables photopatterning of multiple beds with a satisfied uniformity and reproducibility within one wafer. This work focused on the investigation of HEMA-based hydrophilic polymer bed, since this type of monolithic material is quite suitable to immobilize trypsin molecules for the on-bed enzymatic digestion. For greater generality, it is necessary to look at other polymeric monoliths, such as the BMA-based hydrophobic polymer bed, which is suitable for protein preconcentration. In Chapter 5, we demonstrated photopatterning of optimized monolithic trypsin beds for protein digestion. Obviously, this approach to photopatterning arrays of beds with different functionalities in a single multiplexed microfluidic platform should be further tested in a truly integrated microsystem for high-throughput and automated proteomic applications [1, 2].

In Chapter 3 and 4, a coating strategy based on the confinement effect was established and evaluated for protein separation. The separation efficiency could be further improved by optimizing the coating procedures in terms of the reaction time,

mixture composition and film thickness. Some initial attempts were undertaken to photograft specific functional groups for EOF control and open-channel CEC separation. Approaches to optimize the functional group density and composition should be undertaken to further improve the established procedures, as well as the durability and performance of the coatings.

This coating performance has been evaluated for the chip format. However, it is much easier to conduct studies in fused-silica capillaries, for instance in a 10 or 20- μm i.d. capillary with a UV transparent outside coating. This methodology will attract more interest from industries, because it can provide fused-silica capillaries with widely functionalized and well characterized inner surface coatings for specific applications. Additionally, the confinement effect on the monolithic morphology observed in Chapter 3 should allow simple and spatially selective fabrication of both open tubular coatings and porous monolithic structures within a microfluidic device, by deliberately varying the device dimensions at desired locations.

To summarize, this thesis represents an initial effort to fundamentally and systematically investigate the photopolymerized monoliths integrated in microfluidic devices. The kinetics and mechanism of free radical polymerization in confined space still remain limited. Currently, a significant expansion has been witnessed in the micro-scale chips integrated with polymer monoliths for proteomics [3-5]. The rapidly increasing diversity of functional monomers will make it possible to find more applications in the fields of lab-on-chip and nanotechnology [6, 7].

6.3 REFERENCES

1 Tan, A.; Benetton, S.; Henion, J. D. *Anal. Chem.* **2003**, *75*, 5504-5511.

2 Gac, S. L.; Carlier, J.; Camart, J. C.; Olivé, C. C.; Rolando, C. *J. Chromatogr. B* **2004**, *808*, 3-14.

3 Buchmeiser, M. R. *Polymer* **2007**, *48*, 2187-2198.

4 Levkin, P. A., Eeltink, S.; Stratton, T. R.; Brennen, R.; Robotti, K.; Yin, H.; Killeen, K.; Svec, F.; Fréchet, J. M. J. *J. Chromatogr. A* **2008**, *1200*, 55-61.

5 Peterson, D. S.; Rohr, T.; Svec, F.; Fréchet, J. M. J. *J. Proteome. Res.* **2002**, *1*, 563-568.

6 Tripp, J. A.; Stein, J. A.; Svec, F.; Fréchet, J. M. J. *Org. Lett.* **2000**, *2*, 195-198.

7 Nordborg, A.; Svec, F.; Fréchet, J. M. J.; Irgum, K. *J. Sep. Sci.* **2005**, *28*, 2401-2406.

Appendix

Summary of Pore Size of Monoliths Corresponding to Different Recipes Reported in Literatures

1. Polymerization with the same recipe reported from different literature

Solvents: Methanol + Hexane

NO	Journal	monomer	solvent	Reaction conditions	Pore size (μm)
1	Anal. Chem.,**1998**, 70, 4879-4884	10%EDMA 15%BMA	52.5%Methanol 22.5%Hexane	24 h@70°C.	19.5
2	Anal. Chem., **2003**, 75, 5504-5511	10% EDMA 15% BMA	52.5% methanol 22.5% hexane	UV for 20min	10
3	Electrophoresis, **2001**, 22 , 3959–3967	16%EDMA 24% HEMA	30%Methanol 30%Hexane	UV for 60 min	10.7
4	J. Polym. Sci., Part A: Polym. Chem., **2002**, 40, 755-769	16% EDMA 24% HEMA	30% methanol 30% hexane	UV for 16h	7.9

Solvents: Toluene + Dodecanol

NO	Journal	monomer	solvent	Reaction conditions	Pore size (μm)
1	Chem. Mater., **1997**, 9, 1898-1902	20% styrene 20% DVB	15% tolune 45% 1-dodecanol	20 h@60°C.	20
2	Chem. Mater., **1996**, 8, 744-750	20% styrene 20% DVB	15% toluene 45% 1-dodecanol	12 h@60°C.	1.75

Solvents: Decanol

NO	Journal	monomer	solvent	Reaction conditions	Pore size (μm)
1	J. Chromatogr. A, **2004**, 1051, 53–60	16% EDMA 24% BMA	60% 1-Decanol	UV for 10 min	2.24
2	Macromolecules, **2003**, 36, 1677-1684	16% EDMA 24% BMA	60% 1-Decanol	UV for 10min	2
3	Rapid Commun. Mass Spectrom. **2004**, 18, 1504–1512	16%EDMA 24%BMA	60% 1-Decanol	UV for 5 min	2.13
4	Anal. Chem., **2003**, 75, 5328-5335	20%EDMA 12%HEMA 8%VAL	60 %1-decanol	UV for 10min	1.02
5	J. Proteome Res., **2002**, 1, 563- 568	20% EDMA, 8% 1-vinyl-4,4-dimethylazalactone, 12% HEMA	60% 1-decanol	UV for 6 min	1.02

Solvents: Decanol + Cyclohexanol

NO	Journal	monomer	solvent	Reaction conditions	Pore size (μm)
1	J. Sep. Sci., **2004**,27,779 –788	24%BMA 16%EDMA	50%1- decanol 10%1-cyclohexanol	UV for10 min	1.64
2	Anal. Chem., **2004**, 76, 3887-3892	24 wt % BMA, 16 wt % EDMA	50 % 1-decanol 10 % cyclohexanol,	UV for 10min	1.6

2. Recipes listed in order by pore size

NO	Journal	monomer	solvent	Reaction conditions	Pore size (µm)
1	Anal. Chem., **2001**, 73, 5088-5096	10%EDMA 12%HEMA 3%META	52%Methanol 22%Hexane	UV for 3 h	13.2
2	J. Polym. Sci., Part A: Polym. Chem., **2002**, 40, 755-769	24% BMA 16% EDMA	60% methanol	UV for 16h	9.07
3	Chem. Mater., **1998**, 10, 4072-4078	80% divinylbenzene 20% ethylstyrene	2% toluene 58% decanol	24 h@70°C.	7.59
4	J. Polym. Sci., Part A: Polym. Chem., **2002**, 40, 755-769	24% GMA 16% EDMA	48%methanol 20%ethyl acetate	UV for 16h	7.5
5	J. Chromatogr. A, **1999**, 855, 273–290	2:1 Styrene: DVB	n-propanol	24 h@70°C.	7
6	Chem. Mater., **1998**, 10, 4072-4078	80% divinylbenzene 20% ethylstyrene	52% dodecanol 8% toluene	24 h@70°C.	6.19
7	J. Polym. Sci., Part A: Polym. Chem., **2002**, 40, 755-769	24% GMA 16% EDMA	30% methanol 30% hexane	UV for 16h	5.2
8	J. Chromatogr. A, **1999**, 855, 273–290	2:1 Styrene: DVB	ethanol	24 h@70°C.	5
9	Anal. Chem., **2005**, 77, 417-423	40:60, EDMA/BMA with 1.5% AMPS	55% propanol 35% butanediol, 10% water.	24 h@60 °C	5
10	J. Polym. Sci., Part A: Polym. Chem., **2002**, 40, 755-769	24% GMA 16% EDMA	30% methanol 30% ethanol	UV for 16h	4.7
11	Anal. Chem., **2002**, 74, 2336-2344	20% styrene 20% DVB	40% 1-propanol 20% formamide	24 h@60°C.	4
12	J. Polym. Sci., Part A: Polym. Chem., **2002**, 40, 755-769	24% BMA 16% EDMA 1% AMPS	30% methanol 30% ethanol	UV for 16h	4.0
13	J. Sep. Sci., **2005**, 28, 2401-2406,	26%BMA 13%EDMA	30%1-propanol 30% 1,4-butanediol	24 h@70°C	3.8
14	Chem. Mater., **1997**, 9, 463-471	TRIM/GMA70/30	isooctane/toluene70/30	UV for 60min	3.6
15	Anal. Chem., **2005**, 77, 407-416	19% EDMA 22% BMA 1.8% AMPS	35% 1-propanol, 23% 1,4-butanediol, water	20 h@60 °C	3.4
16	J. Polym. Sci., Part A: Polym. Chem., **2002**, 40, 755-769	24% BMA 16% EDMA 1% META	36%1-propanol 24%1,4 butanediol	UV for 16h	3.1

17	Ind. Eng. Chem. Res., **1999**, 38, 34-48	20 wt % ethylene dimethacrylate, 20% vinylazlactone + acrylamide,	60% tetradecanol	24 h@60°C.	2.92
18	Electrophoresis, **2000**, 21, 120-127	16% EDM 24% BMA 0.36g AMPS	74% 1-propanol 16% 1,1 butanediol	UV for 16h	2.8
19	Chem. Mater, **1996**, 8, 744-750	24% GMA- 16% EDMA	15 %1-dodecanol 45%cyclohexanol	12 h@70°C.	2.5
20	J. Polym. Sci., Part A: Polym. Chem., **2002**, 40, 755-769	24% HEMA 16% EDMA	60% 1-octanol	UV for 16h	2.3
21	J. Sep. Sci., **2006**, 29, 25–32	22.4%BuMA 17.6%EDMA	21.6%1-Propanol 38.4%1,4-Butanediol	24 h@70°C	2.05
22	J. Polym. Sci., Part A: Polym. Chem., **2002**, 40, 755-769	24% HEMA 16% EDMA	60% 1-heptanol	UV for 16h	2.0
23	Anal. Chem., **2005**, 77, 7342-7347	23.8% BMA, 15.8% EDMA, 0,4% META	5.5% water, 22.0% 1,4-butanediol, 32.5% 1-propanol	20 h@70°C	2
24	Anal. Chem., **2001**, 73, 4071-4078	20%NBE 20%DMN-H6	50%2-PrOH 10%Toluene	0.5 h@80°C.	2
25	Sens. Actuators, A, **2004**, 99, 66-73	24%Chloromethylstyrene, 16% DVB	42 %1-dodecanol 18% toluene	12 h@70°C.	1.7
26	Anal Chem., **2000**, 72, 4614-4622	8% Chiral selector 16% HEMA 16% EDMA	40%1-decanol 20% cyclohexanol	UV for 16 h	1.7
27	Chem. Mater., **1997**, 9, 1898-1902	24% GMA 16% EDMA	60 % cyclohexane	20 h@60°C.	1.5
28	Chem. Mater., **1995**,7, 707-715	24% GMA- 16% EDMA	12 %1-dodecanol 48%cyclohexanol	12 h@55°C.	1.5
29	J. Polym. Sci., Part A: Polym. Chem., **2002**, 40, 755-769	24% BMA 16% EDMA	30% methanol 30% ethanol	UV for 16h	1.5
30	Anal. Chem., **2000**, 72, 5693-5699	GMA-EDMA	cyclohexanol, dodecanol,	12 h@60°C.	1.5
31	Rapid Commun. Mass Spectrom. **2004**, 18, 1504–1512	16% EDMA 24% Benzyl MA	60%1-Decanol	UV for 5 min	1.2
32	J. Chromatogr. A, **1999**, 852, 297-304	24% GMA- 16% EDMA	6 %1-dodecanol 54%cyclohexanol	12 h@55°C.	1.2
33	Macromolecules, **2000**, 33, 7769-7775	1:1 DVB+ styrene	5% Polystyrene 55% toluene	12 h@60°C.	1.1
34	J. Polym. Sci., Part A: Polym. Chem., **2002**, 40, 755-769	24% HEMA 16% EDMA	60% 1-hexanol	UV for 16h	1.1

35	Electrophoresis **2003**, 24,3172–3180	5.2% Styrene 12.5%DVB 5.2%MAA	37.5% toluene 37.5% isooctane	24 h@70°C	1.095
36	Chem. Mater., **1998**, 10, 4072-4078	80% divinylbenzene 20% ethylstyrene	7% toluene 53% decanol	24 h@70°C.	1.06
37	Anal. Chem.,**1997**, 69, 3646-3649	40 wt % EDMA 60 wt %BMA AMPS in various ratios	10 wt % water 90 wt % of 1-propanol and 1,4-butanediol	20 h@60°C.	1-4
38	Fresenius. J. Anal. Chem., **2001**, 371, 174–181	30% 1,3-butanediol diacrylate 0.3% z-6030, 0.5% AMPS 69.2% butyl acrylate.	monomer to solvent33:67 20% ethanol 60% MeCN	UV for 20 min	1
39	Anal. Chem., **2002**, 74, 784-789	30%1,3-butanediol diacrylate, 0.5% AMPS, 0.3% trimethoxysilylpropyl acrylate, 6.92% lauryl acrylate	62.28% butyl acrylate,	UV for 10 min	1
40	Macromolecules, **2003**, 36, 1677-1684	24% BMA 16% EDMA	20% decanol 40% butanediol	UV for 10min	1
41	Macromolecules, **2003**, 36, 1677-1684	24% BMA 16% EDMA	50%1-decanol 10% cyclohexanol	UV for 10min	1
42	Electrophoresis, **2001**, 22 , 3959–3967	16% EDMA 24% HEMA	42%1-Dodecanol 18% Cylohexanol	UV for 60 min	1
43	Macromolecules, **2000**, 33, 7769-7775	1:1 DVB+ STYRENE	60% octadecanol	12 h@60°C.	1.0
44	Anal. Chem., **2003**, 75, 5328-5335	16%EDMA 24%BMA	43.3 % 1-decanol, 16.7% cyclohexanol,	UV for 10min	0.96
45	Rapid Commun. Mass Spectrom. **2004**, 18, 1504–1512	16%EDMA 24%BMA	43.3%1-Decanol 16.7% Cyclohexanol	UV for 5 min	0.96
46	Anal. Chem., **2002**, 74, 4081-4088	20%EDMA+12%acrylamide+8% 2-vinyl-4,4-dimethylazlactone,	60%1-decanol	UV for 6 min	0.95
47	J. Sep. Sci., **2003**,26,322-330	40% GMA 60% EDMA	60% Cyclohexanol+ dodecanol	24 h@60°C.	0.9
48	Ind. Eng. Chem. Res., **2004**, 43, 6507-6513	50% EDMA 25% GMA	25%Toluene	4 h@60°C 2 h@40°C	0.8
49	Electrophoresis **2003**, 24, 3663–3673	20% EGMA 10% MMA 10% GMA	10% v/v n-propanol, 50% v/v formamide	3 h@65°C 16 h@78°C	0.8
50	React. Funct. Polym., **2005**, 64, 93–102	HEMA(2ml)-MAH(500mg) EGDMA(1ml)	Toluene (1ml)	4 h@55°C, 2 h@75°C	0.75
51	Anal. Chem., **2002**, 74, 4081-4088	20%EDMA+12%acrylamide+8%2-vinyl-4,4-dimethylazlactone,	60%1-dodecanol	UV for 6 min	0.74

52	Anal. Chem.,**1998**, 70, 4879-4884	15% styrene 25% divinylbenzene	45% 1-dodecanol 15% toluene	24 h@70°C.	0.7
53	J. Chromatogr. A, **2004**, 808, 3–14	40% LMA and EGDMA	48% cyclohexanol 12% ethylene glycol	UV for 2 h	0.7
54	J. Chromatogr. A, **2004**, 1051, 53–60	16% EDMA 24% BuMA	40% 1-Decanol 20% Cyclohexanol	UV for 10 min	0.66
55	Chem. Mater., **1998**, 10, 4072-4078	4.85% HEMA 35.2% DVB	57.5% tetradecanol 2.5% toluene	24 h@70°C.	0.6
56	Anal. Chem., **2001**, 73, 5126-5132	30% GMA 10% EDMA	8% cyclohexanol 52% dodecanol	20 h@57°C.	0.6
57	J. Polym. Sci., Part A: Polym. Chem., **2002**, 40, 755-769	24% HEMA 16% EDMA	60% 1-pentanol	UV for 16h	0.4
58	J. Chromatogr. A, **2005**, 1079 382–391	16% PEGMEA 24% EDMA	19% Cyclohexanol + 29% dodecanol + 12% hexanes	UV for 10 min	0.4
59	J. Polym. Sci., Part A: Polym. Chem., **2002**, 40, 755-769	24% HEMA 16% EDMA	60% 1-butanol	UV for 16h	0.3
60	Talanta, **2005**, 66 472–478	60% GMA 40% EDMA	90% cyclohexanol 10% 1-dodecanol	24 h@55°C	0.25
61	Chem. Mater., **1997**, 9, 463-471	TRIM/GMA70/30	isooctane/toluene 30/70	UV for 60min	0.2
62	Rapid Commun. Mass Spectrom. **2004**, 18, 1504–1512	16%EDMA 24%BMA	35% 1-Decanol 25% Cyclohexanol	UV for 5 min	0.2
63	J. Polym. Sci., Part A: Polym. Chem., **2002**, 40, 755-769	24% BMA 16% EDMA 1% AMPS	30% methanol 30% 1-propanol/ 1-butanol/ 1-pentanol/ 1-hexanol/ 1-heptanol	UV for 16h	< 0.2
64	Macromolecules, **2000**, 33, 7769-7775	1:1 DVB+ styrene	60% octanol	12 h@60°C.	0.13
65	Rapid Commun. Mass Spectrom. **2004**, 18, 1504–1512	20% Styrene 20% Divinyl benzene	43% 1-Decanol 17% Toluene	UV for 5 min	0.1
66	Macromolecules, **2000**, 33, 7769-7775	1:1 DVB+ styrene	60% hexadecanol	12 h@60°C.	0.1
67	J. Polym. Sci., Part A: Polym. Chem., **2002**, 40, 755-769	24% HEMA 16% EDMA	60% 1-propanol	UV for 16h	0.1
68	Rapid Commun. Mass Spectrom. **2004**, 18, 1504–1512	16% EDMA 24% BMA	20% 1-Decanol 40% Cyclohexanol	UV for 5 min	0.07

69	J. Polym. Sci., Part A: Polym. Chem., **2002**, 40, 755-769	24% HEMA 16% EDMA	Methanol/ethanol/H2O/MeCN	UV for 16h	< 0.06
70	Macromolecules, **2000**, 33, 7769-7775	1:1 DVB+ styrene	60% decanol	12 h@60°C.	0.05
71	Macromolecules, **2000**, 33, 7769-7775	1:1 DVB+ styrene	60% dodecanol	12 h@60°C.	0.05
72	Macromolecules, **2000**, 33, 7769-7775	1:1 DVB+ styrene	60% tetradecanol	12 h@60°C.	0.05
73	Macromolecules, **2000**, 33, 7769-7775	1:1 DVB+ styrene	60% butanol	12 h@60°C.	0.05
74	Electrophoresis, **2006**, 27,2518–2525	18% GMA 6% EDMA	68% cyclohexanol 6% dodecanol	12 h@60°C	N/A
75	J. Chromatogr. A, **2006**, 1120, 69–74	MMA 8.9%, GMA:EGDMA(2:1)	formamide:1-propanol (7.08:1)	48 h@58°C	N/A
76	Anal. Chem., **2006**, 78, 1673-1681	Sol-gel MPTMS	90% toluene	UV for 5 min	N/A
77	J. Liq. Chromatogr. Related Technol., **2006**, 29, 829–840,	20% GMA 15.5% EGDMA 3.5% BMA	40% cyclohexanol	24 h@57°C.	N/A
78	Anal. Chem., **2006**, 78, 788-792	24% BuMA 16% EDMA	42%1-dodecanol 18%cyclohexanol	UV for 2min	N/A
79	J. Chromatogr. A, **2006**, 1102, 294–301	3% MAA 30% EGDMA	7% toluene 60% dodecanol	16 h@60°C	N/A
80	Radiat. Phys. Chem., **2006**, 75, 26–33	HEMA–EDMA 40:60 wt/wt	methanol n-hexane (63:37wt/wt)	UV for 1 h	N/A
81	Anal. Chem., **2005**, 77 (9), 2997-3000	36%stearylacrylate 36% 1,6-hexanediol diacrylate 14%etrahydrofurfural acrylate	14% 10 mM acetate (pH 5.0), 0.1% methoxyethanol,	UV for 15 min	N/A
82	J.Sep.Sci.,**2005**, 28,1675-1684	24% GMA 16% EDMA	6 % n-octanol 54% cyclohexanol	12 h@60°C.	N/A
83	Anal. Chem., **2005**, 77, 2362-2372	24% GMA 16% EDMA	48 % CyOH 12 % DoOH	24 h@60°C	N/A
84	J. Chromatogr. A, **2005**, 1071, 213–222	65% (EDMA+BMA)	butanediol-propanol (80:20, v/v)	UV for 2 h	N/A
85	J. Chromatogr. A, **2005**, 1065, 51-58	40% (GMA+EDMA)	60%(Cyclohexanol+ 1-dodecanol)	24 h@55°C	N/A
86	Lab Chip, **2005**, 5, 869–876	25% BMA and EDMA with a ratio of 6 to 4	75% methanol and ethanol with a ratio of 2 to 1.	UV for 10min	N/A

87	Electrophoresis, **2005**, 26, 3622 – 3630	10% EDMA 15% BMA	methanol and ethanol 50% /25%	UV for 20min	N/A
88	Electrophoresis **2005**, 26,1988 – 1995	30% PEDAS	66% cyclohexanol/1,4-butanediol 3.6%water.	18 h@60°C	N/A
89	Anal. Chem., **2004**, 76, 6941-6947	24% GMA 15% EDMA	54% cylcohexanol 6% decyl alcohol	UV for 6 min	N/A
90	J. Chromatogr. A, **2004**, 1044, 187–199	24% (w/w)GMA 16% (w/w) EDMA	30% cyclohexanol 30% 1-dodecanol	20 h@60°C	N/A
91	Electrophoresis **2003**, 24, 3689 – 3693	24% HEMA 16% EDMA	29% 1-dodecanol 31% cyclohexanol	UV for 20 min	N/A
92	J. Chromatogr. A, **2002**, 946, 99–106	60% BMA 40% EDMA	36%propan-1-ol,18% butane-1,4-diol, 6% deionized water	20 h@60°C.	N/A
93	Ind. Eng. Chem. Res., **2001**, 40, 3495-3501	24% GMA 16% EDMA	12% dodecanol 48% cyclohexanol	24 h@60°C.	N/A
94	Electrophoresis, **2001**, 22, 544-551	1:1 BMA+EDMA	1:1 1-propanol+1,1 butanediol	12 h@60°C.	N/A